ISBN 978-82-326-0402-9 (printed version)
ISBN 978-82-326-0403-6 (electronic version)
ISSN 1503-8181

Doctoral Thesis
Christopher Nilsen

Doctoral theses at NTNU, 2014:243

Christopher Nilsen

On the motion of inertial particles in unsteady flows

NTNU
Norwegian University of
Science and Technology
Faculty of Engineering
Science and Technology
Department of Energy and
Process Engineering

NTNU – Trondheim
Norwegian University of
Science and Technology

Doctoral theses at NTNU, 2014:243

NTNU

NTNU – Trondheim
Norwegian University of
Science and Technology

Christopher Nilsen

On the motion of inertial particles in unsteady flows

Thesis for the degree of Philosophiae Doctor

Trondheim, August 2014

Norwegian University of Science and Technology
Faculty of Engineering Science and Technology
Department of Energy and Process Engineering

NTNU – Trondheim
Norwegian University of
Science and Technology

NTNU
Norwegian University of Science and Technology

Thesis for the degree of Philosophiae Doctor

Faculty of Engineering Science and Technology
Department of Energy and Process Engineering

© Christopher Nilsen

ISBN 978-82-326-0402-9 (printed version)
ISBN 978-82-326-0403-6 (electronic version)
ISSN 1503-8181

Doctoral theses at NTNU, 2014:243

Printed by Skipnes Kommunikasjon as

Abstract

Inertial particles transported in unsteady flows will not be able to follow the fluid motion perfectly. We explore some of the effects caused by particle inertia. The dissertation contains three parts. In the first part, we show that ellipsoidal particles rotating in oscillating shear flows can exhibit chaotic rotation, and we investigate how the rotation is affected by particle shape and inertia. The second part outlines a set of numerical simulation tools developed to conduct large scale computational studies of particle motion. This includes both a new direct numerical simulation code and two synthetic turbulence generation tools. In the third part, we use the numerical simulation tools to study particle clustering, the tendency for particles to distribute inhomogeneously in space. We discuss some of the characteristics and mechanisms of clustering in both synthetic homogeneous isotropic turbulence and turbulent channel flows.

Preface

The work presented here was carried out at the Norwegian University of Science and Technology (NTNU) under the supervision of professor Helge I. Andersson, to whom I am grateful for the academic freedom I was granted and the supervision I received, during the three years I worked at the university. I would like to thank Lihao Zhao for his assistance during the initial phase of the project, and for the collaboration that led to one of the articles included in the dissertation. I would also like to thank Finn P. Nilsen for giving helpful advice.

Contents

1 Introduction **1**

I Ellipsoids in shear **5**

2 Ellipsoid in simple shear flow **7**
2.1 Ellipsoid in linear shear flow 7
2.2 Constant shear 8
2.3 Rotation in the flow-gradient plane 10
2.4 Relevance to turbulent flow 10

3 Article 1: Chaotic rotation of inertial spheroids in oscillating shear flow **13**

II Numerical turbulence **27**

4 Spectral element direct numerical simulation **29**
4.1 Time discretisation and splitting 29
4.2 The Poisson and Helmholtz equations 32
4.3 Convection operator, aliasing and spectral vanishing viscosity . . 35
4.4 Solving symmetric positive definite systems 36
4.5 Particle tracking 39
4.6 Simulations of turbulent flow 41
4.7 Implementation 42

5 Synthetic turbulence **43**
5.1 Gaussian synthetic turbulence 43
5.2 Non-Gaussian synthetic turbulence 44

6 Article 2: A new spectral element direct numerical simulation code **47**

III Particle clustering **57**

7 Particle dynamics and examples of clustering **59**

7.1 Particle motion in rigid-body vortex 60
7.2 Clustering in a vortex array 61
7.3 Gravity and Brownian motion 62
7.4 Finite-radius effects 64

8 Identifying and describing particle clustering 65
8.1 Density estimation 65
8.2 Measuring clustering 67
8.3 Cluster identification 68
8.4 Particle statistics in channel flow 69

9 Article 3: A Voronoï analysis of preferential concentration in a vertical channel flow 71

10 Article 4: Mechanisms of particle clustering in synthetic turbulence 85

11 Article 5: On wall-normal particle drift and clustering in a turbulent channel flow 97

Bibliography 113

Chapter 1

Introduction

Particles suspended in a fluid are transported by the flow, but as long as they have finite inertia, they will not be able to follow the flow completely. The characteristics and mechanisms of suspended particle transport with flow, is a topic that has great relevance in many natural and industrial applications, and it has been studied extensively over the last hundred years.

With particle, we mean a body suspended in the flow, whose motion can be described without considering its dimensions. Such particles are often called point-particles and for very small particles, to which we will limit our analysis, this is a suitable approximation. We only consider dilute particle suspensions, which means that the particles do not affect the fluid flow or interact with each other.

Although the particles are assumed to have essentially zero volume, they do have finite mass and therefore finite inertia. The significance of particle inertia is often measured using the non-dimensional Stokes number, which is the ratio of a particle time-scale to a fluid time-scale. For low Stokes numbers, the particles are expected to follow the flow passively like fluid particles, while at very high Stokes numbers the particles remain unaffected by all but the largest fluid scales. In-between these two limits, when the particle and fluid time-scales are comparable, interesting and sometimes surprising effects are found. We will see how the particle Stokes number influences the rotation of an ellipsoidal particle and the distribution of spherical particles.

The main topic of this dissertation is how particle inertia influences the motion of particles in unsteady flows, and we look at several different examples to highlight important aspects. The dissertation contains three parts. Part I is concerned with the rotation of a single ellipsoidal particle in a simple unsteady shear flow. Part II details the numerical methodology of direct numerical simulation and synthetic turbulence used to produce the results in part III. Part III deals with the motion and distribution of many spherical particles in turbulent flows. The primary research results are presented in the articles in chapters 3, 6, 9, 10 and 11, while the other chapters contain discussions of related topics.

In part I we look at how prolate spheroidal particles rotate in oscillating shear flows, at different oscillation frequencies. By considering such a simple

flow, we are able to investigate the effects of Stokes number and particle shape in great detail. Chapter 2 contains an introduction to the subject matter and a brief discussion on the potential implications for particles suspended in turbulent flows. In chapter 3, we show that this non-linear oscillation problem has the potential to create chaos, and we investigate how and when ellipsoidal particles can rotate chaotically.

We find that chaotic rotation is possible, as long as the particle Stokes number is greater than the Stokes number for which the fixed shear particle rotation transitions from slow to fast. Chaos emerges when inertial effects and shape effects are comparable in size. Particles with a 3:1 aspect ratio are the most chaotic.

The computational studies in part III, would not have been possible without simulation tools designed to study turbulent flows. This involves two types of simulation codes, one direct numerical simulation Navier-Stokes solver and one synthetic turbulence generation tool, both of which were developed from scratch and are presented in part II. In chapter 4 the spectral element methodology used in the new direct numerical simulation code is presented in detail, while convergence tests are shown in chapter 6. A desire to study homogeneous isotropic turbulence, and the unavailability of such data, lead to the development of the two different synthetic turbulence algorithms presented in chapter 5, one Gaussian and one non-Gaussian. While we have not seen the non-Gaussian methodology used elsewhere, we cannot be certain of its originality.

The decision to develop a new direct numerical simulation code was motivated by two factors. The first was the inherent limitations of the available code (used in chapter 9), with regards to computational and parallelisation efficiency, numerical accuracy and geometric flexibility. The second, and arguably the most important factor, was the invaluable learning opportunity this development project represented. Much like it is important for an experimentalist to understand the fundamentals of conducting advanced experiments, it is imperative within computational science to fully understand the theoretical aspects of solving the equations numerically. Arguably, the best way to understand the various numerical methods used to find an approximate solution to the Navier-Stokes equations, is to develop a Navier-Stokes solver oneself.

To contrast the study of a complex (non-spherical) particle in a simple flow in part I, we study simple (spherical) particles in complex flows in part III. We investigate in detail how swarms of inertial spherical particles tend to form inhomogeneous spatial distributions. In chapter 7, we give an introduction to particle dynamics and provide some simple examples of particle clustering and the effects of gravity, Brownian motion and finite particle radius. The identification and description of particle clustering is explained in chapter 8, where we introduce some new statistical tools that have not been previously applied to particle clustering.

In chapter 10, we look into some of the mechanisms responsible for the formation of particle clusters in synthetic homogeneous isotropic turbulence. We look at two common clustering mechanisms: the vortex centrifuge effect and “caustics”. The vortex centrifuge effect is responsible for the clustering

observed at low Stokes number, and the particles avoid regions of high vorticity. When the Stokes number is greater than unity, caustics emerge and create strong intermittency in the particle velocity field. Although the clustering is quite similar in the two types of synthetic turbulence, preferential sampling of low vorticity regions is much more prominent in the non-Gaussian turbulence. Synthetic simulations cannot accurately predict how particles preferentially sample certain regions of the flow, without including convection.

We also study local particle clustering in turbulent channel flows, and the large-scale accumulation of particles in the near-wall region, in chapters 9 and 11. In chapter 9, we investigate how particle clustering and the wall-normal particle drift are affected by gravity, in a vertical channel flow with shear Reynolds number 395. We use Voronoï analysis to show that gravity decreases the transport of particles towards the walls in a downward flow, while the opposite is true in an upward flow. Local particle clustering in the centre of the channel, is increased in the downward flow.

In chapter 11, we use the new spectral element direct numerical simulation code to simulate the transport of particles in channel flows, at shear Reynolds numbers 180 and 395. An increase in Reynolds number from 180 to 395 causes a significant increase in the particle wall-normal drift velocity. In both cases the drift is maximised for Stokes numbers, based on the wall time scale, around 20. For medium to high Stokes numbers, when the wall-normal flux is strongest, the mean wall-normal particle velocity is close to proportional to the fluid RMS wall-normal velocity. We also look at local particle clustering in the channel flow, and find significant preferential sampling of low vorticity regions, also in the centre of the channel. At higher Stokes numbers, we also observe indications of caustics formation.

References used in chapters 2, 4, 5, 7 and 8, are listed in the bibliography at the end of the document. The rest of the chapters, containing the articles, are self-contained.

Part I

Ellipsoids in shear

Chapter 2

Ellipsoid in simple shear flow

When studying complex physical problems, it is often useful to isolate a small portion of the problem that will be more amenable to in-depth analysis. Applying this philosophy to particle suspended flows, leads us to a study of the rotation of a single non-spherical particle in a simple shear flow. Because we assume the particles are tiny, the flow around each particle can be approximated, by neglecting the fluid acceleration, with the Stokes equations,

$$0 = -\frac{1}{\rho}\nabla p + \nu\nabla^2 \boldsymbol{u}, \tag{2.1a}$$

$$\nabla \cdot \boldsymbol{u} = 0, \tag{2.1b}$$

for the velocity $\boldsymbol{u}$ and the pressure p. The density ρ and kinematic viscosity ν are constants.

2.1 Ellipsoid in linear shear flow

The rotation of a small ellipsoidal particle moving in a viscous flow, is described by Euler's equations

$$\boldsymbol{I}\dot{\boldsymbol{\omega}} + \boldsymbol{\omega} \times (\boldsymbol{I}\boldsymbol{\omega}) = \boldsymbol{M}, \tag{2.2}$$

where $\boldsymbol{\omega}$ is the angular velocity in a rotating reference frame attached to the particle, $\boldsymbol{I}$ is the moment of inertia matrix and $\boldsymbol{M}$ is the torque exerted by the flow. For an ellipsoid, whose surface is described by

$$\frac{x^2}{a^2} + \frac{y^2}{b^2} + \frac{z^2}{c^2} = 1, \tag{2.3}$$

the moments of inertia are

$$\boldsymbol{I} = \frac{4}{15}\pi\rho_p abc\,\mathrm{diag}(b^2 + c^2, c^2 + a^2, a^2 + b^2), \tag{2.4}$$

where ρ_p is the density of the particle.

The orientation of the ellipsoid relative to an inertial reference frame is defined by the quaternion vector $\boldsymbol{e}$, which satisfies $\boldsymbol{e}^T\boldsymbol{e} = 1$. A vector $\boldsymbol{q}$ in the

rotating reference frame can then be expressed in the inertial frame as $\tilde{\boldsymbol{q}} = \boldsymbol{Q}\boldsymbol{q}$, where the rotation matrix $\boldsymbol{Q} = \boldsymbol{G}\boldsymbol{E}^T$ is constructed from the quaternions using

$$\boldsymbol{G} = \begin{bmatrix} -e_2 & e_1 & e_4 & -e_3 \\ -e_3 & -e_4 & e_1 & e_2 \\ -e_4 & e_3 & -e_2 & e_1 \end{bmatrix}, \; \boldsymbol{E} = \begin{bmatrix} -e_2 & e_1 & -e_4 & e_3 \\ -e_3 & e_4 & e_1 & -e_2 \\ -e_4 & -e_3 & e_2 & e_1 \end{bmatrix}. \tag{2.5}$$

If the fluid velocity in the inertial frame is $\tilde{\boldsymbol{u}} = \boldsymbol{K}\tilde{\boldsymbol{x}}$, then the torques on the particle are (Jeffery, 1922)

$$\begin{aligned} M_1 &= \frac{16\pi\rho\nu}{3(b^2\beta + c^2\gamma)} \left\{(b^2 - c^2)S_{23} + (b^2 + c^2)(\Omega_{32} - \omega_1)\right\} \\ M_2 &= \frac{16\pi\rho\nu}{3(c^2\gamma + a^2\alpha)} \left\{(c^2 - a^2)S_{13} + (c^2 + a^2)(\Omega_{13} - \omega_2)\right\} \\ M_3 &= \frac{16\pi\rho\nu}{3(a^2\alpha + b^2\beta)} \left\{(a^2 - b^2)S_{12} + (a^2 + b^2)(\Omega_{21} - \omega_3)\right\}. \end{aligned} \tag{2.6}$$

$\boldsymbol{S}$ and $\boldsymbol{\Omega}$ are the symmetric and antisymmetric parts of the velocity gradient in the particle frame $\nabla\boldsymbol{u} = \boldsymbol{Q}\boldsymbol{K}\boldsymbol{Q}^T$. The constants α, β and γ are computed with the integrals

$$\alpha = \int_0^\infty \frac{d\lambda}{(a^2 + \lambda)\Delta}, \quad \beta = \int_0^\infty \frac{d\lambda}{(b^2 + \lambda)\Delta}, \quad \gamma = \int_0^\infty \frac{d\lambda}{(c^2 + \lambda)\Delta}, \tag{2.7}$$

$$\Delta = \sqrt{(a^2 + \lambda)(b^2 + \lambda)(c^2 + \lambda)}. \tag{2.8}$$

Euler's equations can be solved together with

$$\dot{\boldsymbol{e}} = \frac{1}{2}\boldsymbol{G}^T\boldsymbol{\omega}, \tag{2.9}$$

and written as a system of first-order differential equations $\dot{\boldsymbol{\chi}} = \boldsymbol{f}(\boldsymbol{\chi})$. Some information can be obtained from the system without actually solving it. Taking the divergence of $\boldsymbol{f}$ we get

$$\nabla \cdot \boldsymbol{f} = -\frac{1}{\tau} = -\frac{20\rho\nu}{\rho_p abc}\left(\frac{1}{b^2\beta_0 + c^2\gamma_0} + \frac{1}{c^2\gamma_0 + a^2\alpha_0} + \frac{1}{a^2\alpha_0 + b^2\beta_0}\right), \tag{2.10}$$

from which we can say that the system is dissipative, and that volumes in phase space contract as $\exp(-t/\tau)$. Thus we can expect the solution to approach an attractor in phase space, and that τ is a relevant time-scale for this process. We will use this to define a modified Stokes number in chapter 3.

We only consider prolate spheroids, where $b = c < a$. This reduces some of the complexity of the ellipsoid problem.

2.2 Constant shear

We consider a shear flow where $\partial\tilde{u}/\partial z = \kappa$ and all the other velocity gradients are equal to zero. This is equivalent to setting

$$K_{ij} = \delta_{i1}\delta_{j3}\kappa. \tag{2.11}$$

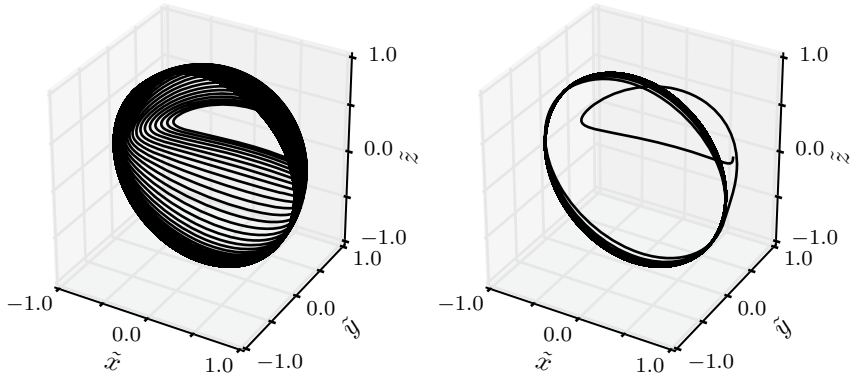

Figure 2.1: Trace of prolate spheroid tip as it drifts towards the flow-gradient plane, for spheroid with $a/b = 5$ and $\mathrm{St} = 100$ (left), and $a/b = 5$ and $\mathrm{St} = 1000$ (right).

The Stokes number, a measure of particle inertia, is the ratio between a particle time scale and a relevant fluid time scale, and we use the definition

$$\mathrm{St} = \frac{\kappa(2a)^2}{\nu}\frac{\rho_p}{\rho}. \tag{2.12}$$

In this flow non-inertial prolate spheroids will move in closed Jeffery orbits (Jeffery, 1922). This motion is reminiscent of the motion of a kayak paddle and therefore often referred to as "kayaking". When there is particle inertia, the spheroids will no longer stay in the closed Jeffery orbits as the particle inertia causes a drift towards the flow-gradient plane (Lundell and Carlsson, 2010). The particle mass is pushed away from the vorticity axis, which is what causes the particles to eventually align in the flow-gradient plane. When there is very little particle inertia (low St), this process is slow and there is only a modest drift from the Jeffery orbit each rotation. For strongly inertial particles (high St), the particle is quickly forced to rotate in the flow-gradient plane. This is illustrated in figure 2.1, where the trace of the spheroid tip is plotted for particles with two different Stokes numbers.

While in the flow-gradient plane, prolate spheroids rotate with a non-constant rate of rotation because the spheroid is not axisymmetric around the rotation axis. A sphere in a similar shear flow will eventually rotate with a constant rate of rotation, as will an oblate spheroid. The rotation around the minor axis in the flow-gradient plane is stable for the prolate spheroid. It is also possible for a prolate spheroid to rotate around its major axis, if it is aligned with the $\tilde{y}$-axis, but this rotation is unstable and a small perturbation will cause the particle to start drifting towards the flow-gradient plane.

2.3 Rotation in the flow-gradient plane

We propose that much can be learned about the dynamics of the rotating spheroid by studying its rotation in the flow-gradient plane. By choosing an initial condition in the flow-gradient plane, Euler's equations simplify to one second order ordinary differential equation for the particle orientation, as shown in chapter 3. This new equation includes the two non-dimensional parameters

$$\varepsilon = \frac{1 - b^2/a^2}{1 + b^2/a^2}, \tag{2.13}$$

which is a shape parameter, and the modified Stokes number

$$\widetilde{\mathrm{St}} = \frac{\mathrm{St}}{80} \frac{1-\varepsilon}{1+\varepsilon} \left(a^3 \alpha + \frac{1-\varepsilon}{1+\varepsilon} a^3 \gamma \right), \tag{2.14}$$

which is a measure of particle inertia. This gives us a two-dimensional parameter space, which can be investigated to determine when inertial effects (as measured by $\widetilde{\mathrm{St}}$) are important, and when non-linear shape effects (as measured by ε) are important. Details are given in chapter 3.

We extend our analysis to include time dependent shear, more specifically oscillating shear. The flow is described by

$$K_{ij} = \delta_{i1}\delta_{j3}\kappa \cos(ft), \tag{2.15}$$

where f is a non-dimensional frequency, or Strouhal number, for the oscillating shear flow. It is important to remember that the equations describing the particle rotation were derived under the assumption that the flow around the particle could be accurately approximated by the steady Stokes equations. Oscillating shear violates the assumption that the flow is steady. However, as long as f is not significantly greater than unity, the time-derivative of the fluid velocity will still be insignificant compared with the viscous terms. This means we can still use the steady Stokes equations.

The use of an oscillating rate of shear means that the instantaneous Stokes number $\widetilde{\mathrm{St}}|\cos(ft)|$, and therefore the relative importance of particle inertia, will change during the oscillation period. How the particle rotates in the oscillating shear flow, is studied in detail in chapter 3.

2.4 Relevance to turbulent flow

Generally, we are interested not only in how a single prolate spheroid rotates in a simple shear flow, but also how millions of tiny prolate spheroids rotate in a turbulent flow. The question is if we can learn something about the latter, by studying the former. While the equations used to describe the rotation of each single particle in a direct numerical simulation of a turbulent flow are the same as those used for three-dimensional rotation of a single spheroid (Mortensen et al., 2008), the immense complexity of the turbulent velocity field makes it a very different kind of problem. Although it is difficult to relate specific results from chapter 3 to turbulent flow, some general observations are made.

Assuming a homogeneous isotropic turbulent flow, we can estimate an approximate mean velocity gradient as $\lambda = (\epsilon/\nu)^{1/2}$, where ϵ is the rate of viscous dissipation and ν is the kinematic viscosity. Then a Stokes number $\widetilde{\mathrm{St}}_\lambda$, based on λ (instead of κ), can provide valuable information about how important particle inertia will be and if $\mathcal{O}(1)$ instantaneous Stokes numbers are likely. As for the oscillating shear flow, the fluctuating velocity gradient in isotropic turbulence will cause the effective Stokes number to also frequently take values close to zero, which means that non-linear shape effects are always going to be important. Small-scale intermittency will cause local velocity gradients much greater than λ and probability density functions for the velocity gradients can be used to construct a probability distribution for the instantaneous Stokes number. This probability distribution can then be used to estimate the probability of finding particle Stokes numbers greater than the transitional Stokes number described in chapter 3, which will tell us how important inertial effects are.

Turbulent flows contain vortices of many different sizes, and therefore velocity fluctuations over a wide range of scales. In chapter 3, we observe that the particles are only responsive to oscillation frequencies within a certain range. In turbulent flows, this leads to a filtering of small-scale frequencies.

Chapter 3

Article 1: Chaotic rotation of inertial spheroids in oscillating shear flow

Published in Physics of Fluids 25 (2013)

PHYSICS OF FLUIDS **25**, 013303 (2013)

Chaotic rotation of inertial spheroids in oscillating shear flow

Christopher Nilsen[a] and Helge I. Andersson
Department of Energy and Process Engineering, Norwegian University of Science and Technology, N-7491 Trondheim, Norway

(Received 24 August 2012; accepted 20 December 2012; published online 31 January 2013)

The rotation of prolate spheroidal particles is studied in the flow-gradient plane of an oscillating creeping shear flow. Chaotic dynamics is observed for particles with strong inertia, and spheroids with aspect ratio 3:1 are seen to be the most prone to chaotic rotation. This makes the particles' long-term behaviour unpredictable, and also affects the particles' average statistics, such as the rotation energy. Chaos is only seen for Stokes numbers larger than a certain critical value, always greater than the Stokes number for which the particle rotation period in a constant shear rate transitions from long to short. This is because both inertial and nonlinear effects need to be significant for chaos to emerge. © *2013 American Institute of Physics*. [http://dx.doi.org/10.1063/1.4789376]

I. INTRODUCTION

The study of how particles move in a fluid has been given considerable attention throughout the last century, and it is of significance both in nature and in engineering applications. Most studies on particle suspensions are concerned with spherical particles; however, the sphere is not a suitable approximation to the shape of many types of particles. Non-spherical particles, the simplest of which is the ellipsoid, can often behave very differently from their spherical counterparts.

Particles transported in the human respiratory system are sometimes described as ellipsoids,[1,2] and so are the elongated wood fibres used in paper production.[3,4] In the latter case the orientation of each fibre is of particular interest, as it greatly affects the properties of the paper. Many types of ice crystals in clouds can be described as different kinds of ellipsoids, and an understanding of how these ice particles collide is important to describe the growth of crystals and the formation of snow.[5,6] In other cases it is not the orientation itself that is important, rather how it affects the rheology of the suspension. A study of the rotation of a single particle can be considered as the first step towards a rheological description.[7]

Jeffery[8] studied the motion of ellipsoidal particles in shear flow, and his results are frequently used when studying suspensions of ellipsoids. He derived equations for the torques on a general ellipsoid in a shearing Stokes flow. By neglecting both fluid and particle inertia, Jeffery was also able to find a solution for the orbit of an axisymmetric ellipsoid (spheroid) in a simple shear flow. He showed that the particle moved in a closed orbit, sometimes referred to as a Jeffery orbit, reminiscent of the motion of a kayak paddle. Hinch and Leal[9] studied the motion of non-axisymmetric ellipsoids, and showed that small deviations from axial symmetry could cause large changes in rotation. Nearly spherical ellipsoids were shown to behave similarly to general ellipsoids.

Further progress in the understanding of the effect of particle inertia was made by Lundell and Carlsson,[10] where the rotation of prolate spheroids of non-negligible inertia was studied by solving the angular momentum equations for the particles in a linear creeping shear flow. The particle inertia was seen to introduce a drift of the particle orientation towards the flow-gradient plane. Fluid inertia has been observed to introduce a similar effect,[11] and the effect of both fluid and particle

[a]Electronic mail: christopher.nilsen@ntnu.no.

 © 2013 American Institute of Physics

inertia was studied by Subramanian and Koch.[12] A review of the early contributions to the study of particle motions in viscous flow was written by Leal,[13] and a large number of experimental[14,15] and computational studies[16–20] of suspended ellipsoids have been carried out.

The effect of an external field on the motion of dipolar particles was investigated by Almog and Frankel.[21] The introduction of an external force can sometimes lead to chaotic rotation, as observed by Ramamohan *et al.*[22] for a periodically forced slender body in a simple shear flow. Applications of this phenomenon were discussed by Kumar, Kumar, and Ramamohan[23] and a review was written by Asokan *et al.*[24]

However, chaotic motion can also occur without the presence of an external force. Young *et al.*[25] found a period-doubling transition to chaos for viscous drops in a shear flow with sinusoidal temporal variation of vorticity. Yarin, Gottlieb, and Roisman[26] showed that long triaxial ellipsoids can exhibit chaotic rotation in simple shear flow, by studying non-inertial particles in creeping flow, while a similar observation was made for inertial particles by Lundell.[27] He observed chaotic rotation for certain aspect ratio combinations and for a range of Stokes numbers.

Although the motion of prolate spheroids in a shear flow with constant rate of shear is well documented, it is not clear how the spheroids will behave in a time-dependent shear flow. By simulating the spheroids in an oscillating shear flow, we will be able to see how the spheroids respond to different time scales in a simplified model. The effect of aspect ratio and inertia on the rotation of prolate spheroids in time-dependent shear flow, will be investigated. We want to see if prolate spheroids can exhibit chaotic rotation when subjected to an oscillating shear rate, and under what conditions this behaviour is prominent. We will also try to explain why chaotic rotation might occur, and what sort of implications these observations will have in real flows.

II. GOVERNING EQUATIONS

In a simple shear flow prolate spheroids with non-negligible inertia will tend to drift towards the flow-gradient plane,[10] ending up only rotating in this plane. In the present study we consider spheroids initially in the flow-gradient plane, which means that the particle will remain in this plane at all times. This greatly simplifies the dynamical system, maintaining at the same time the essential aspects of the nonlinear rotation problem we want to investigate. The solution to this simplified system will be the steady-state solution to the full three-dimensional problem.

We consider a prolate spheroid with semi-principal axes of length a and b, and aspect ratio $k = b/a$, rotating in a linear creeping shear flow. The surface of the spheroid is described by the equation

$$\frac{x^2}{a^2} + \frac{y^2}{b^2} + \frac{z^2}{b^2} = 1.$$

The coordinates xyz are defined within a particle frame of reference, that is to say the coordinate system is fixed on and rotates with the particle. The flow is defined in a second non-rotating reference frame $x'y'z'$ as

$$\boldsymbol{u}' = \left(\kappa g(t) z', 0, 0\right),$$

where $\kappa g(t)$ is the rate of shear, with $\kappa[\mathrm{s}^{-1}]$ a constant and $g(t)$ a non-dimensional function of non-dimensional time t.

The rotation of a spheroid is governed by Euler's equations:

$$\boldsymbol{I} \cdot \boldsymbol{\omega} + \boldsymbol{\omega} \times (\boldsymbol{I} \cdot \boldsymbol{\omega}) = \boldsymbol{M},$$

and the torques from the shear flow were derived by Jeffery[8] as

$$M_1 = \tfrac{32\pi\mu}{3(\beta_0+\gamma_0)} (\Omega_{32} - \omega_1),$$

$$M_2 = \tfrac{16\pi\mu}{3(b^2\gamma_0+a^2\alpha_0)} \left((b^2 - a^2)S_{13} + (b^2 + a^2)(\Omega_{13} - \omega_2)\right),$$

$$M_3 = \tfrac{16\pi\mu}{3(a^2\alpha_0+b^2\beta_0)} \left((a^2 - b^2)S_{12} + (a^2 + b^2)(\Omega_{21} - \omega_3)\right),$$

where α_0, β_0, γ_0 are constants and $\boldsymbol{S}$ and $\boldsymbol{\Omega}$ are the symmetric and antisymmetric parts of the velocity gradient tensor $\nabla \boldsymbol{u}$ in the particle frame. For initial conditions in the flow-gradient plane this simplifies to the second-order ordinary differential equation

$$\frac{\mathrm{St}}{80}\frac{1-\varepsilon}{1+\varepsilon}\left(\alpha_0+\frac{1-\varepsilon}{1+\varepsilon}\gamma_0\right)\ddot{\phi}=\varepsilon\left(\frac{1}{2}-\cos^2\phi\right)g(t)+\frac{1}{2}g(t)-\dot{\phi}, \tag{1}$$

where

$$\mathrm{St}=\frac{\kappa(2a)^2}{\nu}\frac{\rho_p}{\rho_f}=\mathrm{Re}\frac{\rho_p}{\rho_f}$$

is the non-dimensional Stokes number for Reynolds number Re. The parameter ε is a function of the aspect ratio k of the prolate spheroid and is defined as

$$\varepsilon=\frac{1-k^2}{1+k^2},$$

with $\varepsilon=0$ for spherical particles and $\varepsilon=1$ for infinitely thin spheroids. The dots denote differentiation with respect to the non-dimensional time t, and ϕ is the angle between the x' and x axes. The time is made non-dimensional with the rate of shear constant κ. The densities of the particle and fluid are ρ_p and ρ_f respectively, and ν is the kinematic viscosity. The non-dimensional coefficients α_0 and γ_0 are given by

$$\alpha_0=\int_0^\infty\frac{d\psi}{(1+\psi)\left\{(1+\psi)\left(k^2+\psi\right)\left(k^2+\psi\right)\right\}^{\frac{1}{2}}},$$

$$\gamma_0=\int_0^\infty\frac{d\psi}{\left(k^2+\psi\right)\left\{(1+\psi)\left(k^2+\psi\right)\left(k^2+\psi\right)\right\}^{\frac{1}{2}}},$$

and both are equal to 2/3 for a spherical particle.

We will refer to the non-dimensional group in front of the angular acceleration $\ddot{\phi}$ as the modified Stokes number, $\widetilde{\mathrm{St}}$, because it simplifies the equation, and also, as we will see, clarifies the results. $\widetilde{\mathrm{St}}$ is finite for all values of ε between 0 and 1, and prescribing $\widetilde{\mathrm{St}}$ and ε separately does not cause any inconsistencies.

We can write Eq. (1) as an autonomous system of first-order ordinary differential equations:

$$\begin{aligned}\dot{\chi}_1&=\chi_2,\\ \dot{\chi}_2&=\left\{\varepsilon\left(\tfrac{1}{2}-\cos^2\chi_1\right)g(\chi_3)+\tfrac{1}{2}g(\chi_3)-\chi_2\right\}/\widetilde{\mathrm{St}},\\ \dot{\chi}_3&=1,\end{aligned}$$

or in vector notation $\dot{\boldsymbol{\chi}}=\boldsymbol{f}(\boldsymbol{\chi})$. The divergence of $\boldsymbol{f}$ is then $\nabla\cdot\boldsymbol{f}=-1/\widetilde{\mathrm{St}}$, which means that volumes in phase space ($\boldsymbol{\chi}$ space) contract as $\exp(-t/\widetilde{\mathrm{St}})$. The system is dissipative and for all initial conditions the solution will approach a limiting set of zero volume in phase space. This makes $\widetilde{\mathrm{St}}$ an important time-scale for the dynamical system.

The equations have been solved numerically using the ordinary differential equation (ODE) solver LSODE from the package ODEPACK,[28,29] using the non-stiff Adams methods. We want to be able to accurately recognise chaotic particle rotation, and we use the Lyapunov exponents to do this. For a chaotic system an initial separation δ_0 between two trajectories in phase space will diverge exponentially to $\delta(t)$. The rate of divergence is determined by the maximum Lyapunov exponent

$$\lambda=\lim_{t\to\infty}\frac{1}{t-t_0}\ln\frac{\delta(t)}{\delta_o}.$$

We use a normalisation approach,[30,31] and average over a total of 1000 normalisations. Because of the periodic time dependence of χ_3, δ_0 and $\delta(t)$ are measured in $(\chi_1,\chi_2)=(\phi,\dot{\phi})$, and we average over 10 different initial conditions evenly distributed in one χ_3-period. An initial separation $\delta_0=10^{-6}$ is used, and we normalise when $\delta(t)$ reaches 10^{-5} or 10^{-7}. All other statistical quantities

are averaged over 1000 periods of $g(t)$. The simulations are started from an initial condition on the attractor, found by first simulating until $t = 2000\widetilde{\mathrm{St}}$ from a random initial condition.

III. CONSTANT SHEAR RATE

We begin by studying Eq. (1) with the simplest possible shear rate function $g(t) = 1$, which gives us the equation

$$\widetilde{\mathrm{St}}\,\ddot{\phi} = \varepsilon\left(\frac{1}{2} - \cos^2\phi\right) + \frac{1}{2} - \dot{\phi}. \tag{2}$$

This allows us to illustrate some basic features of the physical system before we consider more complex cases.

For spherical particles $\varepsilon = 0$ the equation simplifies to

$$\widetilde{\mathrm{St}}\ddot{\phi} = \frac{1}{2} - \dot{\phi},$$

with the solution

$$\phi(t) = \widetilde{\mathrm{St}}\left(\dot{\phi}(0) - \frac{1}{2}\right)\left(1 - e^{-t/\widetilde{\mathrm{St}}}\right) + \frac{1}{2}t + \phi(0),$$

where $\widetilde{\mathrm{St}} = \mathrm{St}/60$ for spherical particles. The solution describes a temporal development starting from the initial condition $(\phi(0), \dot{\phi}(0))$ and approaching, after an initial exponential transient, a steady rotation with angular velocity $\dot{\phi} = 1/2$. This gives a rotation period of $T_H = 4\pi$.

Non-inertial particles represent another analytically solvable degenerate case. We assume that $\widetilde{\mathrm{St}} = 0$ and get

$$\dot{\phi} = \varepsilon\left(\frac{1}{2} - \cos^2(\phi)\right) + \frac{1}{2}.$$

Integration then yields the solution

$$\tan\phi = \frac{\sqrt{1-\varepsilon^2}}{1+\varepsilon}\tan\left(\frac{1}{2}\sqrt{1-\varepsilon^2}t\right),$$

which describes a closed orbit rotation with period $T_J = 4\pi/\sqrt{1-\varepsilon^2}$. This is also the solution found by Jeffery.[8] For a spherical non-inertial particle a period of $T = 4\pi$ is found, the same as for the inertial particle. The rotation period is therefore unaffected by particle inertia for a spherical particle.

In order to see the combined effect of particle inertia and shape, we have solved the system numerically for a wide range of $\widetilde{\mathrm{St}}$ and ε. Figure 1(a) shows how the rotation period depends on the Stokes number for three selected values of ε. The rotation period is equal to the non-inertial rotation period T_J for low Stokes numbers and then drops to the rotation period of spherical particles T_H when St is sufficiently high. This suggests that the particles behave as if they are either non-inertial or spherical, except in the transitional range of St.

The modified Stokes number $\widetilde{\mathrm{St}}$ is plotted against a normalised rotation period $\widetilde{T}$ in Figure 1(b), to be able to see more clearly how the rotation period changes. There is a transition to the low rotation period when $\widetilde{\mathrm{St}}$ is around 1, but the shape of the particle determines how gradual the transition is, with a steeper gradient for more elongated particles.

Inertia clearly has a different effect on highly elongated particles than it does on almost spherical particles. The second derivative of $\widetilde{T}$ with respect to $\widetilde{\mathrm{St}}$ is plotted in Figure 2(a) together with the interpolating function $-4.0\sqrt{1-\varepsilon^2}$. The favourable agreement this function shows with the numerical data suggests that

$$\widetilde{T} = 1 - 2.0\sqrt{1-\varepsilon^2}\,\widetilde{\mathrm{St}}^2 \tag{3}$$

is a good approximation for low values of $\widetilde{\mathrm{St}}$. The considerable deviations for $\varepsilon < 0.4$ are caused by the difficulties in estimating the second derivative when $\sqrt{1-\varepsilon^2} \approx 1$.

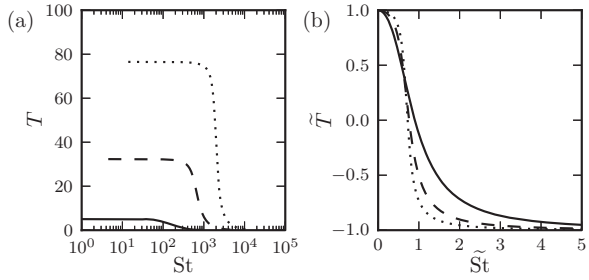

FIG. 1. Effect of particle shape on rotation period in constant shear for $\varepsilon = 0.7$ (solid), 0.96 (dashed), and 0.99 (dotted). (a) Rotation period T as a function of St and (b) normalised rotation period $\widetilde{T}$ as function of $\widetilde{\mathrm{St}}$. $\widetilde{T}$ is defined as $\widetilde{T} = (T - (T_J + T_H)/2)/((T_J - T_H)/2)$.

The point where $\widetilde{T} = 0$ in Figure 1(b) corresponds with the point where T is equal to $(T_J + T_H)/2$ in Figure 1(a). The corresponding Stokes number is $\mathrm{St}_{0.5}$ (following the definition of Lundell and Carlsson[10]) and the modified Stokes number is $\widetilde{\mathrm{St}}_{0.5}$. Lundell and Carlsson[10] suggested that $\widetilde{\mathrm{St}}_{0.5} \approx 0.8$, while Figure 2(b), showing $\widetilde{\mathrm{St}}_{0.5}$ for different ε, indicates that $\widetilde{\mathrm{St}}_{0.5}$ is accurately predicted as

$$\widetilde{\mathrm{St}}_{0.5} = 0.7 + 0.3\left(1 - \varepsilon^2\right)^{0.625}. \tag{4}$$

This simple expression makes it easy to compute $\widetilde{\mathrm{St}}_{0.5}$, and thus also $\mathrm{St}_{0.5}$, for a given particle shape. The width of the transitional range can be defined as $\widetilde{\mathrm{St}}_{0.05} - \widetilde{\mathrm{St}}_{0.95}$, which is accurately estimated as $\widetilde{\mathrm{St}}_{0.05} - \widetilde{\mathrm{St}}_{0.95} = 4.12(1 - \varepsilon)^{0.375}$.

IV. OSCILLATING SHEAR RATE

We want to investigate the effects of an oscillating shear rate, and choose a shear rate function $g(t) = \cos(ft)$, where f is a non-dimensional frequency for the oscillation and can be thought of as an imposed Strouhal number. The Stokes number is defined, as in Sec. II, using κ, which in this case is the maximum shear rate. A Stokes number based on the instantaneous shear rate would be $\widetilde{\mathrm{St}}|\cos(ft)|$. The differential equation describing the system is then

$$\widetilde{\mathrm{St}}\ddot{\phi} = \varepsilon\left(\frac{1}{2} - \cos^2\phi\right)\cos(ft) + \frac{1}{2}\cos(ft) - \dot{\phi}. \tag{5}$$

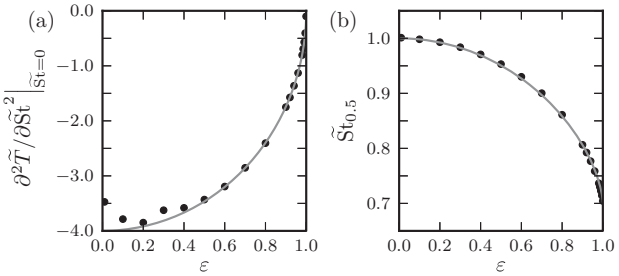

FIG. 2. Effect of particle shape ε on (a) second-order derivative of $\widetilde{T}$ for $\widetilde{\mathrm{St}} = 0$ and (b) transition Stokes number $\widetilde{\mathrm{St}}_{0.5}$. Solid lines (grey) are interpolation functions $-4.0\sqrt{1 - \varepsilon^2}$ and (4).

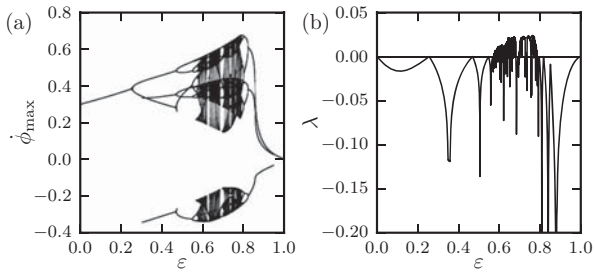

FIG. 3. Period-doubling route to chaos for ε between 0 and 1, and St $= 400$, $f = 0.2$. (a) Orbit diagram displaying local maxima of $\dot{\phi}$ and (b) the corresponding maximum Lyapunov exponent.

This is a second-order ordinary differential equation with three parameters $\widetilde{\mathrm{St}}$, ε, and f, that we solve numerically for different parameter values, in order to see how they affect the solution. In the derivation of the expressions for the torque components on the particle, it is assumed that we have a steady flow, which the introduction of an oscillating shear rate would seem to violate. However, as long as the Strouhal number of the imposed temporal variation (f) is not significantly greater than unity, the transient and the nonlinear effects are of the same order of magnitude, and we can safely use the expressions derived for stationary flows, provided that the Reynolds number is sufficiently low.

The orbit diagram (Figure 3(a)) shows the period of the orbits by plotting all local maxima of $\dot{\phi}$ for a range of ε values. The dense regions are indicative of chaos, and we can see that chaos emerges through a series of period-doubling bifurcations in ε. In this particular case we have St $= 400$ and $f = 0.2$. In Figure 3(b) a corresponding plot of the maximum Lyapunov exponent λ is shown, and confirms that the dense regions in Figure 3(a) are truly chaotic, with $\lambda > 0$ for f roughly between 0.6 and 0.8. We also see that λ approaches 0 in the period-doubling bifurcations, as expected.

This shows that chaotic rotation can occur for this system, and that the geometry of the spheroid, described by ε, has an important effect on the dynamics of the particle rotation. Both the smoothness of the λ graph in Figure 3(b), and its correspondence with the orbit diagram, are good indicators of the sampling time being sufficient.

To illustrate what chaotic rotation means for the evolution of the phase space variables, we plot $\dot{\phi}$ as a function of time, together with $(\dot{\phi}, \cos\phi)$ phase portraits in Figure 4. Figures 4(a)–4(c) show $\dot{\phi}$ between $t = 1000$ and $t = 1200$ for $\varepsilon = 0.2$, 0.5, and 0.75, respectively. Figures 4(d)–4(f) show the $(\dot{\phi}, \cos\phi)$ phase portrait for the same values of ε.

Several bifurcations have occurred between $\varepsilon = 0.2$ and 0.5, and it is clear in Figures 4(a) and 4(b) that we go from a period-1 orbit to a more complex behaviour. The corresponding phase portraits reveal significant differences, and although we no longer have a period-1 orbit for $\varepsilon = 0.5$, the solution is clearly still periodic. In Figure 4(c), however, the particle rotation is no longer periodic, as ε is within the chaotic range in Figure 3. Figure 4(f) illustrates this by displaying an attractor that is exceedingly complex, but still very organised. This type of strange attractor is common in chaotic systems.

We see that chaotic rotation is possible, and how the chaos presents itself in the phase space variables. However, we have only so far studied a small part of the $(\widetilde{\mathrm{St}}, \varepsilon, f)$ parameter space, and a more complete investigation of this parameter space is necessary for a better understanding of the dynamics of the spheroidal particle. It is also important to see how the chaotic rotation affects other aspects of the particle dynamics.

A comprehensive study of the dynamics of the particle has been conducted for 2048 f-values between 0 and 1.5, 179 $\widetilde{\mathrm{St}}$-values between 0 and 10, and 17 ε-values between 0 and 0.995. This amounts to a total of more than 6×10^6 different parameter combinations, and should allow us to see more clearly how the different parameters affect the solution.

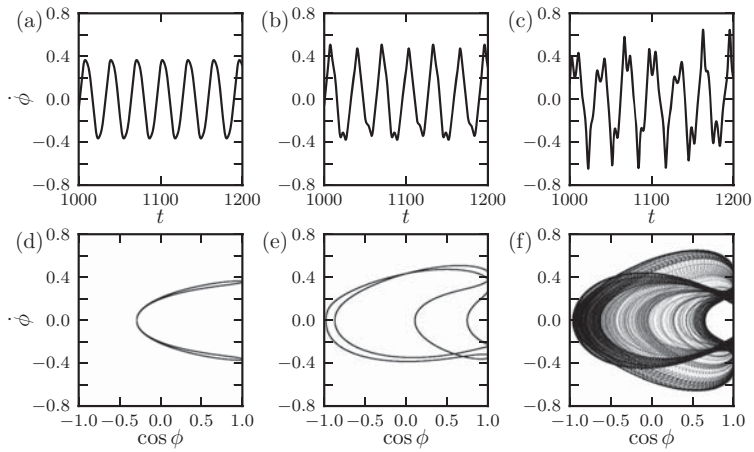

FIG. 4. Complex particle dynamics for $\mathrm{St} = 400$ and $f = 0.2$. Angular velocity as a function of time for (a) $\varepsilon = 0.2$, (b) 0.5, and (c) 0.75, and (d–f) corresponding $(\dot{\phi}, \cos\phi)$ phase portraits.

In Figure 5 the maximum Lyapunov exponent is plotted as a function of f for $\varepsilon = 0.8$ and $\widetilde{\mathrm{St}} = 0.7$ (a), 1.0 (b) and 3.0 (c). The average rotational kinetic energy $\frac{1}{2}\overline{\dot{\phi}^2}$ (d–f), and the correlation factor between particle and fluid rotation rate $\rho(\dot{\phi}, \cos ft) = \overline{\dot{\phi}\cos ft}/\sqrt{\overline{\dot{\phi}^2}\overline{\cos^2 ft}}$ (g–i), are also plotted in Figure 5.

For f larger than the value indicated by the dashed line, the particle simply rocks back and forth around $\phi = 0$, never crossing $\phi = \pi/2$. It is clear that the particle dynamics for these values of f are rather uneventful, consisting of non-chaotic low energy rocking around $\phi = 0$. Below this frequency, the particle dynamics are much more complex, and the differences between the three different $\widetilde{\mathrm{St}}$ are more pronounced. The maximum Lyapunov exponent is only positive for $\widetilde{\mathrm{St}} = 3.0$, in a range of f between 0.0 and 0.2.

There are only subtle differences between $\widetilde{\mathrm{St}} = 0.7$ and 1.0 for the energy and rotation correlation, but the maximum Lyapunov exponent is significantly changed for $\widetilde{\mathrm{St}} = 1.0$. For $\widetilde{\mathrm{St}} = 3.0$ however, the change in λ also has effects on the other quantities. Not surprisingly, the particle rotation is much less correlated with the fluid rotation when $\lambda > 0$. Interestingly, also the kinetic energy drops significantly at the peaks in λ. This shows that the change in rotation caused by the chaos has significant effects on the long-term statistical properties of the particle dynamics.

It is clear from Figure 5 that chaos is an effect associated with strong particle inertia, i.e., large $\widetilde{\mathrm{St}}$. This suggests that there is a critical $\widetilde{\mathrm{St}}$ ($\widetilde{\mathrm{St}}_c$), below which chaos cannot occur for a given ε, regardless of the value of f. This critical modified Stokes number $\widetilde{\mathrm{St}}_c$ is shown in Figure 6(a) for a set of ε values. The points appear to fit quite neatly on the line

$$\widetilde{\mathrm{St}}_c = -0.1 + 0.85/\varepsilon^2$$

for the included ε values. For $\varepsilon < 0.3$, no chaotic solution was found for $\widetilde{\mathrm{St}} \lesssim 10$, but that does not mean that chaos is not possible given a sufficiently large $\widetilde{\mathrm{St}}$. We can rescale $\widetilde{\mathrm{St}}_c$ back to the standard Stokes number and get St_c, shown in Figure 6(b). We cannot necessarily trust the interpolation function to accurately extrapolate St_c to values lower than $\varepsilon = 0.3$, where no data is available.

Strong inertia is required for chaotic rotation of any particle shape, and especially if ε is close to 0 or 1. However, there is a region from $\varepsilon = 0.4$ to $\varepsilon = 0.92$, in which chaos is possible for St as low as 500. The lowest St_c is seen at $\mathrm{St}_c = 319$ for $\varepsilon = 0.8$. Also plotted in Figure 6 are $\widetilde{\mathrm{St}}_{0.5}$ and $\mathrm{St}_{0.5}$. We see that the critical Stokes number is always greater than the Stokes number for which the

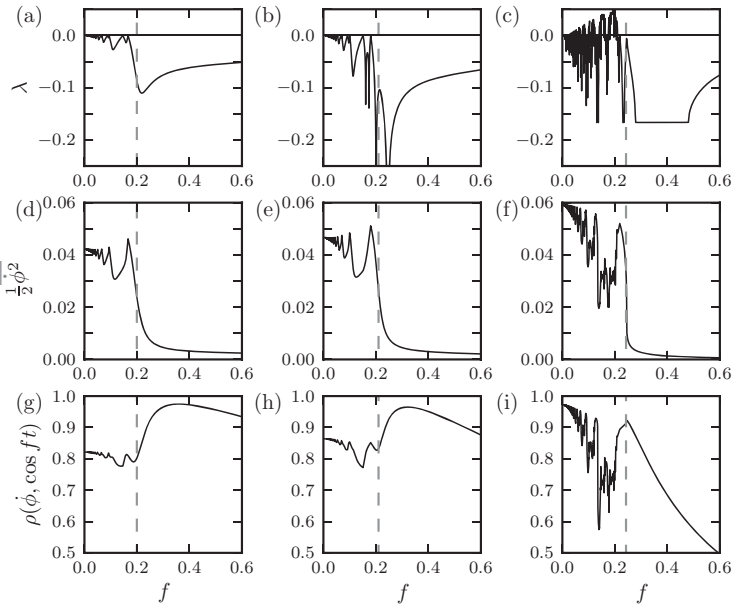

FIG. 5. Effect of f on $\varepsilon = 0.8$ spheroid. Maximum Lyapunov exponent λ for (a) $\widetilde{\mathrm{St}} = 0.7$, (b) 1.0, and (c) 3.0, as well as (d–f) rotational kinetic energy $\frac{1}{2}\overline{\dot{\phi}^2}$, and (g–i) particle-fluid rotation rate correlation factor $\rho(\dot{\phi}, \cos ft)$. The dashed vertical lines (grey) are the f-values for which $\max(\phi(t)) - \min(\phi(t)) < \pi$.

transition in rotation period occurs. However, the two lines approach each other for increasing ε, and almost overlap for $\varepsilon > 0.9$.

Chaos is only possible for certain shear oscillation frequencies, as illustrated in Figure 7(a). The lowest and highest chaotic f values are plotted for every $\widetilde{\mathrm{St}}$, and for $\varepsilon = 0.4$, 0.7, and 0.92. Increasing ε expands the chaotic regime in the $(\widetilde{\mathrm{St}}, f)$ plane, but chaos is nevertheless primarily found in a range of f roughly between 0.0 and 0.2. For $\varepsilon = 0.92$ (and for larger values of ε) positive λ-values are sometimes seen for even higher f-values, as observed in the upper right corner of Figure 7(a). These positive λ-values present themselves as very narrow peaks for particular f-values, and do not affect the notion that chaos is primarily found for $f < 0.2$.

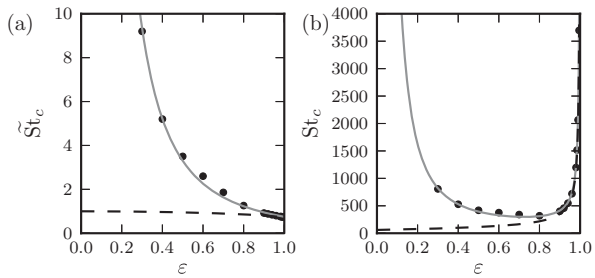

FIG. 6. (a) Critical modified Stokes number $\widetilde{\mathrm{St}}_c$ below which chaos is not observed, plotted together with the function $-0.1 + 0.85/\varepsilon^2$ (solid grey line). (b) The critical Stokes number St_c is shown with the same interpolation function (solid grey line). The dashed lines are $\widetilde{\mathrm{St}}_{0.5}$ and $\mathrm{St}_{0.5}$.

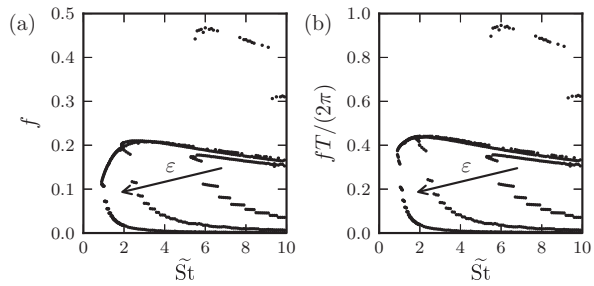

FIG. 7. (a) Lowest and highest frequency f with $\lambda > 0$ for $\varepsilon = 0.4$, 0.7, and 0.92, for a given $\widetilde{\mathrm{St}}$, and (b) normalised with the rotation period T.

When rescaling f with the rotation time period T, at constant shear rate (Figure 7(b)), we see that chaos is found when $2\pi/f \gtrsim 2T$. It is important to remember that T is not a relevant timescale throughout the entire period of the oscillating shear function. As the rate of shear varies between 0 and κ, the relevant rotation period $T(|\cos(ft)|\widetilde{\mathrm{St}})$ will change accordingly. However, because the rescaling used in Figure 7(b) gives domains of similar shapes for the different aspect ratios, $T(\widetilde{\mathrm{St}})$ seems to be a suitable time scale. Increased ε reduces the lowest f-value where chaos is possible because the increased rotation period at $\widetilde{\mathrm{St}} = 0$ means that the particle can be affected by a wider range of time scales. Increased $\widetilde{\mathrm{St}}$ reduces the f-values for which chaos is found as increased inertia makes the particles more sluggish.

The degree of chaos can be measured by the maximum Lyapunov exponent. To determine which particle shape exhibits the strongest chaotic divergence, the maximum value of the maximum Lyapunov exponent $\lambda_{\max}$ is shown in Figure 8. This is the maximum obtainable value of λ for a given ε. There is a peak in $\lambda_{\max}$ at $\varepsilon = 0.8$ with a value of $\lambda_{\max} = 0.053$. This value is found for $\widetilde{\mathrm{St}} = 3.9$ and $f = 0.194$.

Following the definition of the Lyapunov exponent, a value of 0.053 indicates that the distance between two trajectories on the attractor, with initial separation $\delta_0 = 10^{-6}$, will have grown to $\delta(t) = 0.1$ after $t \approx 217$. In Figure 9(a) we can see $\phi(t)$ for two trajectories on the attractor, with initial separation equal to 10^{-6}, diverge. There is noticeable separation from around $t = 250$, which corresponds to 7.7 complete periods in the oscillating shear flow.

In Figure 9(b) the orientation of the two particles are viewed during a larger time span. The chaotic divergence eventually leads to completely different orientations. The particle rotation is also very persistent, with one of the particles rotating more than 40 complete rotations in one direction.

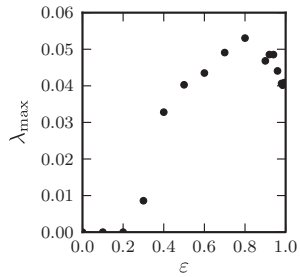

FIG. 8. Maximum possible value of the maximum Lyapunov exponent for various ε.

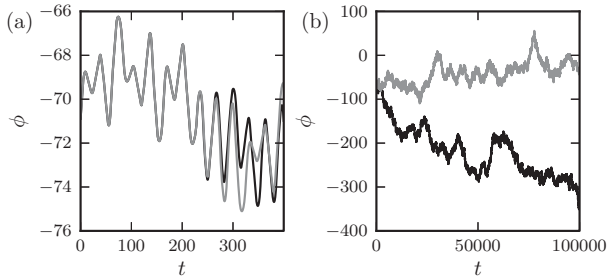

FIG. 9. Particle orientation angle for two particle trajectories with initial separation 10^{-6} and $\varepsilon = 0.8$, $\widetilde{\mathrm{St}} = 3.9$, $f = 0.194$, for (a) a short and (b) a long time window.

V. DISCUSSION AND CONCLUSION

We have shown that a prolate spheroid rotating in the flow-gradient plane of an oscillating shear flow can exhibit complex chaotic rotation for strong particle inertia. Spheroids with $\varepsilon = 0.8$, corresponding to a 3:1 aspect ratio, have the strongest chaotic divergence and also chaos for the lowest Stokes numbers. Chaos only occurs for oscillation frequencies lower than half the rotation frequency the particle would have in a constant shear rate. This is because the high inertia slows down the particle when the shear rate is rapidly changing. Even though we have limited the study to rotation in the flow-gradient plane, we believe that the results are relevant in more complicated situations, where the particle undergoes three-dimensional rotation. Rotation in the flow-gradient plane is the steady-state solution for an inertial prolate spheroid,[10] and the dynamics observed in the flow-gradient plane should give relevant information about how the particle behaves when rotating around its minor axis.

Lundell[27] found chaotic particle dynamics for triaxial ellipsoids for Stokes numbers below a certain critical value, always less than $\mathrm{St}_{0.5}$. In the present work, chaos is only found for Stokes numbers larger than a critical value, always greater than $\mathrm{St}_{0.5}$. It is apparent that the two types of chaotic rotation are caused by different effects. Lundell's chaos is caused by a three-dimensional instability associated with the triaxial particle shape. This instability is suppressed by inertia because inertia forces the particle towards the flow-gradient plane. For a spheroid already rotating in the flow-gradient plane, an oscillating shear rate has been shown to cause chaos, provided that there is sufficient inertia.

A possible explanation for the chaos seen at high Stokes numbers is that when $\widetilde{\mathrm{St}}$ is sufficiently high, $|\cos(ft)|\widetilde{\mathrm{St}}$ will move through the transitional range observed in Figure 1 in each oscillation period. This means that both inertial and nonlinear effects will be important during parts of the rotation cycle, which is what is believed to cause the chaos. This is illustrated in Figure 10 where we

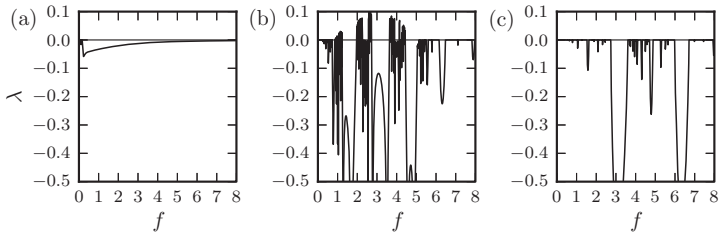

FIG. 10. Maximum Lyapunov exponent as function of f, for $\varepsilon = 0.8$ and $\widetilde{\mathrm{St}} = 0.5$, with shear rate function $g(t) = \beta + \cos(ft)$ and (a) $\beta = 0.5$, (b) $\beta = 2.0$, and (c) $\beta = 3.5$. Positive λ values are only found for $\beta = 2.0$ and at much higher f-values than we have seen previously.

see that adding a constant shear rate β can push the particle's range of instantaneous Stokes numbers into the transitional range to cause chaos. If the constant shear rate is sufficiently large the particle will be inertia-driven during the entire rotation cycle, and there is no chaotic rotation.

Huang *et al.*[20] demonstrated that Jeffery's equations are valid approximations at $\mathrm{Re} = 0.5$. With a density ratio around 1000, we get a Stokes number around 500, making chaotic rotation a real possibility for particles with ε between 0.4 and 0.92. In an oscillating shear flow such as Stokes' second problem (see, e.g., Schlichting and Gersten,[32] page 129), strongly inertial particles can at certain frequencies exhibit strong enough chaotic divergence to make the particle orientation completely unpredictable after an order of 10 fluid oscillation periods. In addition to making it impossible to predict the long term behaviour of the particle rotation, the chaos also affects the rotation energy of the particle in such a way that small changes in the frequency can lead to dramatic changes in the average energy of the particle. The chaotic behaviour of the particle may even affect the rheological properties of a sufficiently dense particle-fluid mixture.[24]

Pure oscillating shear flows are not all that common in real applications, but several flows, such as wakes and jets, exhibit periodicity, and thus some of the effects seen here might be observed in such flows. In addition to this, the particle's motion in an oscillating shear flow could also reveal something about how particles are affected by the velocity fluctuations at different time scales found in turbulent flows. Knowledge of how certain frequencies excite certain particles, could help understand how particles rotate in a turbulent flow.

In a turbulent boundary layer or channel flow, a mean shear rate co-exists with a fluctuating shear rate associated with the turbulence. The time scales of the turbulent motions extend over a wide spectrum of scales; they also vary somewhat with the distance from the wall. The results obtained in the present study may indicate whether or not chaotic rotation of prolate spheroids can occur in a given turbulent flow. Moreover, if chaotic rotation is likely to occur, one might expect an anomalous interaction between the spheroids and the turbulent flow.

The results presented here are based on the assumption of negligible fluid inertia, and it remains to be seen how fluid inertia would affect the chaotic particle rotation. Computational or experimental studies could be used to clarify the effect of fluid inertia, yet extensive parameter sweeps would be time-consuming. Extending the present work to include three-dimensional rotation in an oscillating shear flow, might also reveal interesting new effects. As we have seen briefly here, adding a constant rate of shear dramatically changes the dynamics of the particle, and this could be investigated further.

ACKNOWLEDGMENTS

We gratefully acknowledge stimulating discussions enabled by COST Action FP1005, funded by the European Science Foundation.

[1] Z. Zhang and C. Kleinstreuer, "Airflow structures and nano-particle deposition in a human upper airway model," J. Comput. Phys. **198**, 178–210 (2004).
[2] G. Miserocchi, G. Sancini, F. Mantegazza, and G. Chiappino, "Translocation pathways for inhaled asbestos fibers," Environ. Health **7**, 4 (2008).
[3] J. A. Olson, I. Frigaard, C. Chan, and J. P. Hämäläinen, "Modeling a turbulent fibre suspension flowing in a planar contraction: The one-dimensional headbox," Intl. J. Multiphase Flow **30**, 51–66 (2004).
[4] F. Lundell, L. D. Söderberg, and P. H. Alfredsson, "Fluid mechanics of papermaking," Annu. Rev. Fluid Mech. **43**, 195–217 (2011).
[5] A. P. Khain and I. L. Sednev, "Simulation of hydrometeor size spectra evolution by water-water, ice-water and ice-ice interactions," Atmos. Res. **36**, 107–138 (1995).
[6] A. Khain, A. Pokrovsky, M. Pinsky, A. Seifert, and V. Phillips, "Simulation of effects of atmospheric aerosols on deep turbulent convective clouds using a spectral microphysics mixed-phase cumulus cloud model. Part I: Model description and possible applications," J. Atmos. Sci. **61**, 2963–2982 (2004).
[7] C. J. S. Petrie, "The rheology of fibre suspensions," J. Non-Newtonian Fluid Mech. **87**, 369–402 (1999).
[8] G. B. Jeffery, "The motion of ellipsoidal particles immersed in a viscous fluid," Proc. R. Soc. Lond. A **102**, 161–179 (1922).
[9] E. J. Hinch and L. G. Leal, "Rotation of small non-axisymmetric particles in a simple shear flow," J. Fluid Mech. **92**, 591–607 (1979).
[10] F. Lundell and A. Carlsson, "Heavy ellipsoids in creeping shear flow: Transitions of the particle rotation rate and orbit shape," Phys. Rev. E **81**, 016323 (2010).

[11] G. Subramanian and D. L. Koch, "Inertial effects on fibre motion in simple shear flow," J. Fluid Mech. **535**, 383–414 (2005).
[12] G. Subramanian and D. L. Koch, "Inertial effects on the orientation of nearly spherical particles in simple shear flow," J. Fluid Mech. **557**, 257–296 (2006).
[13] L. G. Leal, "Particle motions in a viscous fluid," Annu. Rev. Fluid Mech. **12**, 435–476 (1980).
[14] G. I. Taylor, "The motion of ellipsoidal particles in a viscous fluid," Proc. R. Soc. Lond. A **103**, 58–61 (1923).
[15] J. R. T. Seddon and T. Mullin, "The motion of a prolate ellipsoid in a rotating Stokes flow," J. Fluid Mech. **583**, 123–132 (2007).
[16] Z. Yu, N. Phan-Thien, and R. I. Tanner, "Rotation of a spheroid in a Couette flow at moderate Reynolds numbers," Phys. Rev. E **76**, 026310 (2007).
[17] P. H. Mortensen, H. I. Andersson, J. J. J. Gillissen, and B. J. Boersma, "Dynamics of prolate ellipsoidal particles in a turbulent channel flow," Phys. Fluids **20**, 093302 (2008).
[18] C. Marchioli, M. Fantoni, and A. Soldati, "Orientation, distribution, and deposition of elongated, inertial fibers in turbulent channel flow," Phys. Fluids **22**, 033301 (2010).
[19] H. I. Andersson, L. Zhao, and M. Barri, "Torque-coupling and particle–turbulence interactions," J. Fluid Mech. **696**, 319–329 (2012).
[20] H. Huang, X. Yang, M. Krafczyk, and X.-Y. Lu, "Rotation of spheroidal particles in Couette flows," J. Fluid Mech. **692**, 369–394 (2012).
[21] Y. Almog and I. Frankel, "The motion of axisymmetric dipolar particles in homogeneous shear flow," J. Fluid Mech. **289**, 243–261 (1995).
[22] T. R. Ramamohan, S. Savithri, R. Sreenivasan, and C. C. S. Bhat, "Chaotic dynamics of a periodically forced slender body in a simple shear flow," Phys. Lett. A **190**, 273–278 (1994).
[23] C. V. A. Kumar, K. S. Kumar, and T. R. Ramamohan, "Chaotic dynamics of periodically forced spheroids in simple shear flow with potential application to particle separation," Rheol. Acta **34**, 504–511 (1995).
[24] K. Asokan, C. V. A. Kumar, J. Dasan, K. Radhakrishnan, K. S. Kumar, and T. R. Ramamohan, "Review of chaos in the dynamics and rheology of suspensions of orientable particles in simple shear flow subject to an external periodic force," J. Non-Newtonian Fluid Mech. **129**, 128–142 (2005).
[25] Y.-N. Young, J. Blawzdziewicz, V. Cristini, and R. H. Goodman, "Hysteretic and chaotic dynamics of viscous drops in creeping flows with rotation," J. Fluid Mech. **607**, 209–234 (2008).
[26] A. L. Yarin, O. Gottlieb, and I. V. Roisman, "Chaotic rotation of triaxial ellipsoids in simple shear flow," J. Fluid Mech. **340**, 83–100 (1997).
[27] F. Lundell, "The effect of particle inertia on triaxial ellipsoids in creeping shear: From drift toward chaos to a single periodic solution," Phys. Fluids **23**, 011704 (2011).
[28] A. C. Hindmarsh, "ODEPACK, a systematized collection of ODE solvers," *Scientific Computing*, edited by R. S. Stepleman *et al.* (North-Holland, Amsterdam, 1983), Vol 1, pp. 55–64.
[29] K. Radhakrishnan and A. C. Hindmarsh, "Description and use of LSODE, the Livermore solver for ordinary differential equations," *Tech. Rep.* (Lawrence Livermore National Laboratory, 1993).
[30] G. Benetting, L. Galgani, and J.-M. Strelcyn, "Kolmogorov entropy and numerical experiments," Phys. Rev. A **14**, 2338–2345 (1976).
[31] A. Wolf, J. B. Swift, H. L. Swinney, and J. A. Vastano, "Determining Lyapunov exponents from a time series," Physica D **16**, 285–317 (1985).
[32] H. Schlichting and K. Gersten, *Boundary-Layer Theory* (Springer, Heidelberg, 2000).

Part II

Numerical turbulence

Chapter 4

Spectral element direct numerical simulation

Direct numerical simulations (DNS) of turbulent flow have the potential to provide valuable insight into the physics of turbulence. Spectral methods have typically been favoured in these simulations, due to their superior efficiency. In a newly developed DNS code, we use spectral element discretisation to allow more complex geometries, while retaining the exponential convergence of spectral methods. This chapter describes the numerical methods used in the DNS code.

Most of the information about spectral-element discretisation is from Deville et al. (2002), Karniadakis and Sherwin (2005) and Rønquist (2012). References to specific results or methods are given when applied.

Our purpose is to find an approximate solution for the velocity $\boldsymbol{u}$ and the pressure p to the incompressible Navier-Stokes equations

$$\frac{\partial \boldsymbol{u}}{\partial t} + (\boldsymbol{u} \cdot \nabla)\boldsymbol{u} = -\frac{1}{\rho}\nabla p + \nu \nabla^2 \boldsymbol{u} + \boldsymbol{f}, \tag{4.1}$$

with the incompressibility condition

$$\nabla \cdot \boldsymbol{u} = 0, \tag{4.2}$$

in the domain Ω. Both the density ρ and the kinematic viscosity ν are constant. The vector $\boldsymbol{f}$ represents the body forces.

4.1 Time discretisation and splitting

We will not solve the Navier-Stokes equations directly as a coupled system, but instead split the system into simpler equations we can solve efficiently. Two different, but both commonly used, splitting schemes are implemented in the DNS code. A splitting scheme with third-order accuracy is sought, and it is important that this can be accomplished without very strict stability requirements. As is often done in incompressible flow solvers, we use an implicit method for the viscous terms and an explicit method for the convective terms.

This avoids a strict stability constraint from the viscous scheme and a costly non-linear solver for the convective scheme.

The first splitting scheme uses stiffly stable time integrators, and extrapolation to approximate the convective terms. The scheme was developed by Karniadakis et al. (1991) and it is applied to the continuous equations. When the splitting scheme is applied, we get the semi-discrete system

$$\frac{\hat{\boldsymbol{u}} - \sum_{q=0}^{J_i-1} \alpha_q \boldsymbol{u}^{n-q}}{\Delta t} = -\sum_{q=0}^{J_e-1} \beta_q \left[(\boldsymbol{u}\cdot\nabla)\,\boldsymbol{u}\right]^{n-q} + \boldsymbol{f}^{n+1}, \tag{4.3a}$$

$$\frac{\hat{\hat{\boldsymbol{u}}} - \hat{\boldsymbol{u}}}{\Delta t} = -\frac{1}{\rho}\nabla p^{n+1}, \tag{4.3b}$$

$$\frac{\gamma_0 \boldsymbol{u}^{n+1} - \hat{\hat{\boldsymbol{u}}}}{\Delta t} = \nu \nabla^2 \boldsymbol{u}^{n+1}. \tag{4.3c}$$

J_i and J_e are the orders of the implicit and explicit schemes, respectively, and α_q, β_q and γ_0 are the weights for the explicit and implicit stiffly stable schemes (Karniadakis and Sherwin, 2005, page 264). Δt is the time step. It is worth noting that the implicit stiffly stable schemes are in fact the backwards differentiation formula (BDF) schemes, while the explicit schemes are obtained using a BDF scheme combined with polynomial extrapolation.

By taking the divergence of equation (4.3b) and assuming that $\nabla \cdot \hat{\hat{\boldsymbol{u}}} = 0$ we get a Poisson equation for the pressure, i.e.

$$\nabla^2 p^{n+1} = \frac{\rho}{\Delta t}\nabla \cdot \hat{\boldsymbol{u}}. \tag{4.4}$$

By rearranging equation (4.3c) we see that it takes the form of a Helmholtz equation for each of the new velocity components

$$\left(\nabla^2 - \frac{\gamma_0}{\nu \Delta t}\right)\boldsymbol{u}^{n+1} = -\frac{1}{\nu \Delta t}(\hat{\boldsymbol{u}} - \Delta t \nabla p^{n+1}). \tag{4.5}$$

The solution method then consists of first finding $\hat{\boldsymbol{u}}$ from equation (4.3a), then solving the Poisson equation in (4.4) for the pressure and the three Helmholtz equations in (4.5) for the three velocity components.

As the explicit schemes are used to integrate the convective operator, an operator with purely imaginary eigenvalues (at least for the continuous operator), the factor that determines the stability requirements is how much of the imaginary axis is included in the stability diagram. While the stability diagram of the third-order explicit stiffly stable scheme does contain a sizeable portion of the imaginary axis, the standard fourth-order Runge-Kutta method encompasses about three times as much of the imaginary axis in the stability diagram. This means that in cases where the time step required for stability is much smaller than the time step required for a sufficiently accurate solution, significant performance gains can be accomplished by switching to a different type of time discretisation. There are no stability requirements associated with the implicit scheme applied to the viscous operator.

The second splitting scheme uses the same kind of pressure velocity splitting, but with a semi-Lagrangian convection treatment (Maday et al., 1990; Xiu and

Karniadakis, 2001; Xiu et al., 2005). This means that equations (4.4) and (4.5) are still solved for the pressure and velocity, but we get a new equation for $\hat{\boldsymbol{u}}$. Instead of using extrapolation for the convection we solve a pure convection problem to obtain $\hat{\boldsymbol{u}}$. We use the combination of a BDF scheme for the viscous Stokes operator and a Runge-Kutta scheme for the convection problem.

The velocity $\hat{\boldsymbol{u}}$ is computed as

$$\hat{\boldsymbol{u}} = \sum_{q=0}^{J_i-1} \alpha_q \tilde{\boldsymbol{u}}^{n-q} + \Delta t \boldsymbol{f}^{n+1}, \tag{4.6}$$

where $\tilde{\boldsymbol{u}}^{n-q}$ are obtained by solving the J_i convection problems

$$\frac{d\tilde{\boldsymbol{u}}}{dt} = -(\boldsymbol{U}(t)\cdot\nabla)\tilde{\boldsymbol{u}}, \;\; \tilde{\boldsymbol{u}}(t^{n-q}) = \boldsymbol{u}^{n-q}, \;\; t^{n-q} \le t \le t^{n+1}, \\ q = 0, \ldots, J_i - 1. \tag{4.7}$$

The convection velocity $\boldsymbol{U}(t)$ is the polynomial extrapolant of order $J_i - 1$ on the interval $t^{n+1-J_i} \le t \le t^{n+1}$. The convection problems must be solved with an integration method of order at least equal to J_i, in order to obtain a time accuracy of order J_i for this semi-Lagrangian method. We use the standard fourth-order Runge-Kutta method. The particular semi-Lagrangian scheme we have just presented, was described by Maday et al. (1990), and derived using operator-integration-factors.

If the time step required for stability is much smaller than the time step required for accuracy, we can integrate the convection equation using a smaller time step $\Delta t/s$. This is particularly useful if integrating the convection operator is relatively cheap compared with the solution of the Poisson and Helmholtz equations. When using s sub-steps, integration order J_i and a fourth-order Runge-Kutta method, the convection step requires a total of $2sJ_i(J_i + 1)$ convection operator evaluations, which can be very expensive for a higher order scheme. It is, however, possible to reduce the number of convection operator evaluations to $4sJ_i$ by exploiting the linearity of the convection equation (Fischer). The optimal choice of splitting scheme, time step and number of sub-steps will depend on the relative cost of evaluating the convection operator and solving the Poisson and Helmholtz equations.

The reason this type of method is called a semi-Lagrangian method, is that we discretise the Lagrangian derivative using the BDF scheme for a particle trajectory arriving at the grid-point at time t^{n+1}. This type of semi-Lagrangian method is called an auxiliary semi-Lagrangian method because we solve an auxiliary convection equation. Another type of semi-Lagrangian method, the strong semi-Lagrangian method, uses interpolation to find the departure point of the fluid particle arriving at the grid-point. We will use this type of method in chapter 5.

In both of the splitting schemes we have presented, we end up with a Poisson equation for the pressure, and Neumann pressure boundary conditions must be estimated. It is quite common, especially in standard CFD codes, to use $\boldsymbol{n}\cdot\nabla p = 0$ as the pressure boundary condition on solid surfaces. Here $\boldsymbol{n}$ is the outward surface normal vector. However, this boundary condition is only correct

in inviscid flow, and the use of this boundary condition in viscous flow will cause $\mathcal{O}(1)$ errors near the surface (Tomboulides et al., 1989; Karniadakis et al., 1991). Instead, we will use a pressure boundary condition which is consistent with and can be easily derived from the Navier-Stokes equations. The Neumann pressure boundary condition is

$$\boldsymbol{n}\cdot\nabla p = -\rho\left[\frac{\partial \boldsymbol{u}}{\partial t}^{n+1} + \nu\sum_{q=0}^{J_p-1}\beta_q(\nabla\times(\nabla\times\boldsymbol{u}))^{n-q} - \boldsymbol{f}^{n+1} + \sum_{q=0}^{J_e-1}\beta_q[(\boldsymbol{u}\cdot\nabla)\boldsymbol{u}]^{n-q}\right]\cdot\boldsymbol{n}, \quad (4.8)$$

where J_p is the order of the boundary condition approximation. On a surface with non-slip velocity boundary conditions this simplifies to

$$\boldsymbol{n}\cdot\nabla p = -\rho\left[\nu\sum_{q=0}^{J_p-1}\beta_q(\nabla\times(\nabla\times\boldsymbol{u}))^{n-q} - \boldsymbol{f}^{n+1}\right]\cdot\boldsymbol{n}, \quad (4.9)$$

which when $\boldsymbol{f}=0$ will be reduced to $\boldsymbol{n}\cdot\nabla p = 0$ in inviscid flow.

The explicit pressure boundary condition has been shown (Leriche and Labrosse, 2000) to be unconditionally stable for $J_p = 1, 2$, with only conditional stability for $J_p > 2$. This is not, however, a significant problem in practice as the time step required for accuracy is usually smaller than the stability constraint (Leriche and Labrosse, 2000).

Before we move to the next part of the discretisation, it should be pointed out that neither of the two splitting schemes presented here will find a velocity field that is exactly divergence free, because we do not project the velocity field onto the subspace of solenoidal vector functions. This means that the divergence-free condition will be part of the convergence process.

4.2 The Poisson and Helmholtz equations

Having dealt with the splitting and temporal discretisation, we end up with one Poisson equation and three Helmholtz equations that we need to solve. This closely follows the procedure developed by Rønquist (1988, 2012).

We start by writing the Poisson equation for the pressure as

$$-\nabla^2 p = f(\boldsymbol{x}) \quad \text{in } \Omega. \quad (4.10)$$

This is the strong form of the Poisson equation. The weak form, which is the form we will solve, is formulated by multiplying with a test function v and integrating over the domain Ω. Using integration by parts, we obtain

$$(\nabla v, \nabla p) = (v, f) + \int_{\partial\Omega} v(\nabla p\cdot\boldsymbol{n})\,dS\,, \quad (4.11)$$

where

$$(\nabla v, \nabla p) = \int_{\Omega}\nabla v\cdot\nabla p\,d\boldsymbol{x} \quad (4.12)$$

is the weak form of the Laplacian of p,

$$(v, f) = \int_\Omega v f \, d\boldsymbol{x} \tag{4.13}$$

is the inner product of v and f over Ω, and

$$\int_{\partial\Omega} v(\nabla p \cdot \boldsymbol{n}) \, dS \tag{4.14}$$

enforces the Neumann boundary condition for ∇p on the surface of Ω.

Next we must define the function spaces. $L^2(\Omega)$ is the space of all functions that are square-integrable over Ω. $H^1(\Omega)$ is the space of all functions, such that the function and the first derivative are square-integrable over Ω. It is clear that $H^1(\Omega) \subset L^2(\Omega)$. We require that $f \in L^2(\Omega)$ and choose the solution space as

$$X = H^1(\Omega) \tag{4.15}$$

to arrive at the weak form: find $p \in X$ such that

$$(\nabla v, \nabla p) = (v, f) + \int_{\partial\Omega} v(\nabla p \cdot \boldsymbol{n}) \, dS \,, \quad \forall v \in X. \tag{4.16}$$

Discretising equation (4.16) involves choosing a discrete solution space, a basis, a test-function and quadrature to approximate the integrals; but first we must define the domain Ω. We have so far stated that the equations are solved in the domain Ω, without giving any details about this domain. As we are using a spectral element framework, the domain consists of several smaller sub-domains or elements. The domain Ω is the union of E deformed hexahedral sub-domains Ω_e, i.e.

$$\overline{\Omega} = \bigcup_{e=1}^{E} \overline{\Omega}_e, \quad \mathcal{F}_e : \hat{\Omega} \to \Omega_e, \quad e = 1, \ldots, E, \tag{4.17}$$

where $\mathcal{F}_e$ is a geometry mapping that maps the reference domain $\hat{\Omega} = (-1, 1) \times (-1, 1) \times (-1, 1)$ to Ω_e. Associated with each geometry mapping $\mathcal{F}_e$ we have a Jacobian

$$\boldsymbol{J}^e = \begin{pmatrix} \frac{\partial x}{\partial \xi} & \frac{\partial x}{\partial \eta} & \frac{\partial x}{\partial \zeta} \\ \frac{\partial y}{\partial \xi} & \frac{\partial y}{\partial \eta} & \frac{\partial y}{\partial \zeta} \\ \frac{\partial z}{\partial \xi} & \frac{\partial z}{\partial \eta} & \frac{\partial z}{\partial \zeta} \end{pmatrix} \tag{4.18}$$

and its inverse $\boldsymbol{J}^{-1}$, which relates the reference variables (ξ, η, ζ) to the physical variables (x, y, z), and can be different at each point in space. J is defined as the determinant of $\boldsymbol{J}$,

$$J = \det(\boldsymbol{J}). \tag{4.19}$$

Derivatives are computed as

$$\frac{\partial p^e}{\partial x} = \frac{\partial \hat{p}^e}{\partial \xi}\frac{\partial \xi}{\partial x} + \frac{\partial \hat{p}^e}{\partial \eta}\frac{\partial \eta}{\partial x} + \frac{\partial \hat{p}^e}{\partial \zeta}\frac{\partial \zeta}{\partial x}, \tag{4.20a}$$

$$\frac{\partial p^e}{\partial y} = \frac{\partial \hat{p}^e}{\partial \xi}\frac{\partial \xi}{\partial y} + \frac{\partial \hat{p}^e}{\partial \eta}\frac{\partial \eta}{\partial y} + \frac{\partial \hat{p}^e}{\partial \zeta}\frac{\partial \zeta}{\partial y}, \tag{4.20b}$$

$$\frac{\partial p^e}{\partial z} = \frac{\partial \hat{p}^e}{\partial \xi}\frac{\partial \xi}{\partial z} + \frac{\partial \hat{p}^e}{\partial \eta}\frac{\partial \eta}{\partial z} + \frac{\partial \hat{p}^e}{\partial \zeta}\frac{\partial \zeta}{\partial z}, \tag{4.20c}$$

where $\hat{p}^e = p|_{\Omega_e} \circ \mathcal{F}_e$ is the reference solution on the reference domain.

To discretise equation (4.16), we define the discrete solution space $X_{E,N}$ as

$$X_{E,N} = \{v \in X \quad | \quad v|_{\Omega_e} \circ \mathcal{F}_e \in \mathbb{P}_N(\hat{\Omega})\}, \tag{4.21}$$

where $\mathbb{P}_N(\hat{\Omega})$ is the space of all polynomial functions of degree $\leq N$ over the reference domain $\hat{\Omega}$.

Next we define a basis for the discrete space as

$$\forall v \in X_{E,N}, \quad v|_{\Omega_e} \circ \mathcal{F}_e = \hat{v}^e,$$
$$\hat{v}^e(\xi,\eta,\zeta) = \sum_{\alpha=0}^{N}\sum_{\beta=0}^{N}\sum_{\gamma=0}^{N} v^e_{\alpha\beta\gamma} l_\alpha(\xi) l_\beta(\eta) l_\gamma(\zeta). \tag{4.22}$$

This defines a nodal tensor-product basis in each element, where $l_\alpha(\xi)$ is the one-dimensional N-order Lagrangian interpolant through the nodes and $v^e_{\alpha\beta\gamma}$ denote the nodal values. When using high-order polynomial interpolation, the nodes need to be chosen carefully to guarantee convergence, as using equidistant points will lead to severe oscillations (Runge's phenomenon). We use the $N+1$ Gauss-Lobatto-Legendre (GLL) nodes. Similarly, the solution can be expressed as

$$p|_{\Omega_e} \circ \mathcal{F}_e = \hat{p}^e_N, \quad \hat{p}^e_N(\xi,\eta,\zeta) = \sum_{\alpha=0}^{N}\sum_{\beta=0}^{N}\sum_{\gamma=0}^{N} p^e_{\alpha\beta\gamma} l_\alpha(\xi) l_\beta(\eta) l_\gamma(\zeta). \tag{4.23}$$

C^0 continuity is enforced across element boundaries.

The geometry is approximated using the same basis as the solution,

$$x^e_N(\xi,\eta,\zeta) = \sum_{\alpha=0}^{N}\sum_{\beta=0}^{N}\sum_{\gamma=0}^{N} x^e_{\alpha\beta\gamma} l_\alpha(\xi) l_\beta(\eta) l_\gamma(\zeta), \tag{4.24}$$

and similarly for y and z.

What remains is the choice of test functions and quadrature. As test functions we choose

$$\hat{v}(\xi,\eta,\zeta) = l_i(\xi) l_j(\eta) l_k(\zeta), \quad \forall i,j,k = 0,\ldots,N, \tag{4.25}$$

and we use GLL-quadrature,

$$\int_{\Omega_e} g \, d\boldsymbol{x} \approx \sum_{\alpha=0}^{N}\sum_{\beta=0}^{N}\sum_{\gamma=0}^{N} \rho_\alpha \rho_\beta \rho_\gamma g_{\alpha\beta\gamma} J_{\alpha\beta\gamma} \tag{4.26}$$

to approximate the integrals in the weak form.

Putting all this together, yields a system of linear equations

$$\boldsymbol{A}\boldsymbol{p} = \boldsymbol{b}, \tag{4.27}$$

for all the nodal pressure values p^e_{ijk}. Due to the exclusive use of Neumann boundary conditions, this system is actually singular, and the matrix $\boldsymbol{A}$ has a non-trivial null-space consisting of the one-vector $\mathbf{1}$. This is, however, the only spurious pressure mode we have to deal with for the particular splitting schemes we are using. How we deal with the null-space of $\boldsymbol{A}$ when we solve the system, is discussed in chapter 4.4.

Having taken care of the Poisson equation for the pressure, three Helmholtz equations for the three velocity components remain. The Helmholtz equation is in its strong form written as

$$\nabla^2 u + cu = f(\boldsymbol{x}) \quad \text{in } \Omega, \tag{4.28}$$

where c is a constant. Again we seek the weak form, but this time we are using Dirichlet boundary conditions on $\partial\Omega$. The solution space Y is then defined as

$$Y = H^1_0 = \{v \in H^1 \quad | \quad v|_{\partial\Omega} = 0\}, \tag{4.29}$$

which means that homogeneous Dirichlet boundary conditions are defined in the function space. Non-homogeneous Dirichlet boundary conditions are obtained by lifting the solution, which means expressing u as $u_0 + u_D$, where u_0 satisfies homogeneous Dirichlet boundary conditions and u_D is a function in H^1 which satisfies the real non-homogeneous boundary conditions. The resulting weak form of the Helmholtz equation is: find $u \in Y$ such that

$$(\nabla w, \nabla u_0) + c\,(w, u_0) = (w, f) - (\nabla w, \nabla u_D) - c\,(w, u_D)\,, \quad \forall w \in Y. \tag{4.30}$$

The discretisation of equation (4.30) is almost identical to the discretisation of equation (4.16), with the exception that the nodes on $\partial\Omega$ are set equal to zero, and therefore that the resulting system

$$\boldsymbol{B}\boldsymbol{u} = \boldsymbol{d}, \tag{4.31}$$

for the nodal values u^e_{ijk}, is non-singular.

4.3 Convection operator, aliasing and spectral vanishing viscosity

Whichever splitting scheme we choose to use, we have to approximate the convection terms in the Navier-Stokes equations. The convection operator $(\boldsymbol{u} \cdot \nabla)\boldsymbol{u}$ can be written in several different forms: the conservative form

$$\nabla \cdot \boldsymbol{u}\boldsymbol{u}, \tag{4.32}$$

the convective form

$$\boldsymbol{u} \cdot \nabla \boldsymbol{u}, \tag{4.33}$$

the skew-symmetric form

$$\frac{1}{2}(\nabla \cdot \boldsymbol{u}\boldsymbol{u} + \boldsymbol{u} \cdot \nabla \boldsymbol{u}), \tag{4.34}$$

and the rotational form

$$\frac{1}{2}\nabla \cdot \boldsymbol{u}\boldsymbol{u} - \boldsymbol{u} \times (\nabla \times \boldsymbol{u}). \tag{4.35}$$

These continuous operators are all equivalent in incompressible flow, but the discrete operators will be different. The choice of convection operator can have a significant impact on the solution (Rønquist, 1996; Wilhelm and Kleiser, 2000), and only the skew-symmetric form has purely imaginary eigenvalues (Rønquist, 1996). The computational cost of the convective forms will also differ in the number of matrix-matrix products needed. Benchmark tests of three of the different convection operators are shown in chapter 6.

We discretise the weak form of the convective operator

$$(\boldsymbol{v}, (\boldsymbol{w} \cdot \nabla)\boldsymbol{u}), \tag{4.36}$$

where $\boldsymbol{v}$ is the test function and $\boldsymbol{w}$ is the convective velocity. When the convective terms are linearised, as in the semi-Lagrangian splitting scheme, the convective velocity $\boldsymbol{w}$ is not equal to $\boldsymbol{u}$. No integration by parts is performed on the convection terms.

A polynomial approximation of the non-linear convection operator, will cause aliasing errors, in much the same way as for Fourier spectral approximations. In both Fourier and polynomial spectral approximations, over-integration (super-collocation) can be used to avoid aliasing. We use numerical quadrature of a higher order than the polynomial approximation used for the solution, and this requires interpolation. In under-resolved simulations, the aliasing errors can cause stability problems and must be dealt with in some way. Using $3N/2$ quadrature points to approximate the convective terms, effectively removes the problem of aliasing and stabilises the simulation (Kirby and Karniadakis, 2003).

Another way to stabilise an unstable simulation is to use spectral vanishing viscosity (SVV) (Kirby and Karniadakis, 2002). Spectral vanishing viscosity involves adding a small portion of added viscosity only to the highest wave-numbers. This dampens unphysical high-wavenumber oscillations, without compromising the exponential convergence of the spectral element approximation. We use the formulation presented by Xu and Pasquetti (2004), which yields an exponentially accurate stabilised solution with no change to computational cost per iteration of the iterative solver.

4.4 Solving symmetric positive definite systems

For each time step we have to solve four symmetric positive definite (SPD) systems. We will discuss how such systems are solved, exemplified with the system

$$\boldsymbol{A}\boldsymbol{x} = \boldsymbol{b}. \tag{4.37}$$

The standard method of choice for SPD systems is the preconditioned conjugate gradient (PCG) method (Hestenes and Stiefel, 1952), which is shown in algorithm 1 for an error tolerance ε.

Algorithm 1 Preconditioned conjugate gradient method

function conjugate_gradient($\boldsymbol{x}_0, \boldsymbol{b}, \varepsilon$)
  $\boldsymbol{r}_0 \leftarrow \boldsymbol{b} - \boldsymbol{A}\boldsymbol{x}_0$
  $\boldsymbol{z}_0 \leftarrow \boldsymbol{P}^{-1}\boldsymbol{r}_0$
  $\boldsymbol{p}_0 \leftarrow \boldsymbol{z}_0$
  $k \leftarrow 0$
  while $\boldsymbol{r}_k^T \boldsymbol{r}_k > \varepsilon^2$ **do**
    $\alpha_k \leftarrow \frac{\boldsymbol{r}_k^T \boldsymbol{z}_k}{\boldsymbol{p}_k^T \boldsymbol{A}\boldsymbol{p}_k}$
    $\boldsymbol{x}_{k+1} \leftarrow \boldsymbol{x}_k + \alpha_k \boldsymbol{p}_k$
    $\boldsymbol{r}_{k+1} \leftarrow \boldsymbol{r}_k - \alpha_k \boldsymbol{A}\boldsymbol{p}_k$
    $\boldsymbol{z}_{k+1} \leftarrow \boldsymbol{P}^{-1}\boldsymbol{r}_{k+1}$
    $\beta_k \leftarrow \frac{\boldsymbol{z}_{k+1}^T \boldsymbol{r}_{k+1}}{\boldsymbol{z}_k^T \boldsymbol{r}_k}$
    $\boldsymbol{p}_{k+1} \leftarrow \boldsymbol{z}_{k+1} + \beta_k \boldsymbol{p}_k$
    $k \leftarrow k + 1$
  return $\boldsymbol{x}_{k+1}$

Multiplication with the symmetric positive definite preconditioner matrix $\boldsymbol{P}^{-1}$, accelerates the solver by reducing the condition number of the system. For large systems, an efficient preconditioner is needed to be able to solve the system in a reasonable number of iterations. Sometimes it is necessary to use a sophisticated preconditioner, that is not necessarily constant between iterations. This violates the assumptions behind the preconditioned conjugate gradient method, and might seriously compromise the performance of the algorithm. In such cases, it is better to use a different formulation of the method, the flexible conjugate gradient method (Notay, 2000), which allows the use of a variable preconditioner. Algorithm 2 shows the solution procedure for the flexible conjugate gradient method. In this algorithm, multiplication by $\boldsymbol{P}^{-1}$ should be thought of as a general operator which approximates the action of $\boldsymbol{A}^{-1}$, and not as a standard matrix-vector multiplication.

Algorithm 2 Flexible preconditioned conjugate gradient method

function flexible_conjugate_gradient($\boldsymbol{x}_0, \boldsymbol{b}, \varepsilon$)
  $\boldsymbol{r}_0 \leftarrow \boldsymbol{b} - \boldsymbol{A}\boldsymbol{x}_0$
  $k \leftarrow 0$
  while $\boldsymbol{r}_k^T \boldsymbol{r}_k > \varepsilon^2$ **do**
    $\boldsymbol{z}_k \leftarrow \boldsymbol{P}^{-1}\boldsymbol{r}_k$
    $\boldsymbol{p}_k \leftarrow \boldsymbol{z}_k - \sum_{j=k-m_k}^{k-1} \frac{\boldsymbol{z}_k^T \boldsymbol{A}\boldsymbol{p}_j}{\boldsymbol{p}_j^T \boldsymbol{A}\boldsymbol{p}_j} \boldsymbol{p}_j$
    $\boldsymbol{x}_{k+1} \leftarrow \boldsymbol{x}_k + \frac{\boldsymbol{p}_k^T \boldsymbol{r}_k}{\boldsymbol{p}_k^T \boldsymbol{A}\boldsymbol{p}_k} \boldsymbol{p}_k$
    $\boldsymbol{r}_{k+1} \leftarrow \boldsymbol{r}_k - \frac{\boldsymbol{p}_k^T \boldsymbol{r}_k}{\boldsymbol{p}_k^T \boldsymbol{A}\boldsymbol{p}_k} \boldsymbol{A}\boldsymbol{p}_k$
    $k \leftarrow k + 1$
  return $\boldsymbol{x}_{k+1}$
$m_0 = 0; \;\; m_k = \max(1, \;\; \mathrm{mod}\;(k, m_{\max} + 1)), \;\; k > 0$

When solving the Poisson equation with Neumann boundary conditions, we have to take special steps to address the null-space. The null-space of the Poisson system matrix $\boldsymbol{A}$ consists of the all-ones vector $\mathbf{1}$, and to make sure that the conjugate gradient method converges, we first project out the portion of the right-hand-side vector $\boldsymbol{b}$ that lies in the null-space. Before line 2 in algorithm 1 or 2 we perform the projection

$$\boldsymbol{b} \leftarrow \boldsymbol{b} - \frac{\boldsymbol{b}^T\mathbf{1}}{\mathbf{1}^T\mathbf{1}}\mathbf{1}. \tag{4.38}$$

We also have to include the projection

$$\boldsymbol{z}_k \leftarrow \boldsymbol{z}_k - \frac{\boldsymbol{z}_k^T\mathbf{1}}{\mathbf{1}^T\mathbf{1}}\mathbf{1} \tag{4.39}$$

after each application of the preconditioner $\boldsymbol{P}^{-1}$ (after line 3 and 10 in algorithm 1 and line 5 in algorithm 2), as the preconditioning might add a component in the null-space. With these minor modifications, we are able to find a solution also to the singular Poisson system. A different, and perhaps more common, method of dealing with the null-space, is to set a reference pressure at some point in the domain. This is not generally an advisable approach because it involves changing the system matrix $\boldsymbol{A}$, changing the condition number of $\boldsymbol{A}$ and possibly slowing down the convergence of the iterative method.

The systems we solve will typically be very large, and the conjugate gradient method will take many iterations to converge. It is important to use any method available to accelerate the convergence. Both the choice of initial guess $\boldsymbol{x}_0$ and the choice of preconditioner $\boldsymbol{P}^{-1}$, can dramatically affect the convergence of the iterative method, so we will consider both.

One of the simplest choices for the initial guess $\boldsymbol{x}_0$, is to use the solution from the previous time step. Compared with using $\boldsymbol{x}_0 = \mathbf{0}$, this is a considerable improvement. We can do even better than this by using polynomial extrapolation of the J_i previous solutions, which we have to store anyway for the time discretisation scheme. Grindberg and Karniadakis (2011) showed that the use of polynomial extrapolation as the initial guess, is a very effective way of reducing the number of iterations required for convergence. The computational cost of the extrapolation is marginal, and we have adopted this method for both the pressure and the velocity.

The choice of preconditioner is more complicated. For the Helmholtz velocity equations, a diagonal (Jacobi) preconditioner can be used. In turbulent flows, where $\nu\Delta t$ is a very small number, the Helmholtz operator is close to diagonal and the simple diagonal preconditioner can be used with great effect. A diagonal preconditoner is not particularly efficient for the Poisson equation, although it will help somewhat in highly deformed elements.

We use, instead, a multi-grid preconditioner for the Poisson equation. Details of the implementation of a multi-grid based solver, in combination with a spectral element discretisation, were discussed by Rønquist and Patera (1987) and Rønquist (1988). We use one multi-grid V-cycle as a preconditioner. The multi-grid V-cycle is explained in algorithm 3.

Algorithm 3 Multi-grid V-cycle

```
1:  function multi_grid(x_0, b, l, m_1, m_2)
2:      if l = 1 then
3:          return A^{-1} b
4:      else
5:          r = b − A x_0
6:          for k = 0, ..., m_1 − 1 do
7:              x_{k+1} = S(x_k, r)
8:          r = b − A x_{k+1}
9:          z = multi_grid(0, R r_{k+1}, l − 1, m_1, m_2)
10:         x_0 = x_{k+1} + R^T z
11:         r = b − A x_0
12:         for k = 0, ..., m_2 − 1 do
13:             x_{k+1} = S(x_k, r)
14:         return x_{k+1}
```

In algorithm 3, $\boldsymbol{R}$ is the restriction operator that takes a residual on level l and restricts it to the lower order space used on level $l-1$. The prolongation operator $\boldsymbol{R}^T$ takes a vector and extends it to the higher order space on the higher level. The smoother $\mathcal{S}(\boldsymbol{x}_k, \boldsymbol{r}), k = 0, \ldots, m-1$ smooths $\boldsymbol{x}_k$ by finding an approximate solution to the system $\boldsymbol{A}\boldsymbol{x} = \boldsymbol{r}$, using m iterations of an iterative method. In most cases, $m_1 = m_2$ is used.

Rønquist and Patera (1987) used Jacobi iteration as a smoother, while Rønquist (1988) showed that significant acceleration was possible with Chebyshev iteration. We use a diagonally preconditioned conjugate gradient solver as the smoother, with $m_1 = 0$ and $m_2 > 0$, as suggested by Canuto et al. (1998).

4.5 Particle tracking

The equation of motion for a small spherical particle, with position $\boldsymbol{X}$ and velocity $\boldsymbol{V}$, is discussed in chapter 7, while the numerical methods used to integrate the equation are described here. Integrating the equation of motion, involves two types of numerical approximations: first we must approximate the fluid velocity or any function of the fluid velocity at the particle point using interpolation, then we have to integrate the differential equations using numerical integration. The specific form of the particle equation is not important at this point, but will be discussed in chapter 7. Particle tracking of fluid particles was discussed by Darmofal and Haimes (1996) and Coppola et al. (2001), and the tracking of inertial point-particles involves many of the same challenges.

We use Lagrangian interpolation of order $P < N$, to approximate the fluid velocity at point $\boldsymbol{X}$. P should typically not exceed ~ 5 to limit the computational cost and avoid oscillations associated with Runge's phenomenon. It is possible to use the high-order spectral element polynomial basis to interpolate the velocity field, but this is prohibitively expensive for large values

of N, when there are many particles.

Having dealt with the interpolation, we are left with the problem of integrating a system of six ordinary differential equations, $\dot{\boldsymbol{y}} = \boldsymbol{f}(\boldsymbol{y}, t)$. We use the fourth order Runge-Kutta method and the time step $\Delta\tau$. Because the fourth order Runge-Kutta method requires the evaluation of the fluid velocity at times τ, $\tau + \Delta\tau/2$ and $\tau + \Delta\tau$, we use the time step $\Delta\tau = 2\Delta t$ to avoid temporal integration of the velocity field (except when the particle crosses a boundary). Particle tracking in a spectral element solver has some unique challenges (Coppola et al., 2001) associated with particles crossing element boundaries. There are two main approaches to this. Either we integrate the particle paths in the physical variables $\boldsymbol{x}$, or we integrate the particle paths in the reference variables $\boldsymbol{\xi}$. In a general deformed element, each method has its unique challenges.

Integration in the physical variables requires the solution of a non-linear problem to find the fluid velocity in the particle coordinate. Because we know the physical coordinates of the particle, but not the reference coordinates, we first have to find which element houses the particle and secondly use iteration to find the particle reference coordinates, to be able to integrate the velocity field.

Algorithm 4 Integrate particle to element boundary

procedure integrate_to_boundary($\boldsymbol{y}, t$)
  $\boldsymbol{f}_1 \leftarrow \boldsymbol{f}(\boldsymbol{y}, t)$
  $h \leftarrow$ time_to_boundary($\boldsymbol{y}, \boldsymbol{f}_1$)
  for $k = 1, \ldots, m$ **do**
    $\boldsymbol{f}_2 \leftarrow \boldsymbol{f}(\boldsymbol{y} + \frac{h}{2}\boldsymbol{f}_1, t + \frac{h}{2})$
    $h \leftarrow$ time_to_boundary($\boldsymbol{y}, \boldsymbol{f}_2$)
    $\boldsymbol{f}_3 \leftarrow \boldsymbol{f}(\boldsymbol{y} + \frac{h}{2}\boldsymbol{f}_2, t + \frac{h}{2})$
    $h \leftarrow$ time_to_boundary($\boldsymbol{y}, \boldsymbol{f}_3$)
    $\boldsymbol{f}_4 \leftarrow \boldsymbol{f}(\boldsymbol{y} + h\boldsymbol{f}_2, t + h)$
    $\boldsymbol{f}_5 \leftarrow \frac{1}{6}(\boldsymbol{f}_1 + 2\boldsymbol{f}_2 + 2\boldsymbol{f}_3 + \boldsymbol{f}_4)$
    $h \leftarrow$ time_to_boundary($\boldsymbol{y}, \boldsymbol{f}_5$)
  $t \leftarrow t + h$
  $\boldsymbol{y} \leftarrow \boldsymbol{y} + h\boldsymbol{f}_5$

We use integration in the reference coordinates. In spectral element simulations, where a particle crossing an element boundary is a relatively rare occurrence, this is the more efficient method. First we have to express the system in terms of the reference velocities using the chain rule, e.g.

$$\frac{d\xi}{dt} = \frac{\partial \xi}{\partial x}\frac{dx}{dt} + \frac{\partial \xi}{\partial y}\frac{dy}{dt} + \frac{\partial \xi}{\partial z}\frac{dz}{dt}, \tag{4.40}$$

which takes care of the problem of integrating the particle inside an element. When a particle crosses a boundary, we first have to integrate the particle to the boundary using a time step $\delta\tau < \Delta\tau$, then we transform the particle velocity to physical coordinates, find the particle reference coordinates in the new element

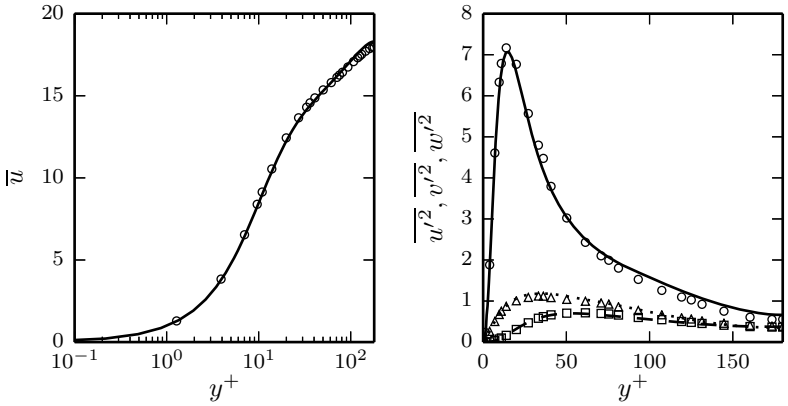

Figure 4.1: Mean streamwise fluid velocity $\overline{u}$ (left, circles) compared with reference simulation (solid line) (Moser et al., 1999), and normal Reynolds stress tensor components (right) in streamwise (circles), wall-normal (squares) and spanwise (triangles) direction, compared with reference simulation (solid, dashed and dotted lines).

and find the new reference velocity. The remaining part of the time step, $\Delta\tau - \delta\tau$, is integrated in the new element.

Finding the time step $\delta\tau$ that brings the particle exactly to the element boundary, is in general a non-linear problem. We solve this using a very simple modified Runge-Kutta method shown in algorithm 4, by updating a linear estimate of $\delta\tau$ between each Runge-Kutta sub-step.

4.6 Simulations of turbulent flow

Direct numerical simulations of turbulent flow are almost always under-resolved, and in many cases vastly so, compared to the resolution used in typical convergence tests. The convergence properties of the numerical methods are therefore not the only important factor, it is just as important how the methods perform when the resolution is very low.

In figure 4.1 we show the results of a low resolution ($40 \times 51 \times 40$) simulation of a turbulent channel flow at friction Reynolds number 180, compared with a well-resolved ($128 \times 129 \times 128$) reference simulation (Moser et al., 1999). Our results agree well with the reference simulation, despite the low resolution. The simulation would be unstable without spectral vanishing viscosity, and because of the low resolution, one might choose to call this a large eddy simulation. Nevertheless, it shows that it is possible to obtain accurate results with very low spatial resolution, which emphasises the robustness of the chosen methodology.

4.7 Implementation

The simulation methodology described in the preceding sections has been implemented in a direct numerical simulation code, written in the C programming language (Kernighan and Ritchie, 1988). Due to the computational complexity of direct numerical simulations, implementation and programming efficiency is important. We use the BLAS library (Lawson et al., 1979) for all vector and matrix operations.

The convection and Laplace operators, are the most computationally demanding parts of the Navier-Stokes solver. These require the evaluation of derivatives. The derivatives of the nodal values u_{ijk} $(n \times n \times n)$ inside an element, are evaluated by multiplying the unrolled n^3 vector $\boldsymbol{u}$ with one of the three differentiation matrices

$$\boldsymbol{D}_x = (\boldsymbol{I} \otimes \boldsymbol{I} \otimes \hat{\boldsymbol{D}}), \quad \boldsymbol{D}_y = (\boldsymbol{I} \otimes \hat{\boldsymbol{D}} \otimes \boldsymbol{I}), \quad \boldsymbol{D}_z = (\hat{\boldsymbol{D}} \otimes \boldsymbol{I} \otimes \boldsymbol{I}). \tag{4.41}$$

$\hat{\boldsymbol{D}}$ is the one-dimensional Lagrangian differentiation matrix, with

$$\hat{D}_{ij} = l'_j(\xi_i). \tag{4.42}$$

By exploiting the memory layout of $\boldsymbol{u}$, these matrix-vector multiplications can be evaluated as matrix-matrix multiplications (Deville et al., 2002, chapter 8) of complexity $\mathcal{O}(n^4)$, between the $n \times n$ matrix $\hat{\boldsymbol{D}}$ and $\boldsymbol{u}$ treated as either an $n \times n^2$ matrix, n $n \times n$ matrices or an $n^2 \times n$ matrix. All geometry transformation operations are evaluated in $\mathcal{O}(n^3)$ and thus do not change the $\mathcal{O}(n^4)$ leading order complexity.

We have so far almost exclusively discussed operators that are local to each element. In order to ensure C^0 continuity on element boundaries, we use the global operation known as direct stiffness summation. The direct stiffness summation operator Σ' takes the shared interface variables, adds them together, and redistributes them to the original locations.

Efficient parallelisation of the code is essential, to be able to simulate turbulent flow. We use domain decomposition and distribute the different elements on different processors. The communication between them is handled using the Message Passing Interface (MPI). There are only two operators in the solver that require communication between the elements, direct stiffness summation and the global dot product. Direct stiffness summation is implemented using one `MPI_Alltoallv`, while the global dot product is implemented using `MPI_Allreduce`.

Parallelisation of the particle solver is a different challenge. The particle integration itself is "embarrassingly parallel" because there is no interaction between the particles. However, information about the local fluid velocity is required but not necessarily easily available. There are two ways of solving this: either the particles have to be moved from one processor to the next when the particles cross element boundaries, or information about the fluid velocity has to be sent to the processor where the particle is located. We have chosen the first approach, because the second is extremely inefficient due to the large communication cost each time step. The methodology described in section 4.5 is easily parallelised by sending the particle to the correct processor, when the particle crosses over to the next element.

Chapter 5

Synthetic turbulence

The idea behind synthetic turbulence, is to generate a velocity field which resembles real turbulence, without actually solving the Navier-Stokes equations. We will only consider synthetic incompressible homogeneous isotropic turbulence. There are several different ways of generating a synthetic velocity field, but it usually involves a random number generator in some way. Simulations of synthetic turbulence are often referred to as kinetic simulations (Fung et al., 1992; Thomson and Devenish, 2005; Osborne et al., 2006).

In order to make random noise look like turbulence, we choose some conditions the velocity field must satisfy. These are: incompressibility, a turbulence-like energy spectrum, a turbulence-like time evolution and smoothness at the smallest scales. Within these constraints, there are a wide range of possible velocity fields with very different statistical properties. We consider two different types of synthetic turbulence, one Gaussian and one non-Gaussian.

5.1 Gaussian synthetic turbulence

The energy spectrum $E(k)$ is an integral part of the synthetic turbulence methodology. A synthetic velocity field $\boldsymbol{u}(\boldsymbol{x}, t)$, is generated on a periodic box with uniform grid and n grid points in each direction. The velocity has the Fourier transform $\hat{\boldsymbol{u}}(\boldsymbol{k})$, and we compute the energy of $\hat{\boldsymbol{u}}$, with complex conjugate $\hat{\boldsymbol{u}}^*$, at wavenumber $k = |\boldsymbol{k}|$ as

$$\mathcal{E}(\hat{\boldsymbol{u}}; k) = \sum_{|\boldsymbol{p}|=k} \hat{\boldsymbol{u}}(\boldsymbol{p}) \cdot \hat{\boldsymbol{u}}^*(\boldsymbol{p}). \tag{5.1}$$

We use the energy spectrum

$$E(k) = C\epsilon^{2/3} k^{-5/3} \exp(-C_\eta(\eta k)^2), \tag{5.2}$$

where ϵ is the rate of dissipation, η is the Kolmogorov length scale, and C and C_η are constants. Using an energy spectrum without an energy containing range at the lowest wavenumbers, and an $\exp(-k^2)$ roll-off at the highest wavenumbers, extends the $k^{-5/3}$ scaling over a wider range of wavenumbers.

Producing a Gaussian synthetic turbulence field starts by generating a three-dimensional vector field of random Fourier modes $\hat{\boldsymbol{\zeta}}$. The Fourier modes are generated such that the real and imaginary parts of $\hat{\boldsymbol{\zeta}}$ follow a standard normal distribution,

$$(\Re(\hat{\boldsymbol{\zeta}}), \Im(\hat{\boldsymbol{\zeta}})) \sim \mathcal{N}(\mathbf{0}, \mathbf{1}). \tag{5.3}$$

In order to ensure that the inverse Fourier transform of $\hat{\boldsymbol{\zeta}}$ is real, the necessary conjugate symmetry is set as part of the random mode generation.

This gives us a random velocity field, but not one resembling turbulence. The next step is to make the velocity field divergence free by the projection

$$\hat{\boldsymbol{\xi}} = \hat{\boldsymbol{\zeta}} - \frac{\boldsymbol{k} \cdot \hat{\boldsymbol{\zeta}}}{\boldsymbol{k} \cdot \boldsymbol{k}} \boldsymbol{k}, \tag{5.4}$$

and enforce the desired energy spectrum by applying the correction

$$\hat{\boldsymbol{u}} = \hat{\boldsymbol{\xi}} \left(\frac{E(k)}{\mathcal{E}(\hat{\boldsymbol{\xi}}; k)} \right)^{1/2}. \tag{5.5}$$

The result is the Fourier transform of a Gaussian synthetic turbulence field. Transforming this to real space by using the inverse Fourier transform $\mathcal{F}^{-1}$,

$$\boldsymbol{u} = \mathcal{F}^{-1}(\hat{\boldsymbol{u}}), \tag{5.6}$$

gives the Gaussian synthetic turbulence field.

If we wanted to use this as an initial condition for a simulation, or in any other application where the time evolution was unimportant, this would conclude the process. Because we are interested in how the velocity field evolves in time, we also need to give the velocity field a turbulence-like time dependence. This can be done most easily by using the phase shift

$$\hat{\boldsymbol{u}}(\boldsymbol{k}, t + \Delta t) = \hat{\boldsymbol{u}}(\boldsymbol{k}, t) \exp(\mathrm{i}\omega(k)\Delta t), \tag{5.7}$$

which evolves the Fourier modes a time Δt with the velocity $\omega(k)$. The phase shift preserves the energy spectrum and the incompressibility of the velocity field.

The time scales associated with large-scale sweeping of smaller scales are Uk (Tennekes, 1975), where U is some large-scale sweeping velocity. There is no such sweeping in the phase-shift mechanism that evolves the velocity field, but it is reasonable to assume that a time scale similar to what is found in real turbulence, will produce the most realistic results. We therefore use

$$\omega(k) = C_\omega U k, \tag{5.8}$$

where C_ω is a constant.

5.2 Non-Gaussian synthetic turbulence

While the simplicity of the Gaussian synthetic turbulence generation is attractive, and the resulting velocity field shares many features with real

isotropic turbulence, it is possible to create a more realistic velocity field by taking the method a bit further. It is well established that many aspects of turbulence are non-Gaussian, and it is possible to generate synthetic turbulence that is more realistic than the Gaussian velocity field. Rosales and Meneveau (2006, 2008) created a multi-scale Lagrangian map that they used to deform a Gaussian velocity field, creating a non-Gaussian synthetic velocity field. This approach was shown to be successful in generating initial conditions for turbulence simulations, but the method is not easily extended to include time evolution. The idea of using the velocity field to deform itself is something we will use, however in a way which is simpler and arguably more physical.

We start with the Navier-Stokes equations. In chapter 4 we discussed the solution of the incompressible Navier-Stokes equations, and how we can use a splitting scheme to decouple the equations. An auxiliary semi-Lagrangian splitting scheme was presented in chapter 4.1. In a strong semi-Lagrangian scheme, we use interpolation to find the fluid-particle departure points, instead of integrating a convection equation. The strong semi-Lagrangian splitting scheme is unconditionally stable.

A first-order strong semi-Lagrangian method starts with the convection step

$$\boldsymbol{v} = \boldsymbol{u}(\boldsymbol{x}_d, t), \tag{5.9a}$$

$$\boldsymbol{x}_d = \boldsymbol{x} - \Delta t \boldsymbol{u}\left(\boldsymbol{x} - \frac{\Delta t}{2}\boldsymbol{u}(\boldsymbol{x}, t), t\right), \tag{5.9b}$$

where $\boldsymbol{x}_d$ is the departure point of the fluid particle arriving at $\boldsymbol{x}$ at time $t + \Delta t$. This requires interpolation, and we use polynomial interpolation of order P. The second step is the correction for incompressibility, which involves solving a Poisson equation for the pressure,

$$\boldsymbol{w} = \boldsymbol{v} - \frac{\Delta t}{\rho}\nabla p(t + \Delta t). \tag{5.10}$$

The final step is the viscous correction, which gives the three Helmholtz equations for the velocity components,

$$\boldsymbol{u}(t + \Delta t) = \boldsymbol{w} + \nu \Delta t \nabla^2 \boldsymbol{u}(t + \Delta t). \tag{5.11}$$

We design a synthetic turbulence method based on the semi-Lagrangian splitting scheme, by retaining convection, the mechanism responsible for creating non-Gaussian statistics. While doing so, we want to get rid of the four elliptic equations in the splitting scheme. The first part of the synthetic turbulence algorithm is the convection, which remains unchanged from the splitting scheme,

$$\boldsymbol{v} = \boldsymbol{u}(\boldsymbol{x}_d, t), \tag{5.12a}$$

$$\boldsymbol{x}_d = \boldsymbol{x} - \Delta t \boldsymbol{u}\left(\boldsymbol{x} - \frac{\Delta t}{2}\boldsymbol{u}(\boldsymbol{x}, t), t\right). \tag{5.12b}$$

Because the rest of the algorithm takes place in Fourier space, we then have to transform the temporary velocity field $\boldsymbol{v}$,

$$\hat{\boldsymbol{v}} = \mathcal{F}(\boldsymbol{v}). \tag{5.13}$$

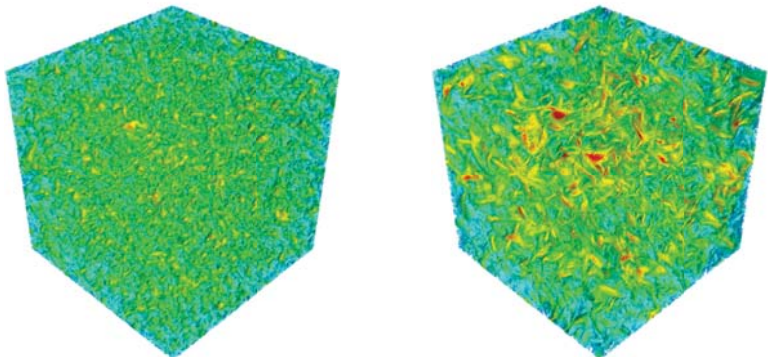

Figure 5.1: Isosurfaces of the vorticity magnitude $|\boldsymbol{\omega}|$ in Gaussian (left) and non-Gaussian (right) synthetic turbulence. The colour red indicates regions of high vorticity, and blue low vorticity.

Incompressibility can then be enforced by using the projection

$$\hat{\boldsymbol{w}} = \hat{\boldsymbol{v}} - \frac{\boldsymbol{k} \cdot \hat{\boldsymbol{v}}}{\boldsymbol{k} \cdot \boldsymbol{k}} \boldsymbol{k}, \tag{5.14}$$

which gives an incompressible velocity field without having to solve an elliptic equation. The last step, the viscous correction, is where we deviate from the Navier-Stokes equations. Instead of solving the Helmholtz equations, we simply correct the energy spectrum of the velocity field using

$$\hat{\boldsymbol{u}}(t + \Delta t) = \hat{\boldsymbol{w}} \left(\frac{E(k)}{\mathcal{E}(\hat{\boldsymbol{w}}; k)} \right)^{1/2}, \tag{5.15}$$

which is then transformed to real space to arrive at $\boldsymbol{u}(t + \Delta t)$.

We have then integrated the synthetic turbulence a time Δt using a combination of real convection and an artificial viscous correction. The idea here is that the mechanism causing dissipation is not that important, as long as there is sufficient dissipation to ensure that the energy spectrum is correct. The energy spectrum is the same as the one used for the Gaussian synthetic turbulence and the simulation can be initialised from a Gaussian synthetic turbulence field.

Figure 5.1 shows, with results from chapter 10, a comparison between the Gaussian and non-Gaussian turbulence methods presented in this chapter. While there is very little structure in the Gaussian turbulence, in the non-Gaussian turbulence we see regions of vorticity concentration and elongated vortex structures. The differences are even more striking when watching the turbulence in motion. In the non-Gaussian turbulence, vortices are convected and deformed by the flow, as in real turbulence, while the vortices in the Gaussian turbulence simply appear and disappear. The non-Gaussian algorithm is able to generate very realistic turbulence, without having to solve any elliptic equations. A more detailed comparison between the two types of synthetic turbulence is found in chapter 10.

Chapter 6

Article 2: A new spectral element direct numerical simulation code

Published in ***MekIT'13 Seventh National Conference on Computational Mechanics, Trondheim 13–14 May 2013***

A new spectral element direct numerical simulation code

Christopher Nilsen and Helge I. Andersson
Department of Energy and Process Engineering
The Norwegian University of Science and Technology, N-7491 Trondheim, Norway
e-mail: christopher.nilsen@ntnu.no

Summary A newly developed simulation code, to be used for direct numerical simulations of turbulent flow, has been tested. The code is based on the spectral element method. Comparisons with an exact solution for a three-dimensional transient vortex flow confirm third-order algebraic convergence in time, and exponential convergence in space. Tests at Reynolds numbers up to 1000 reveal that the choice of discrete advection operator, between convective, conservative and skew-symmetric, has important implications for the accuracy of the results.

Introduction

Direct numerical simulations (DNS) have been frequently used in turbulence research [7] ever since Orszag and Patterson [8] first showed that a numerical simulation could give accurate predictions of wind-tunnel turbulence. It is crucial for the credibility of such simulation results that one has sufficient control over the numerical errors incurred. This, and the complexity of many of these simulations, are some of the reasons why efficient spectral methods have been popular in DNS.

Orszag and Patterson used Fourier spectral methods in all three coordinate directions, while simulations of channel flows often employ Fourier expansions in the homogeneous directions and Chebyshev polynomials in the non-homogeneous wall-normal direction. The first published DNS of a more complex geometry [1] used spectral element discretisation [2, 5, 10], combining the exponential convergence of global spectral methods with the ability to represent complex geometries.

Accurate simulations of turbulent flow have the potential to provide new insight into important flow phenomena, through their extensive amounts of details. However, immensely detailed simulation data are of little use if they cannot be trusted. Thus it is essential that the errors in the simulation results are sufficiently low, and for this purpose high-order and spectral methods are superior. Numerical methods with exponential convergence make it possible to drive the error down to a level that is unattainable for lower order methods, without unfeasibly high resolution. The absence of turbulence models makes the discretisation the primary source of error in a direct numerical simulation.

We want to develop a new DNS code based on the spectral element method. This will allow us to perform highly accurate simulations of turbulent flow in complex geometries. We would also like to be able to simulate inertial particles being advected by the flow, and a Lagrangian point-particle methodology will be implemented as part of the code. The code must be parallelised and able to run on a large number of processors, to enable us to simulate complex turbulent flows.

The mathematical background of the methods used and some implementation details are discussed in the following sections, before we test the code with a series of benchmark simulations in the results section. As the code is designed for turbulent simulations, we are particularly interested in how the dominance of advection affects the error in the simulation results, for different forms of the discrete advection operator.

Mathematical description

We want to solve the incompressible Navier-Stokes equations using a spectral element method, based on the Galerkin formulation for N_{el} conforming deformed hexahedral elements.

We start with the weak form of the incompressible Navier-Stokes equations, i.e. we want to find $(\boldsymbol{u}(t), p(t)) \in X \times Y$ such that for $t \in (0, T)$

$$\left(\boldsymbol{v}, \frac{\partial \boldsymbol{u}}{\partial t}\right) + (\boldsymbol{v}, \boldsymbol{u} \cdot \nabla \boldsymbol{u}) + \nu \left(\nabla \boldsymbol{v}, \nabla \boldsymbol{u}\right) - \frac{1}{\rho} \left(\nabla \cdot \boldsymbol{v}, p\right) = \left(\boldsymbol{v}, \boldsymbol{f}\right), \quad \forall \boldsymbol{v} \in X \equiv H_0^1(\Omega)^3, \tag{1a}$$

$$\left(q, \nabla \cdot \boldsymbol{u}\right) = 0, \quad \forall q \in Y \equiv L_0^2(\Omega), \tag{1b}$$

where the spaces are defined as

$$H_0^1(\Omega) = \left\{ v \in H^1(\Omega) \mid v = 0 \text{ on } \partial\Omega \right\}, \tag{2}$$

$$L_0^2(\Omega) = \left\{ q \in L^2(\Omega) \,\middle|\, \int_\Omega q \; dx \; = 0 \right\}. \tag{3}$$

Non-zero Dirichlet boundary conditions are imposed by lifting the solution, and $(q, \boldsymbol{v})$ denotes the inner product

$$(q, \boldsymbol{v}) = \int_\Omega q \boldsymbol{v} \, d\Omega \,. \tag{4}$$

The discrete spaces of velocity (X_N) and pressure (Y_N) are subspaces of X and Y, formed using polynomials of degree $\leq N$. We use a nodal basis of high-order Lagrangian interpolants through the Gauss-Lobatto-Legendre points.

To solve the discretised equations we use a high-order dual splitting scheme based on stiffly stable time integrators, developed by Karniadakis, Israeli and Orszag [4]. We use an explicit integrator of order J_e for the advection terms, an implicit integrator of order J_i for the diffusion terms and an explicit integrator of order J_p for the pressure boundary conditions. This gives the semi-discrete system

$$\frac{\tilde{\boldsymbol{u}} - \sum_{q=0}^{J_i-1} \alpha_q \boldsymbol{u}^{n-q}}{\Delta t} = - \sum_{q=0}^{J_e-1} \beta_q \left[\left(\boldsymbol{u} \cdot \nabla \right) \boldsymbol{u} \right]^{n-q} + \boldsymbol{f}, \tag{5a}$$

$$\frac{\tilde{\tilde{\boldsymbol{u}}} - \tilde{\boldsymbol{u}}}{\Delta t} = -\frac{1}{\rho} \nabla p^{n+1}, \tag{5b}$$

$$\frac{\gamma_0 \boldsymbol{u}^{n+1} - \tilde{\tilde{\boldsymbol{u}}}}{\Delta t} = \nu \nabla^2 \boldsymbol{u}^{n+1}, \tag{5c}$$

with Neumann pressure boundary conditions given by

$$\begin{aligned} \boldsymbol{n} \cdot \nabla p^{n+1} = -\rho \Bigg[\frac{\partial \boldsymbol{u}}{\partial t}^{n+1} + \nu \sum_{q=0}^{J_p-1} \beta_q \left(\nabla \times \left(\nabla \times \boldsymbol{u} \right) \right)^{n-q} - \boldsymbol{f}^{n+1} \\ + \sum_{q=0}^{J_e-1} \beta_q \left[\left(\boldsymbol{u} \cdot \nabla \right) \boldsymbol{u} \right]^{n-q} \Bigg] \cdot \boldsymbol{n}. \end{aligned} \tag{6}$$

The constants α_q, β_q and γ_0 are the integration weights for the implicit and explicit stiffly stable schemes [4].

We use $J_e = J_p = J_i = 3$ to achieve third-order accuracy in time for both velocity and pressure. Taking the divergence of equation (5b), assuming $\nabla \cdot \tilde{\boldsymbol{u}} = 0$, gives a Poisson equation for the pressure, while equation (5c) gives a Helmholtz equation for each velocity component. Both the Poisson equation and the Helmholtz equations are solved using a preconditioned conjugate gradient method.

The splitting scheme has been chosen because of its third-order accuracy, and because it does not require that the inf-sup condition is satisfied [4]. The only spurious pressure mode is the hydrostatic mode, and the method has been implemented with equal-order interpolation for velocity and pressure. Using equal-order interpolation for velocity and pressure greatly simplifies the implementation.

The advection operator can be written in several different ways, namely the convective form

$$\boldsymbol{u} \cdot \nabla \boldsymbol{u}, \tag{7a}$$

the conservative form

$$\nabla \cdot \boldsymbol{u}\boldsymbol{u}, \tag{7b}$$

and the skew-symmteric form

$$\frac{1}{2}\left(\boldsymbol{u} \cdot \nabla \boldsymbol{u} + \nabla \cdot \boldsymbol{u}\boldsymbol{u}\right). \tag{7c}$$

For the continuous equations, these three forms are equivalent, but the three discrete operators are not. There is no clear evidence to suggest one form is always superior, but the skew-symmetric form is the only one with purely imaginary eigenvalues [9]. However, it is also the most computationally expensive.

The trajectories of inertial spherical particles dispersed in the flow are simulated using a one-way coupled Lagrangian point-particle approach. The point-particle assumption implies that the particles are assumed to be much smaller than the smallest fluid scales. We use a greatly simplified version of the Maxey-Riley equation [6], where we assume that the particles are truly much smaller than the smallest fluid scales, and that their density is much greater than the fluid density. Assuming the particles are heavy allows us to neglect the added mass force, and more importantly the Basset force, the inclusion of which greatly complicates the particle force computation. The resulting equation is

$$m\frac{d\boldsymbol{u}_p}{dt} = 3\pi\nu\rho D\left(\boldsymbol{u} - \boldsymbol{u}_p\right) + m\boldsymbol{g}, \tag{8}$$

where $\boldsymbol{u}_p$ is the particle velocity, D is the particle diameter and m is the particle mass. Additional terms and corrections could be implemented to relax the assumptions necessary for the equation to hold.

The particle equation is integrated using an explicit third-order stiffly stable scheme. Fluid velocities in the particle positions are computed with high-order polynomial interpolation, using the same basis as the one used to discretise the Navier-Stokes equations. High-order polynomial interpolation will be quite computationally expensive for a large number of particles, but we avoid the additional error that would otherwise be caused by using low-order interpolation.

Implementation

The solution method sketched out in the previous section has been implemented in a C program, with MPI for distributed memory parallelism and OpenMP for shared memory parallelism. The BLAS library has been extensively used for matrix and vector operations, and the performance of the BLAS matrix-matrix multiplication routine `DGEMM` is crucial for the overall performance of the code. An eigenvalue routine from the LAPACK library is used to find the Gauss-Lobatto-Legendre points. Message passing communication during the simulation is limited to one `MPI_Alltoallv` for the direct stiffness summation, and one `MPI_Allreduce` to implement the global norm needed in the conjugate gradient solver.

Benchmark

A challenge when testing Navier-Stokes solvers is finding suited test cases with exact analytical solutions. Many analytical solutions are for degenerate cases where one or more of the terms are equal to zero. Ethier and Steinman [3] presented a solution to the three-dimensional incompressible Navier-Stokes equations without body forces, where the unsteady terms balance the viscous terms, and the advective terms balance the pressure gradient. The solution is given in equations 9a–9d, and is valid for any geometry and at any Reynolds number.

$$u = -a\left[\mathrm{e}^{ax}\sin(ay+dz) + \mathrm{e}^{az}\cos(ax+dy)\right]\mathrm{e}^{-d^2t}, \tag{9a}$$

$$v = -a\left[\mathrm{e}^{ay}\sin(az+dx) + \mathrm{e}^{ax}\cos(ay+dz)\right]\mathrm{e}^{-d^2t}, \tag{9b}$$

$$w = -a\left[\mathrm{e}^{az}\sin(ax+dy) + \mathrm{e}^{ay}\cos(az+dx)\right]\mathrm{e}^{-d^2t}, \tag{9c}$$

$$\begin{aligned} p = \; & -\tfrac{a^2}{2}\left[\mathrm{e}^{2ax} + \mathrm{e}^{2ay} + \mathrm{e}^{2az} + 2\sin(ax+dy)\cos(az+dx)\mathrm{e}^{a(y+z)}\right. \\ & + 2\sin(ay+dz)\cos(ax+dy)\mathrm{e}^{a(z+x)} \\ & \left. + 2\sin(az+dx)\cos(ay+dz)\mathrm{e}^{a(x+y)}\right]\mathrm{e}^{-2d^2t} \end{aligned} \tag{9d}$$

This flow is a transient three-dimensional vortex flow well suited to test the accuracy in the approximation of all the different terms in the Navier-Stokes equations. Because this solution is valid at any Reynolds number, we can use it to study the error convergence both in advection-dominated and diffusion-dominated flows.

Results

For our test simulations we have used $a = \pi/4$ and $d = \pi/2$ and compared with the exact solution at $t = 0.1$. The solution is found on the cubic domain $\Omega = (-1, 1) \times (-1, 1) \times (-1, 1)$, represented using eight hexahedral spectral elements of order N. Viscosity and density are chosen such that the Reynolds number is $\mathrm{Re} = 1$. Dirichlet boundary conditions for the velocity, given by the exact solution, are prescribed on all boundaries.

We have conducted several tests with a number of different values for N and Δt and computed the error measured in a normalised maximum norm. To study the effect of the choice of advection operator, the three different advection forms (equations 7a–7c) have been tested and compared. We use $\Delta t = 10^{-4}$ for the spatial convergence tests and $N = 11$ for the temporal convergence tests. This ensures that temporal errors are negligible in the spatial convergence tests and vice versa.

Figures 1 and 2 show the error in the velocity and pressure, respectively, for the convective, conservative and skew-symmetric advection operators. There are mostly small differences between the three advection forms, but the convective form appears to give the smallest velocity

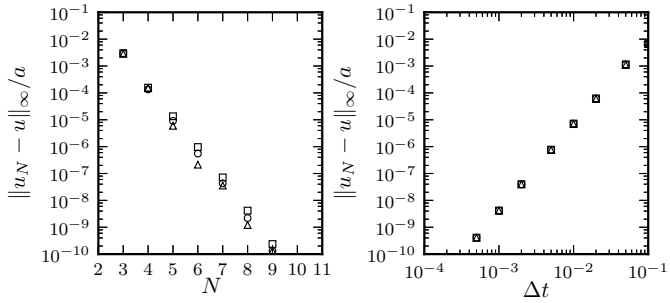

Figure 1: Error in approximate solution u_N computed for skew-symmetric advection operator ($\bigcirc$), conservative advection operator ($\square$) and convective advection operator ($\triangle$), as a function of N (left) and Δt (right).

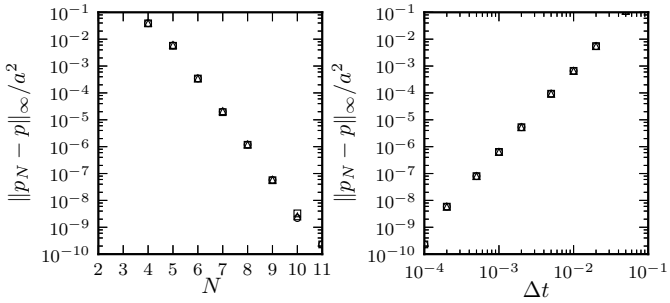

Figure 2: Error in approximate pressure p_N for skew-symmetric ($\bigcirc$), conservative ($\square$) and convective ($\triangle$) advection operator, as a function of N (left) and Δt (right).

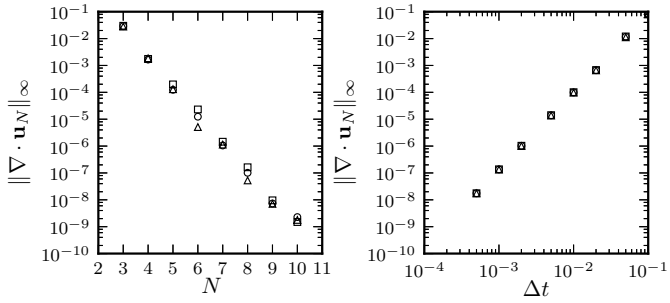

Figure 3: Maximum divergence as a function of N (left) and Δt (right), for skew-symmetric ($\bigcirc$), conservative ($\square$) and convective ($\triangle$) advection operator.

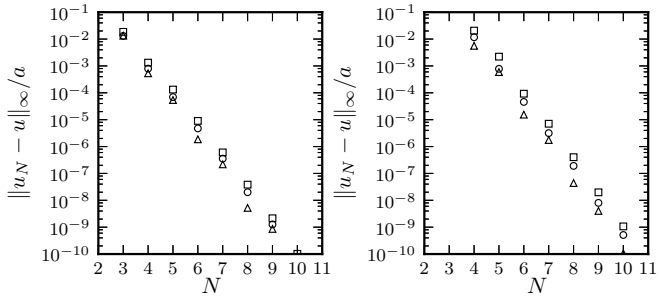

Figure 4: Error in approximate solution u_N for skew-symmetric advection operator ($\bigcirc$), conservative advection operator ($\square$) and convective advection operator ($\triangle$), as a function of N for $\mathrm{Re} = 10$ (left) and $\mathrm{Re} = 100$ (right).

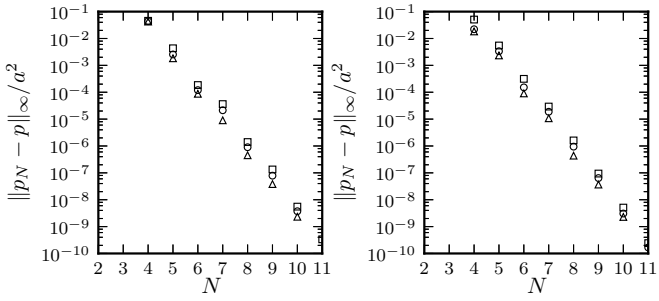

Figure 5: Error in approximate pressure p_N for skew-symmetric ($\bigcirc$), conservative ($\square$) and convective ($\triangle$) advection operator, as a function of N for $\mathrm{Re} = 10$ (left) and $\mathrm{Re} = 100$ (right).

error. The error in the pressure is largely unaffected by the choice of advection operator. In figure 3 we see the maximum divergence of the velocity field, and how it is affected by N and Δt. Because the splitting scheme does not project the velocity on the subspace of solenoidal vector functions, the incompressibility is part of the convergence process. Choice of advection operator has some effect on the divergence, and the convective form appears to perform slightly better than the two others. For both error plots and the divergence plot, we observe exponential convergence in space, and third-order algebraic convergence in time, like we expect.

In order to shed some light on the importance of the discrete form of the advection term in more advection dominated flows, two extra sets of simulations with $\mathrm{Re} = 10$ and $\mathrm{Re} = 100$ have been completed. The time step is chosen to be $\Delta t = 10^{-5}$ for all values of N, to eliminate temporal discretisation errors. The error in the approximate velocity is plotted in figure 4 for both Reynolds numbers, and we observe that the difference between the three advection operator forms increase with increasing Reynolds number. At $\mathrm{Re} = 100$ there is roughly an order of magnitude difference in the error, between the convective advection operator, which has the smallest error, and the conservative operator, which has the largest error.

In figure 5 we observe that the pressure is less affected by the choice of advection operator, but also here the differences are significant at $\mathrm{Re} = 100$. Again, the convective advection operator incurs the smallest errors. For the velocity divergence (figure 6), the convective advection operator is an order of magnitude better than the conservative operator, while the skew-symmetric form lies somewhere in between.

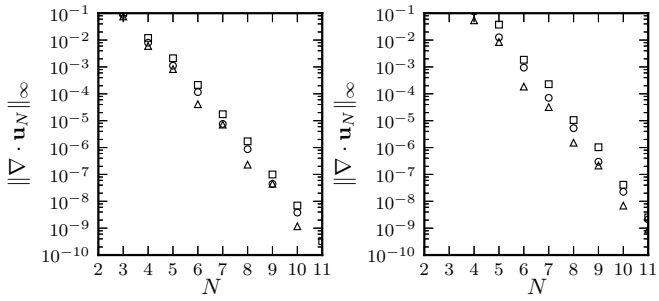

Figure 6: Maximum divergence as a function of N for $\mathrm{Re} = 10$ (left) and $\mathrm{Re} = 100$ (right), for skew-symmetric ($\bigcirc$), conservative ($\square$) and convective ($\triangle$) advection operator.

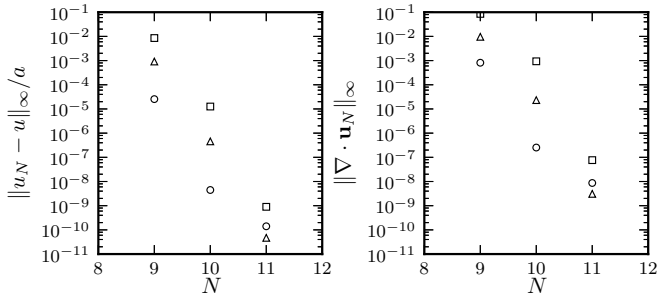

Figure 7: Error in approximate x-velocity u_N (left) and maximum divergence (right), for skew-symmetric ($\bigcirc$), conservative ($\square$) and convective ($\triangle$) advection operator, at $\mathrm{Re} = 1000$.

A comparison of the three advection forms at an even higher Reynolds number of 1000 is shown in figure 7, for $\Delta t = 2 \cdot 10^{-6}$. At this Reynolds number, aliasing errors dominate and stable results are only obtained for $N \geq 9$. For $N = 9$ and $N = 10$, the reduced aliasing error in the skew-symmetric treatment, clearly makes it superior to the convective and the conservative advection treatment. At the highest spatial resolution, $N = 11$, the convective form is once again the one with the smallest error.

The skew-symmetric form is often the preferred choice due to its purely imaginary eigenvalues, although many of our tests indicate performance inferior to the convective form. This is most likely caused by the application if inexact Dirichlet velocity boundary conditions [9], as the skew-symmetric form requires a more exact representation of the boundary conditions. At Reynolds number 1000, however, the increased aliasing error in the convective form dominates, making the skew-symmetric form the preferred choice for $N \leq 10$.

Conclusion

We have successfully implemented a Navier-Stokes solver based on the spectral element method in a simulation code designed for direct numerical simulations of turbulent flow. Through simple, but relevant, benchmark tests, we have shown that we get exponential convergence in space and third-order convergence in time.

Tests of the different discrete formulations of the advection operator have revealed that there are mainly small differences in the errors in both pressure and velocity at a Reynolds number of unity. At higher Reynolds numbers, however, the differences can be highly significant, and

the convective form performs better than the conservative and skew-symmetric forms in most of our tests. The results do not provide sufficient grounds for formulating general guidelines for the choice of advection operator, but illustrate the implications of this choice for the accuracy of the results.

References

[1] D. C.Chu and G. E.Karniadakis A direct numerical simulation of laminar and turbulent flow over riblet-mounted surfaces *J. Fluid Mech.*, **vol.250**, 1–42, 1993.

[2] M. O.Deville, P. F.Fischer and E. H.Mund *High-Order Methods for Incompressible Fluid Flow* Cambridge University Press, 2002.

[3] C. R.Ethier and D. A.Steinman Exact fully 3D Navier-Stokes solutions for benchmarking *Int. J. Numer. Methods Fluids*, **vol.19**, 369–375, 1994.

[4] G. E.Karniadakis, M.Israeli and S. A.Orszag High-order splitting methods for the incompressible Navier-Stokes equations *J. Comp. Phys.*, **vol.97**, 414–443, 1991.

[5] G. E.Karniadakis and S. J.Sherwin *Spectral/hp Element Mehtods for Computational Fluid Dynamics* Oxford University Press, 2005.

[6] M. R.Maxey and J. J.Riley Equation of motion for a small rigid sphere in a nonuniform flow *Phys. Fluids*, **vol.26**, 883–889, 1983.

[7] P.Moin and K.Mahesh Direct numerical simulation: A tool in turbulence research *Annu. Rev. Fluid Mech.*, **vol.30**, 539–578, 1998.

[8] S. A.Orszag and G. S.Patterson, Jr. Numerical simulation of three-dimensional homogeneous isotropic turbulence *Phys. Rev. Lett.*, **vol.28**, 76–79, 1972.

[9] E. M.Rønquist Convection treatment using spectral elements of different order *Int. J. Numer. Methods Fluids*, **vol.22**, 241–264, 1996.

[10] E. M.Rønquist MA8502 Numerical solution of partial differential equations Course material, Department of Mathematical Sciences, NTNU, 2012.

Part III

Particle clustering

Chapter 7

Particle dynamics and examples of clustering

Particles moving in turbulent flow are often inhomogenously distributed, forming areas with higher than average concentration. This tendency for the particles to distribute inhomogeneously is referred to as clustering or preferential concentration, and the prominence of this phenomenon will depend on the particle type as well as the flow conditions. Particles with very low inertia will typically follow the flow passively as tracers, while particles with very high inertia will remain almost unaffected by the turbulence fluctuations. It is between these two limits that we find the particles with the strongest tendency to cluster.

Maxey and Riley (1983) derived an equation for the motion of a small spherical particle in an unsteady non-uniform flow at low Reynolds number. The equation, know as the Maxey-Riley equation, is

$$\begin{aligned} m\frac{d\boldsymbol{V}}{dt} = m\boldsymbol{g} + \frac{m}{\rho_p}\left[-\nabla p + \mu\nabla^2\boldsymbol{u}\right] + 6\pi\mu a\left[(\boldsymbol{u}-\boldsymbol{V}) + \frac{a^2}{6}\nabla^2\boldsymbol{u}\right] \\ + \frac{1}{2}\frac{\rho}{\rho_p}m\frac{d}{dt}\left[(\boldsymbol{u}-\boldsymbol{V}) + \frac{a^2}{10}\nabla^2\boldsymbol{u}\right] \\ + 6\pi\mu a^2\int_0^t \frac{\frac{d}{d\tau}\left((\boldsymbol{u}-\boldsymbol{V}) + \frac{a^2}{6}\nabla^2\boldsymbol{u}\right)}{\left[\pi\mu\rho^{-1}(t-\tau)\right]^{1/2}}\,d\tau\,. \end{aligned} \quad (7.1)$$

$\boldsymbol{V}$ is the velocity of a particle with radius a, density ρ_p and mass m. The velocity $\boldsymbol{u}$ and pressure p of the fluid, with viscosity μ and density ρ, are evaluated at the particle location $\boldsymbol{X}$.

Equation (7.1) is Newton's second law of motion for a spherical point-particle in a viscous flow with five types of forces on the right hand side. The first force is the gravitational body force, where $\boldsymbol{g}$ is the acceleration of gravity vector, while the rest of the terms are fluid forces. The four different kinds of fluid forces, from left to right, are: pressure and shear stress from undisturbed flow, steady state Stokes drag force, added mass force and Basset history force.

Terms proportional to $a^2\nabla^2\boldsymbol{u}$ are Faxén laws correcting for the curvature of the flow. These are usually neglected because of the particle's small size. The Basset history force is particularly challenging to compute because it requires integration along the particle path from time $t = 0$.

In gas flows with suspended solid particles, it is quite common that $\rho/\rho_p \ll 1$, in which case the equation of motion (neglecting the Faxén laws) is

$$m\frac{d\boldsymbol{V}}{dt} = m\boldsymbol{g} + 6\pi\mu a(\boldsymbol{u} - \boldsymbol{V}). \tag{7.2}$$

This is the version of the equation which is typically used in numerical simulations, most often without the gravity term.

There are several possible extensions to equation (7.1). One is the inclusion of lift forces. For a particle with finite radius, a velocity gradient will cause a lift force, due to the pressure distribution developed on the particle (Saffman, 1965). In addition to this, the rotation of the particle will cause a Magnus force on the particle (Rubinow and Keller, 1961). Both forces can be neglected, and usually are neglected, when the particle radius is small.

7.1 Particle motion in rigid-body vortex

We will use a simple two-dimensional example to illustrate how particle inertia and particle density affect the motion of the particle. In this example we will include the Stokes drag force and the added mass force on the particle. The equation governing the motion of the particle thus becomes

$$\frac{d\boldsymbol{V}}{dt} = \beta\frac{D\boldsymbol{u}}{Dt} + \frac{1}{\mathrm{St}}(\boldsymbol{u} - \boldsymbol{V}). \tag{7.3}$$

The particle inertia is measured by the Stokes number St, which in this case is

$$\mathrm{St} = \frac{1}{\tau_f}\frac{a^2}{9\mu}(2\rho_p + \rho), \tag{7.4}$$

where τ_f is a relevant fluid time-scale. The second parameter $\beta = 3\rho/(\rho + 2\rho_p)$ measures the relative magnitude of the fluid and particle densities. Because this example is just meant as a simple illustration, we choose to neglect gravity and the Basset history force.

We shall now see what happens if we place the particle in a rigid-body vortex, where the fluid velocity is

$$\boldsymbol{u} = (-y, x) = \boldsymbol{K}\boldsymbol{x}. \tag{7.5}$$

The equations governing the motion of the particle are then

$$\frac{d\boldsymbol{V}}{dt} = -\beta\boldsymbol{X} + \frac{1}{\mathrm{St}}(\boldsymbol{K}\boldsymbol{X} - \boldsymbol{V}) \tag{7.6a}$$

$$\frac{d\boldsymbol{X}}{dt} = \boldsymbol{V}, \tag{7.6b}$$

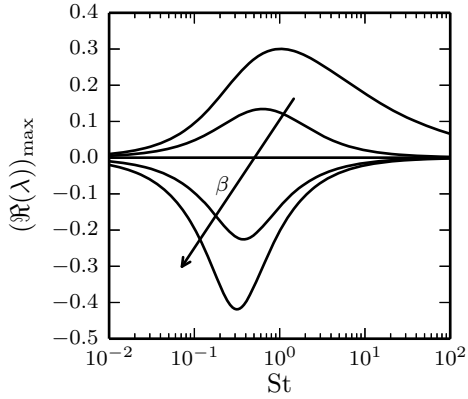

Figure 7.1: Maximum real part of eigenvalues for $\beta = 0.0$, 0.5, 1.0, 2.0 and 3.0.

which can be written as

$$\begin{bmatrix} \dot{\boldsymbol{V}} \\ \dot{\boldsymbol{X}} \end{bmatrix} = \begin{bmatrix} -\frac{1}{\mathrm{St}}\boldsymbol{I} & \frac{1}{\mathrm{St}}\boldsymbol{K} - \beta\boldsymbol{I} \\ \boldsymbol{I} & \boldsymbol{0} \end{bmatrix} \begin{bmatrix} \boldsymbol{V} \\ \boldsymbol{X} \end{bmatrix} = \boldsymbol{A} \begin{bmatrix} \boldsymbol{V} \\ \boldsymbol{X} \end{bmatrix}. \tag{7.7}$$

The eigenvalues of $\boldsymbol{A}$ are

$$\lambda_{1234} = -\frac{1}{2\mathrm{St}}(1 \pm \sqrt{1 - 4\beta\mathrm{St}^2 \pm 4\mathrm{iSt}}), \tag{7.8}$$

which can be used to predict if the particle will move out of the vortex. The maximum real part of any of the eigenvalues, is plotted in figure 7.1 as a function of St for five different values of β.

For $\beta < 1$ the maximum real part is positive, which means the particle will move farther and farther away from the centre of the vortex, as time progresses. For $\beta > 1$ the maximum real part is negative and the particle will instead move towards the centre of the vortex. As $\beta = 1$ corresponds with $\rho_p = \rho$, this leads to the expected conclusion that heavy particles are ejected from the vortex and light particles are drawn into the vortex. In a flow with many particles this means that an initially uniform distribution of particles will not remain so, as the particles are pushed away from regions with certain flow properties. We get particle clustering. Figure 7.1 also indicates that the tendency for particles to move away from (or towards) certain parts of the flow, is strongest for Stokes numbers around unity.

7.2 Clustering in a vortex array

Having shown how particles move in a simple rigid-body vortex, we will move on to a slightly more complicated flow, a steady two-dimensional vortex array. We consider the motion of particles in a flow with

$$u = \sin x \cos y, \quad v = -\cos x \sin y. \tag{7.9}$$

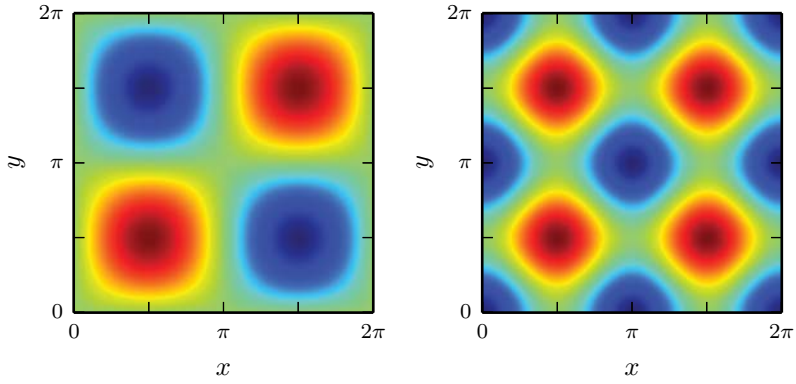

Figure 7.2: Vorticity $\omega = \partial v/\partial x - \partial u/\partial y = 2\sin x \sin y$ (left) and $-\nabla\cdot(\boldsymbol{u}\cdot\nabla)\boldsymbol{u} = -\cos 2x - \cos 2y$ (right) in a vortex array flow. High values are coloured red and low values (negative) are coloured blue.

This time we only consider heavy particles ($\beta = 0$), which means the particle equation is

$$\frac{d\boldsymbol{V}}{dt} = \frac{1}{\mathrm{St}}(\boldsymbol{u} - \boldsymbol{V}), \tag{7.10}$$

when gravity is neglected. We expect that these heavy particles will be thrown out of the vortices in the vortex array.

If we assume that the Stokes number is small, we can find an approximate expression for the particle velocity $\boldsymbol{V}$ as a perturbation expression in St. The particle velocity is

$$\boldsymbol{V} = \boldsymbol{u} - \mathrm{St}\frac{D\boldsymbol{u}}{Dt} + \mathcal{O}(\mathrm{St}^2). \tag{7.11}$$

The divergence of this particle velocity is

$$\nabla \cdot \boldsymbol{V} = -\mathrm{St}\nabla \cdot ((\boldsymbol{u} \cdot \nabla)\boldsymbol{u}), \tag{7.12}$$

which is non-zero for finite St. The particle velocity field is compressible even if the fluid flow is incompressible.

Figure 7.2 shows both the vorticity and $-\nabla \cdot ((\boldsymbol{u} \cdot \nabla)\boldsymbol{u})$, in the vortex array flow. Regions of negative divergence for the particle velocity field are associated with accumulation of particles and found in-between the vortices. Regions of positive divergence are found inside the vortices, indicating that the particles are ejected from these regions.

7.3 Gravity and Brownian motion

Gravity is included in equation (7.1), but often neglected in simulations. Another effect that is often neglected is Brownian motion. When the particle is so small that the radius is not significantly greater than the length-scale

of molecular motion, the fluid cannot be treated as a continuum and Brownian motion must be included. The importance of Brownian motion can be estimated by the relative sizes of the particle radius and the fluid mean free path λ.

In homogeneous turbulence, we can characterise the significance of gravity by comparing the gravitational settling velocity for $\rho \ll \rho_p$

$$v_g = \frac{2}{9}\frac{\rho_p}{\mu} g a^2, \tag{7.13}$$

to a small-scale fluid velocity scale $(\nu\epsilon)^{1/4}$. We get the non-dimensional ratio

$$\frac{v_g}{(\nu\epsilon)^{1/4}} = \mathrm{St}\left(\frac{\nu}{\epsilon^3}\right)^{1/4} g, \tag{7.14}$$

where the Stokes number St is based on the fluid time-scale $(\nu/\epsilon)^{1/2}$. The importance of the gravitational force will depend on the size of $(\nu/\epsilon^3)^{1/4}g$, and when the dissipation is high, gravitational effects are small compared with the effect of the turbulent motion.

In a channel flow we can do a similar exercise to find that the ratio of v_g to the friction velocity u_τ, defined such that ρu_τ^2 is the wall stress, is

$$\frac{v_g}{u_\tau} = \mathrm{St}\frac{\nu}{u_\tau^3} g, \tag{7.15}$$

when the Stokes number is defined using the fluid time-scale ν/u_τ^2. The friction Reynolds number for a channel with height $2h$ is $u_\tau h/\nu$.

For the simple equation of motion (equation (7.2)) without gravity to be a valid approximation, four conditions need to be satisfied: the particle radius must be much smaller than the fluid length-scale, the particle density much greater than the fluid density, the gravitational settling velocity much smaller than the fluid velocity scale, and the particle radius much greater than the mean free path in the fluid. In the turbulent channel flow this translates to: $au_\tau/\nu \ll 1$, $\rho_p \gg \rho$, $\nu g/u_\tau^3 \ll 1$ and $a/\lambda \gg 1$. In order to satisfy $\rho_p \gg \rho$, we need to consider a gas flow. In an air flow at ambient temperature and pressure we have $\nu \approx 10^{-5}\,\mathrm{m}^2/\mathrm{s}$ and $\lambda \approx 10^{-7}\,\mathrm{m}$. The particle radius then has to satisfy $10^{-7}\,\mathrm{m} \ll a \ll (10^{-5}\,\mathrm{m}^2/\mathrm{s})/u_\tau$, and for gravity to be negligible $u_\tau^3 \gg \nu g \approx 10^{-4}\,\mathrm{m}^3/\mathrm{s}^3$. We can make the effect of gravity arbitrarily small by choosing a large value of u_τ, but satisfying both is not possible. Gravity and Brownian motion cannot both be negligible.

In homogeneous turbulence the requirements are: $a \ll (\nu^3/\epsilon)^{1/4}$, $\rho_p \gg \rho$, $(\nu/\epsilon^3)^{1/4} g \ll 1$ and $a/\lambda \gg 1$. Inserting $\nu = 10^{-5}\,\mathrm{m}^2/\mathrm{s}$ and $\lambda = 10^{-7}\,\mathrm{m}$ gives conflicting requirements for ϵ, and thus the same conclusion that gravity and Brownian motion cannot both be negligible.

We have in the preceding paragraphs argued that the assumptions typically made, that we use in chapters 10 and 11, are impossible to strictly satisfy in real flows. However, there are conditions when both effects are quite small compared with the effect of turbulent convection. While gravity and Brownian motion will modify the particle motion and spatial clustering of the particles, the fluid mechanical mechanisms involved when particles are transported by

fluid motion will be the same. By neglecting gravity and Brownian motion, we can make the particle Stokes number the only independent particle parameter. This makes it easier to understand how particle inertia causes clustering. We investigate some of the effects of gravity in chapter 9.

7.4 Finite-radius effects

Even though the particles are assumed to be point-particles, it is not uncommon to include finite-radius effects in particle-wall collision models and drag correction terms. A finite-radius collision model and a drag correction model are included in the simulation presented in chapter 9.

Although these modifications have the potential to make the approximation more realistic, which is why they are included in chapter 9, they have the unfortunate effect of making the particle radius an independent parameter. This increases the dimensionality of the parameter space, and to be thorough one should include a range of particle radii. Because we are not specifically interested in the effect of particle size, we have not included any finite-radius effects in the studies in chapters 10 and 11.

Chapter 8

Identifying and describing particle clustering

In chapters 10 and 11, we use statistical methods based on kernel smoothing to measure and describe particle clustering. This chapter describes the methods used in chapters 10 and 11. Kernel smoothing methods are appealing, because they provide smooth functional approximations. To our knowledge, these methods have not been previously applied to study particle clustering.

8.1 Density estimation

In all forms of particle clustering, there will necessarily be more particles in some regions of the flow than in others. Thus, the most straightforward approach to describe particle clustering is to estimate the local particle number density. The particle number density, which is the expected number of particles per unit volume, can be normalised with the total number of particles to obtain the particle probability density f.

If N particles are moving in a domain Ω, then the probability of finding the position $\boldsymbol{X}$ of a randomly chosen particle in $Q \subset \Omega$ is

$$P(\boldsymbol{X} \in Q) = \int_Q f \, d\boldsymbol{x} \,, \tag{8.1}$$

with $f(\boldsymbol{x})$ a true probability distribution satisfying

$$\int_\Omega f \, d\boldsymbol{x} \, = 1. \tag{8.2}$$

The particle number density is Nf. An estimate of f will tell us a lot about how the particles are distributed.

Many studies of particle clustering in turbulent flow have used a histogram (box-counting) approach to density estimation (Eaton and Fessler, 1994; Picciotto et al., 2005), where the domain is divided into a number of boxes and the particles in each box are counted. Another and more recent idea is the use

of Voronoï diagrams to estimate the inverse of the particle density (Monchaux et al., 2010). While Voronoï diagrams provide an unbiased estimate of $1/f$, the high level of noise makes it challenging to use as a density estimation method. We will instead use kernel density estimation (Wand and Jones, 1995; Silverman, 1986), which gives a smooth functional approximation to the particle density with convergence properties superior to histograms.

Because the method can be easily applied in both two-dimensional and three-dimensional particle flow problems, we will present the general d-dimensional formulation. We assume that we have N particles and that the centre coordinate locations are given by $\boldsymbol{X}_i \in \mathbb{R}^d, i = 1, \ldots, N$. The idea behind kernel density estimation is that we estimate the local density as a sum of density kernel functions located in the centre of each particle. The multivariate probability density estimate $\hat{f}$ at $\boldsymbol{x} \in \mathbb{R}^d$ can then be expressed as

$$\hat{f}(\boldsymbol{x}; \boldsymbol{H}) = N^{-1} \sum_{i=1}^{N} |\boldsymbol{H}|^{-1/2} K(\boldsymbol{H}^{-1/2}(\boldsymbol{x} - \boldsymbol{X}_i)), \tag{8.3}$$

where $\boldsymbol{H}$ is a $d \times d$ bandwidth matrix and $K(\boldsymbol{x})$ is a kernel function. As long as $K(\boldsymbol{x})$ is a proper probability density function, $f(\boldsymbol{x}; \boldsymbol{H})$ will be a proper probability density function. The Gaussian kernel,

$$K(\boldsymbol{x}) = (2\pi)^{-d/2} \exp\left(-\frac{1}{2}\boldsymbol{x}^T\boldsymbol{x}\right), \tag{8.4}$$

is a common choice of kernel function, and the one we will use here. The choice of kernel function does not have a great impact on the accuracy of the approximation (Wand and Jones, 1995). However, the choice of bandwidth is important.

The kernel density estimate can be thought of as the result of applying a filter to a "raw" density estimate $N^{-1} \sum_{i=1}^{N} \delta(\boldsymbol{x} - \boldsymbol{X}_i)$, where $\delta(\boldsymbol{x})$ is the d-dimensional Dirac delta distribution.

Bandwidth selection is a complicated issue, and crucial to the accuracy of the kernel density estimate. There are many different approaches to bandwidth selection, some based on simple heuristic arguments, others based on sophisticated optimisation techniques. We choose a diagonal bandwidth matrix $\boldsymbol{H} = h^2\boldsymbol{I}$, as this greatly simplifies the bandwidth selection process. Equation 8.3 is then simplified to

$$\hat{f}(\boldsymbol{x}; h) = N^{-1}h^{-d} \sum_{i=1}^{N} K((\boldsymbol{x} - \boldsymbol{X}_i)/h). \tag{8.5}$$

By minimising the "asymptotic mean integrated squared error" it can be shown that the optimal bandwidth scales with N as $N^{-1/(d+4)}$ (Wand and Jones, 1995). If we choose a bandwidth proportional to a characteristic length scale and we use a fluid scale η as this length scale then, assuming there are approximately $(\eta/L)^d N$ particles inside a region of size η, we can estimate the optimal bandwidth h as

$$h = C_f \left(\frac{\eta}{L}\right)^{\frac{4}{d+4}} N^{-\frac{1}{d+4}}. \tag{8.6}$$

We can also estimate the derivatives of f as

$$\frac{\partial^r \hat{f}}{\partial x_{\alpha_1} \cdots \partial x_{\alpha_r}}(\boldsymbol{x}; h) = N^{-1} h^{-r-d} \sum_{i=1}^{N} \frac{\partial^r K}{\partial x_{\alpha_1} \cdots \partial x_{\alpha_r}}((\boldsymbol{x} - \boldsymbol{X}_i)/h), \tag{8.7}$$

and as before we can estimate an optimal bandwidth as

$$h = C_{\partial^r f} \left(\frac{\eta}{L}\right)^{\frac{2r+4}{d+2r+4}} N^{-\frac{1}{d+2r+4}}. \tag{8.8}$$

In some cases we might be interested in the probability density in the location of each particle. Kernel density estimation makes it easy to compute $\hat{f}(\boldsymbol{X}_j; h)$ for $j = 1, \ldots, N$. By realising we only need to include contributions of particles closer than $5h$ (the Gaussian kernel is very close to zero outside this), we can use an $\mathcal{O}(N \log N)$ divide-and-conquer (Bentley, 1980) algorithm.

With the right choice of bandwidth, the kernel density estimate will converge to the true probability density function when $N \to \infty$. Due to the complex shape of the probability distribution of particles in a turbulent flow, one cannot expect to get good convergence to f for realistic values of N. Rather than aiming for convergence to the true density, much can be learned about the distribution of particles by choosing a fixed bandwidth and studying clustering at that particular scale.

8.2 Measuring clustering

As it will be difficult to visually observe the magnitude of the clustering tendency, it is convenient to use an objective statistical measure of clustering. This type of dispersion index can be used to compare the relative levels of clustering of different types of particles, or at different scales. For particles whose spatial distribution is homogeneous, the number of particles inside a chosen volume will follow a Poisson distribution. This fact was used to define a "deviation from randomness" parameter $(\sigma - \sqrt{\mu})/\mu$ (Eaton and Fessler, 1994) which measures the deviation of the standard deviation σ from the Poisson distribution value of $\sqrt{\mu}$, when counting the number of particles in each box of a regular box-counting grid.

While this clustering index seems sensible and it has been extensively used in particle clustering studies (Fessler et al., 1994; Rouson and Eaton, 2001; Picciotto et al., 2005; Aliseda and Lasheras, 2011), one could create several other equally sensible indices based on the same premise (e.g. $(\sigma^2 - \mu)/\mu$ or σ^2/μ) with different results. The many different possible dispersion indices, all behave differently with changing density.

We will therefore instead of using an index based on the variance, or any other auxiliary quantity, simply use the density itself, to determine how much the particles are clustered. Using an estimate $\hat{f}$ of the probability density function, we can say that if the particles are uniformly distributed in a domain Ω with volume $\mathcal{V}_\Omega$, then

$$\mathcal{V}_\Omega(h^d \langle \hat{f} \rangle - (2\pi)^{-d/2} N^{-1}) = h^d, \tag{8.9}$$

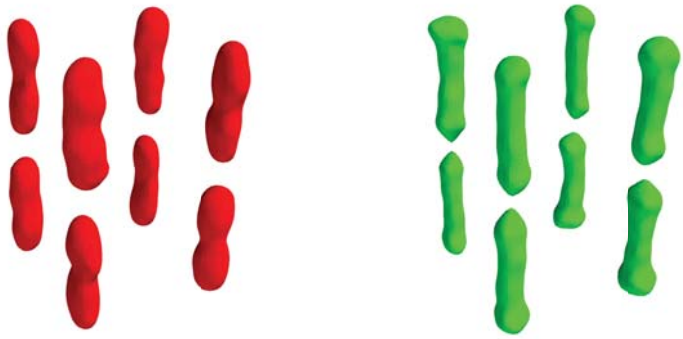

Figure 8.1: Isosurfaces of particle density $\hat{f}$ (left) and λ_2 (right), identifying particle clusters in a three-dimensional vortex array flow, with velocities $u = \cos x \sin y \cos z$, $v = -\sin x \cos y \cos z$ and $w = 0$. The figure was used in a presentation at the 14th European Turbulence Conference.

where $\langle \hat{f} \rangle$ denotes the density sampled on the particle locations. The degree of particle clustering found can then be expressed using

$$[\mathcal{V}_\Omega(h^d \langle \hat{f} \rangle - (2\pi)^{-d/2} N^{-1})]^{1/d} - h, \tag{8.10}$$

which directly measures how much more likely it is to find a particle within a distance of approximately h of another particle, than if the particles were uniformly distributed. Unlike most dispersion indices, this measure has a clear and simple interpretation. The function is almost identical to Ripley's L-function (Ripley, 1976), a commonly used concept in spatial statistics, with the main difference that we use a density estimate based on the Gaussian kernel instead of the uniform kernel.

8.3 Cluster identification

We can define particle clusters as continuous regions of high particle density. Using a kernel density estimate, particle clusters can then either be identified as connected regions of $\hat{f}$ larger than some threshold value or as a local maxima using the derivatives of $\hat{f}$. As the former should not require further explanation, we will briefly discuss the latter approach.

We can define a particle cluster as a local maximum of the probability density $\hat{f}$ in a plane. This can be expressed using the Hessian of $\hat{f}$, $\hat{F}_{ij} = \partial^2 \hat{f} / \partial x_i \partial x_j$. A local maximum in a plane requires two negative eigenvalues of $\hat{\boldsymbol{F}}$, which means the second largest eigenvalue λ_2 must be negative. A particle cluster can then be defined as a connected region of $\lambda_2(\hat{\boldsymbol{F}}) < 0$, and it is possible to illustrate clusters using iso-surfaces of λ_2.

In figure 8.1, we show a simple example of how particle clusters can be visualised, by plotting iso-surfaces of either $\hat{f}$ or λ_2. In this case, the

two methods give very similar results, while more substantial differences are expected in more complicated flows.

8.4 Particle statistics in channel flow

In channel flows, we are often interested in the mean one-dimensional particle density in the wall-normal direction. Because of the strong density gradients close to the walls, a coordinate transformation (Wand et al., 1991) can be used to improve the convergence of the kernel density estimate. We can approximate the one-dimensional wall-normal density $\hat{f}_y$ as

$$\hat{f}_y(y) = N^{-1}\sigma^{-1}\sum_{i=1}^{N} g'_\lambda(y)K((g_\lambda(y) - g_\lambda(Y_i))/\sigma), \tag{8.11}$$

with

$$g_\lambda(x) = \begin{cases} x^\lambda & x < 1 \\ 2 - (2-x)^\lambda & x > 1 \end{cases}. \tag{8.12}$$

This approach can also be used to approximate the wall-normal particle velocity as

$$\langle V \rangle_y(y) = \frac{\sum_{i=1}^{N} V_i g'_\lambda(y)K((g_\lambda(y) - g_\lambda(Y_i))/\sigma)}{\sum_{i=1}^{N} g'_\lambda(y)K((g_\lambda(y) - g_\lambda(Y_i))/\sigma)}. \tag{8.13}$$

Chapter 9

Article 3: A Voronoï analysis of preferential concentration in a vertical channel flow

Published in Physics of Fluids 25 (2013)

PHYSICS OF FLUIDS **25**, 115108 (2013)

A Voronoï analysis of preferential concentration in a vertical channel flow

Christopher Nilsen,[a] Helge I. Andersson, and Lihao Zhao
Department of Energy and Process Engineering, Norwegian University of Science and Technology, N-7491 Trondheim, Norway

(Received 31 July 2013; accepted 1 November 2013; published online 22 November 2013)

We use three-dimensional Voronoï analysis and results from a direct numerical simulation to study the preferential concentration of inertial particles in a vertical channel flow at Reynolds number 395. By comparing results in upward and downward flows with results from a channel flow without gravity, we are able to determine how gravity affects the particle clustering. Gravity increases the drift of particles towards the walls in an upward flow, while in the downward flow more particles are transported to the centre of the channel. For particles with Stokes number 100, the mean wall-normal particle velocity is positive in the entire core region. A significant increase in variance of the Voronoï probability distribution in the core region is observed in downward flow for Stokes numbers 30 and 100, indicating stronger particle clustering than in upward flow or flow without gravity. The increased clustering in the downward flow is believed to be partly caused by the reversed wall-normal drift assisting in bringing particles close together in the centre of the channel. © *2013 AIP Publishing LLC*. [http://dx.doi.org/10.1063/1.4830435]

I. INTRODUCTION

Small inertial particles suspended in a turbulent flow will form a velocity field which is not divergence free, even if the flow is incompressible. Hence, initially uniformly distributed particles will not remain so under the action of a turbulent velocity field. Instead they will tend to accumulate in certain regions of the flow, leading to a strongly inhomogeneous spatial distribution. This behaviour was first discussed by Maxey and Corrsin[1] and Maxey,[2] who discovered that particle inertia leads to accelerated settling due to preferential paths. This phenomenon is known as preferential concentration,[3–5] and has been studied extensively in both homogeneous isotropic turbulence and wall-bounded shear flows.[6,7] It is also believed to explain the increased collision rates[8] leading to accelerated rain generation in clouds,[9] and it is essential in the formation of aggregates.[10] In dense particle suspensions particle clustering is crucial in understanding the local rheological properties of the mixture, as local differences in particle number density will lead to different suspension viscosities.

In homogeneous isotropic turbulence, heavy particles are seen to accumulate in strain-dominated regions, while light particles accumulate in rotation-dominated regions.[4] In a turbulent channel flow, in addition to the aforementioned effect of local preferential concentration, one observes a global effect of particles migrating towards the walls and accumulating in the viscous sublayer.[7] Often in studies of particle-suspended turbulent channel flows, gravity is neglected. However, for heavy particles the gravitational acceleration can have important effects in both horizontal and vertical channel flows. In horizontal channel flows the primary effect is to accelerate settling towards the bottom wall, while in vertical flows the first effect of gravity is to decorrelate the particle velocity with the local fluid velocity. Marchioli, Picciotto, and Soldati[11] and Uijttewaal and Oliemans[12] studied the effect of gravity in channel and pipe flows and observed that the deposition of particles

[a]Electronic mail: christopher.nilsen@ntnu.no

 © 2013 AIP Publishing LLC

increased in an upward flow and decreased in a downward flow. A study of particle deposition in vertical and horizontal duct flows was conducted by Zhang and Ahmadi.[13]

Even though particle clustering is easily observed simply by studying visualisations of the particle positions, more sophisticated techniques are needed to quantify and measure specific features of the clustering. Monchaux, Bourgoin, and Cartellier[14] reviewed many of the different methods available used to describe clustering. A fairly recent idea is the use of Voronoï diagrams.[15,16] Voronoï diagrams are convenient because they provide a specific volume (inverse particle number density) in space without the need for prescribing a grid. Monchaux, Bourgoin, and Cartellier[15] used two-dimensional Voronoï analysis to study clustering in homogeneous isotropic turbulence. They observed a lognormal distribution of Voronoï areas and a self-similar cluster structure. Also Tagawa *et al.*[16] studied particle clustering in homogeneous turbulence, but used three-dimensional Voronoï diagrams and included both light and heavy particles. The probability density functions of the Voronoï volumes were fitted with gamma distributions, and it was shown that light particles accumulated in high-enstrophy regions and heavy particles in low-enstrophy regions. Tagawa *et al.*[17] used Voronoï analysis to study clustering of deformable bubbles, while some of the possible biases of Voronoï concentration estimation were investigated by Monchaux.[18]

Voronoï analysis of preferential concentration has mostly been used in studies of homogeneous isotropic turbulence, but there are some recent studies that also consider shear flows. García-Villalba, Kidanemariam, and Uhlmann[19] studied the spatial distribution of large particles in a vertical channel flow and found an almost homogeneous distribution. Voronoï analysis was also used by Håkansson *et al.*[20] to study particle streaks in a turbulent half-channel flow.

Our primary goal is to map out the most important statistical properties of the particles' spatial distribution in a vertical turbulent channel flow. We will do this by using data from a direct numerical simulation of a turbulent channel flow with suspended inertial Lagrangian point-particles, and using Voronoï diagrams to compute the statistics of the spatial distribution. We will look at probability density functions and lower-order moments of the specific particle volume obtained from the Voronoï diagrams, for different particle types and flow directions. In particular, we will explore how the particle distribution is affected by particle inertia and gravity.

We start by describing the simulation and post-processing methodology in Sec. II, before discussing our main findings in Sec. III. Finally, we summarise and discuss the most interesting results and their potential implications in Sec. IV.

II. METHODOLOGY

We solve the incompressible Navier-Stokes equations in a channel geometry with no-slip boundary conditions at the walls and periodic boundary conditions in the streamwise and spanwise directions. The shear Reynolds number is $\mathrm{Re}_\tau = u_\tau h/\nu = 395$, where $u_\tau = \sqrt{\tau_w/\rho}$ is the friction velocity, ν is the kinematic viscosity, ρ is the fluid density, h is the channel half-width, and τ_w is the wall shear stress. The Reynolds number is significantly higher than what is normally used in particle-suspended turbulent channel flow simulations, where 150 and 180 are the most common values,[21,22] which will give us a wider inertial sublayer and a significantly larger core region. A shear Reynolds number of 395 is the same as that used in the middle case of Abe, Kawamura, and Matsuo[23] and Abe, Antonia, and Kawamura,[24] and corresponds to a centreline streamwise Taylor microscale Reynolds number $\mathrm{Re}_\lambda = \overline{(u^{+2})}^{1/2}\lambda^+ = 51$,[24] where $\overline{(\partial u^+/\partial x^+)^2} = \overline{u^{+2}}/\lambda^{+2}$.

The simulation code[25] uses a Fourier spectral approximation in the two periodic directions and a second-order finite-difference approximation in the wall-normal direction to solve for the three-dimensional velocity field $\boldsymbol{u} = (u, v, w)$. The domain size is $12h$ in the streamwise (x) direction, $2h$ in the wall-normal (y) direction, and $6h$ in the spanwise (z) direction. The grid resolution is 384^3 and the wall-normal grid is stretched to increase resolution in the near-wall region, with a grid size ranging from 0.19 to 3.5 wall units. A wall length unit is ν/u_τ and is used to non-dimensionalise lengths, denoted $(\cdot)^+$. Non-dimensional velocities are also marked $(\cdot)^+$ and are scaled with u_τ. Averages are made in time and the two homogeneous spatial directions (x and z) and denoted $\overline{(\cdot)}$.

The simulation was initialised from a random velocity field with mean velocity profile $\min(y^+, 2.5\log y^+ + 5.0)$ in the streamwise direction, and run until a statistically steady-state had been achieved. Into the steady turbulent velocity field the inertial particles were released, and the simulation was continued until $t = 8$, where t is made dimensionless with the time scale h/u_τ. This is equal to 3160 times the viscous time scale ν/u_τ^2 and 31.6 times the time scale of the slowest particles ($100\nu/u_\tau^2$). The particles were released at random initial positions. Here and throughout the paper random refers to "complete spatial randomness," i.e., events drawn from a three-dimensional homogeneous spatial Poisson process.

We consider the dilute limit, and the particle motion is governed by a simplified Basset-Boussinesq-Oseen equation where we, in addition to assuming point-particles, also assume that the particle density (ρ_p) is much greater than the fluid density (ρ). The equation then only includes the Schiller-Naumann[26] corrected Stokes drag force, and the gravity force, i.e.,

$$\frac{d\boldsymbol{u}_p}{dt} = \frac{C_D \mathrm{Re}_p}{24\tau_p}\left(\boldsymbol{u} - \boldsymbol{u}_p\right) + \boldsymbol{g}, \tag{1}$$

where

$$C_D = \frac{24}{\mathrm{Re}_p}\left(1 + 0.15\mathrm{Re}_p^{0.687}\right), \tag{2}$$

and $\mathrm{Re}_p = \Delta u a/\nu$ is the Reynolds number of the particle based on the magnitude of the slip velocity, $\Delta u = \|\boldsymbol{u} - \boldsymbol{u}_p\|$ and the particle radius a. The particle velocity is $\boldsymbol{u}_p$ and $\boldsymbol{u}$ is the fluid velocity in the particle position. We define a Stokes number based on the particle time scale τ_p as

$$\mathrm{St} = \frac{\tau_p}{\nu/u_\tau^2} = \frac{2\rho_p a^2 u_\tau^2}{9\rho\nu^2}. \tag{3}$$

There is no feedback from the particles on the flow, and no interaction between the particles.

In our simulation we used the five Stokes numbers 1, 5, 15, 30, and 100, and gravitational force $+g\boldsymbol{i}$, 0, and $-g\boldsymbol{i}$ corresponding with downward, non-gravitational, and upward flows, respectively. The non-dimensional particle radius is $a^+ = 0.075$ for $\mathrm{St} = 1, 5$ and $a^+ = 0.25$ for $\mathrm{St} = 15, 30, 100$. We include $N_p = 500\,000$ of each particle type, and use an elastic wall collision model with particles bouncing back when the distance from the centre of the particle to the closest wall is less than a.

Figure 1(a) shows the velocity profile compared with the linear velocity profile $\overline{u}^+ = y^+$ and the logarithmic law $\overline{u}^+ = 2.5\log y^+ + 5.1$. In Figure 1(b) we see the deviation from the logarithmic law, clearly revealing the inertial region of the channel. The velocity profile identifies $y^+ \in (0, 5)$ as the viscous layer, (5, 30) as the buffer layer, (30, 170) as the inertial layer, and (170, 395) as the core region.

Most previous computational studies on preferential concentration in wall-bounded flows are mainly focused on the near-wall region, due to the low Reynolds numbers. By using a Reynolds

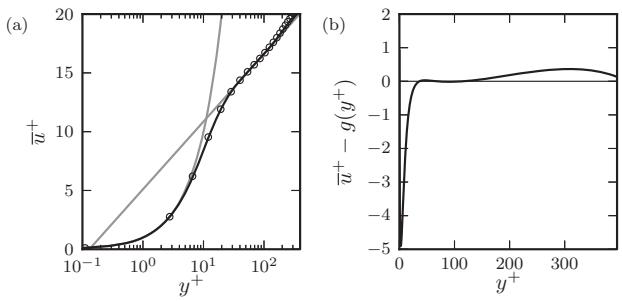

FIG. 1. (a) Mean fluid streamwise velocity $\overline{u}^+$ compared with linear velocity profile y^+, logarithmic law $g(y^+) = 2.5\log y^+ + 5.1$, and results from Abe, Kawamura, and Matsuo[23] (circles). (b) Deviation from logarithmic law $g(y^+)$.

number of 395 we observe substantial inertial and core regions, which will allow us to pay more attention to the particle motion away from the wall. Figure 1(a) also shows a comparison with the results of Abe, Kawamura, and Matsuo,[23] where we see good agreement.

To analyse the preferential concentration of particles we use Voronoï diagrams, where the whole domain is divided into subvolumes each consisting of all points being closer to one particular particle than all other particles. This provides us with a specific particle volume, or an inverse particle number density, for each particle, without having to specify a grid. The probability distribution of the Voronoï volumes can be used to measure particle clustering. We choose to close all Voronoï volumes on the boundaries of the domain, by using mirrored ghost-particles, to avoid having open Voronoï cells at the boundaries. The statistical description of random particles in the channel (as detailed in Sec. III) shows that any bias introduced at the boundaries is minimal. Voronoï diagrams are presented in more detail by Monchaux, Bourgoin, and Cartellier.[15]

The volume obtained from the Voronoï analysis is normalised to obtain $\mathcal{V} = V N_p / V_d$, where V is the volume of the Voronoï cell, N_p is the number of particles, and V_d is the total domain volume. In order to measure preferential concentration we use the probability density function of the Voronoï volumes, and in particular the variance $\sigma^2 = \overline{(\mathcal{V} - \overline{\mathcal{V}})^2}$ of this density function. A set of randomly distributed particles are also included for comparison, and analysed in exactly the same manner as the real particles.

All particle statistics reported as functions of the wall-normal coordinate y are computed on the $n = 100$ nodes $y_i = (1 - \cos((i-1)\pi/(n-1)))h, i = 1, \ldots, n$, by taking the average of all particles closest to a given node. Interpolation is used when values are needed in-between the nodes, such as when average values are needed in the particle positions. Probability density functions are computed for a subvolume by including all particles between a lower and an upper value of y.

III. RESULTS AND DISCUSSION

We expect the particles to drift towards the walls, a phenomenon that could make it impossible to get a truly steady flow until all the particles are located in the viscous sublayer. Figure 2(a) shows the mean Voronoï volume at four different distances from the wall and for St = 100, the slowest of the particles. We see that the particle distribution does not reach a steady state during the simulation, but the strongest transient is over at $t = 2$. The viscous sublayer is the part of the flow that appears to be the least steady.

In Figure 2(b) the normalised Voronoï volume variance is plotted for the same four wall-normal locations for St = 100. The variance of the Voronoï cell volume is a measure of the degree of preferential concentration[15,16] and if it is reasonably steady we can safely assume that the spatial distribution of particles is established, despite any global fluxes that are still prevalent. With the exception of the value in the viscous sublayer ($y^+ = 1$) the plots indicate that the variance is steady after approximately $t = 2$. Since there is still such a strong influx of particles into the viscous

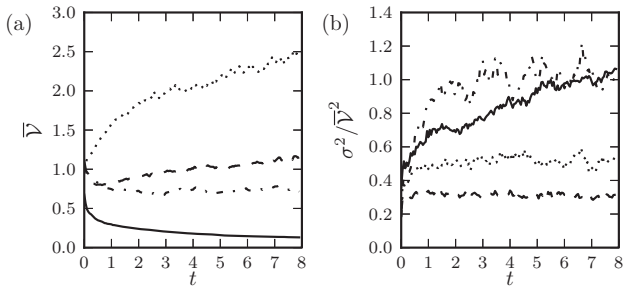

FIG. 2. (a) Mean Voronoï volume and (b) normalised variance as a function of time at $y^+ = 1$ (solid line), 20 (dashed line), 100 (dotted line), and 395 (dashed-dotted line).

sublayer, it is not surprising that also the variance is constantly changing. However, it appears as if most of the channel reaches a kind of statistically steady state. Based on the results of Figures 2(a) and 2(b), we chose to compute statistics for $t \in (2, 8)$, and all reported statistics use this time range unless otherwise stated.

A notable feature of particle-laden channel flow, as illustrated in Figure 2, is the particles' tendency to drift towards the walls. The strength of this particle drift depends on the Stokes number and flow direction relative to the gravitational force.[11] The mean Voronoï volume is plotted across the channel in upward, downward, and non-gravitational flows in Figure 3, for Stokes numbers 5, 15, 30, and 100. Randomly distributed particles are also included for comparison, and we observe a perfectly straight line at $\overline{\mathcal{V}} = 1$. In all four cases we observe that there is a flux of particles towards the walls, where we find the lowest mean Voronoï volume. This is most pronounced for $\mathrm{St} = 15$ and $\mathrm{St} = 30$, which is consistent with what has been reported previously.[11] The region around $y^+ = 100$, in the middle of the inertial sublayer, is the most depleted.

The particle drift towards the walls in the near-wall region is often explained by turbophoresis,[27,28] a mechanism causing particles to move towards regions of lower turbulence intensity, an equivalent to thermophoresis, but forced by turbulence. It has been shown[7] that turbulent motions associated with sweeps are primarily responsible for bringing the particles close to the wall. Differences observed between the three cases compared in each panel of Figure 3 indicate that the particle drift is significantly affected by gravity. Gravity changes the drift of particles, such that an increasing number of particles move towards the wall in an upward flow, while fewer particles migrate towards the wall in a downward flow. This is seen as a more strongly depleted central region in the upward flow, and a central region where particles accumulate in the downward flow.

The results at $\mathrm{St} = 100$ are particularly striking, where in the centre of the channel in the downward flow the average Voronoï volume is lower than for the random distribution, implying that there is a net flux of particles towards the centre of the channel. The region around $y^+ = 100$ is more

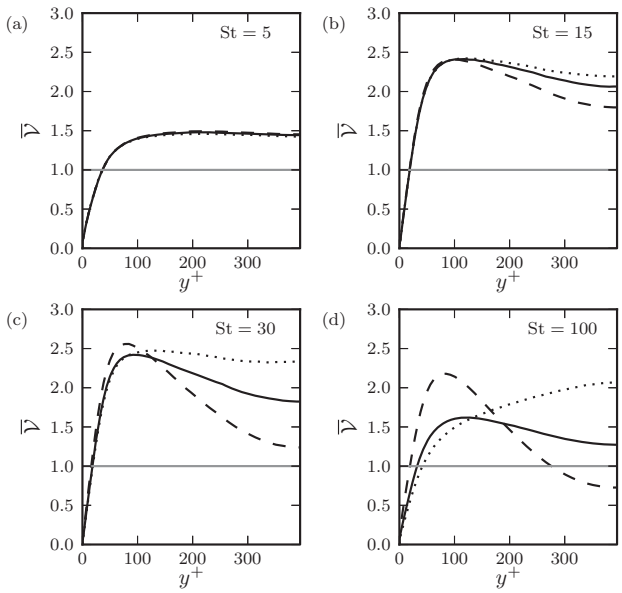

FIG. 3. Mean Voronoï volume for (a) $\mathrm{St} = 5$, (b) $\mathrm{St} = 15$, (c) $\mathrm{St} = 30$, and (d) $\mathrm{St} = 100$, in downward flow (dashed line), upward flow (dotted line), and flow without gravity (solid line), and compared with randomly distributed particles (grey line) where $\overline{\mathcal{V}} = 1$.

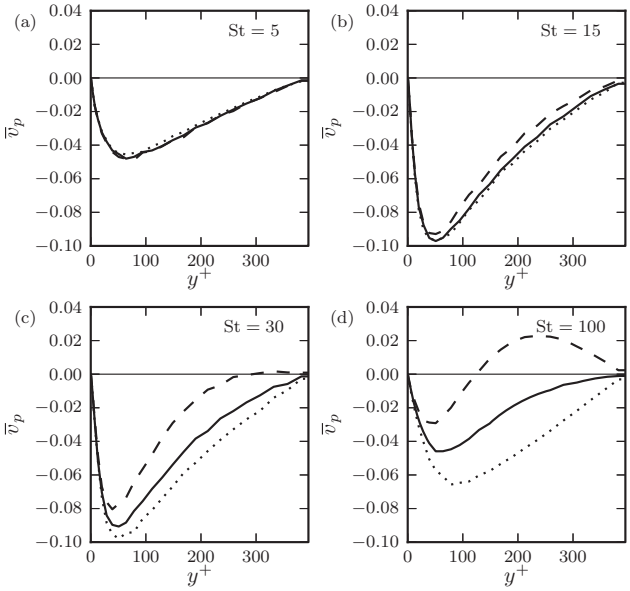

FIG. 4. Mean wall-normal particle velocity averaged from $t = 0$ until $t = 2$ for (a) St = 5, (b) St = 15, (c) St = 30, and (d) St = 100, in downward flow (dashed line), upward flow (dotted line), and flow without gravity (solid line).

depleted in the downward flow, suggesting that many of the additional particles in the centre come from this region.

An implication of the differences in particle density across the channel is that there must be a non-zero mean wall-normal velocity in the particle phase. In Figure 4 the mean wall-normal velocity averaged from $t = 0$ until $t = 2$ is shown for the same four Stokes numbers as in Figure 3. This time window is chosen because it is the part of the simulation where most of the wall-normal transport occurs. Mostly we see a negative wall-normal velocity, explaining the low values of the mean Voronoï volume close to the wall. This wall-normal velocity is highest for St = 15 and 30 and at y^+ around 100, which is consistent with what we observed in Figure 3.

In upward flow the wall-normal velocity is marginally more negative for St = 15 and 30, while the difference is significantly larger for St = 100. In the downward flow the negative wall-normal velocity is decreased and for St = 30 and 100 it changes sign in the core region. The crossover point where $\overline{v}$ changes sign from negative to positive is $y^+ \cong 300$ for St = 30 and $y^+ \cong 120$ for St = 100.

An increase in centre region particle number density in downward flow was also observed by Uijttewaal and Oliemans[12] and Marchioli, Picciotto, and Soldati,[11] and the latter's plot of wall-normal velocity reveals similar trends as those observed in Figure 4 for the downward flow. However, Marchioli, Picciotto, and Soldati[11] also showed a small increase in core region particle density in upward flow, while we observe the opposite effect. A flux of particles towards the centre is consistent with the idea of turbophoresis, where particles move towards regions of lower turbulence intensity, but such a strong dependence on gravity is more difficult to explain. Uijttewaal and Oliemans[12] provide no explanation for the increased number of particles in the centre of the channel, while Marchioli, Picciotto, and Soldati[11] try to relate this to the particle's tendency to occupy regions of high streamwise velocity, where they claim ejections are more likely. We do observe that particles tend to occupy regions of high streamwise velocity (not shown), but fail to see how this will make them more likely to be swept away from the wall by ejections, as ejections are associated with low streamwise velocity.[29] One possible explanation is that a particle falling in downward flow is more likely to be swept away by a vortex that is translating with a velocity closer to that of the particle.

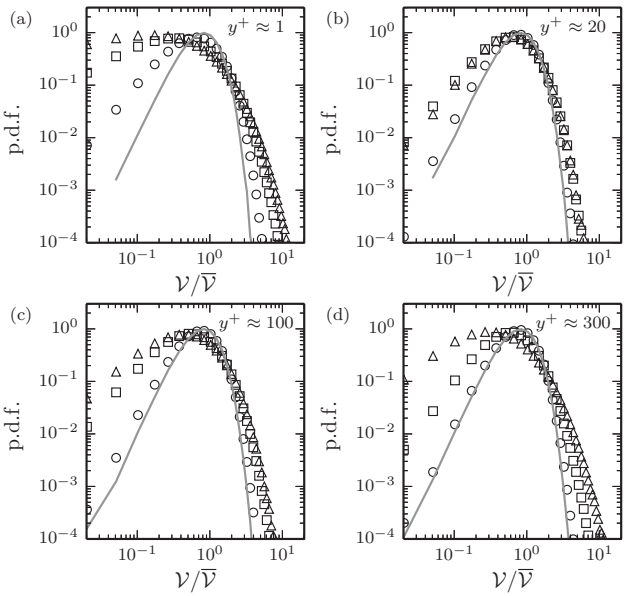

FIG. 5. Probability density functions for the normalised Voronoï volume in the four slices (a) $y^+ \in (0.5, 1.5)$, (b) $y^+ \in (19, 21)$, (c) $y^+ \in (95, 105)$, and (d) $y^+ \in (290, 310)$ for particles with St = 1 (circles), St = 5 (squares), and St = 30 (triangles) compared with randomly seeded particles (grey line). All cases are without gravity.

Because the particle is moving faster than the fluid, and $\partial \overline{u}^+/\partial y > 0$, the faster moving vortices closer to the centre will have more time to sweep the particles than the slower ones closer to the wall.

We have now looked at the global aspects of preferential concentration, in which particles drift towards certain parts of the domain. Of equal importance is what we might call local preferential concentration, the tendency for particles to cluster under the effect of the local turbulent flow field. As a means of studying this phenomenon we use the probability density function (p.d.f.) for the Voronoï volume as first suggested by Monchaux, Bourgoin, and Cartellier.[15] Because the mean value changes across the channel we cannot use a single p.d.f. for the whole channel, but instead divide the channel into several slices and compute a p.d.f. for each of them.

The p.d.f. for the Voronoï volume normalised with the local mean value ($\mathcal{V}/\overline{\mathcal{V}}$) is plotted in Figure 5 in four different wall-normal locations. Three different Stokes numbers are compared for the case without gravity. The computed distributions are compared with the distribution obtained for randomly distributed particles, and a deviation from this distribution is an indication of preferential concentration. Particles with St = 1 behave almost like tracers in most of the channel except close to the wall where there is noticeable preferential concentration also for St = 1. Also for the other Stokes numbers the largest deviation from randomness appears to be at $y^+ = 1$. Increasing Stokes number increases the preferential concentration at all four wall-normal locations.

Tagawa *et al.*[16] fitted the probability density functions of the Voronoï volumes in homogeneous turbulence with gamma distributions. Using a two-parameter distribution to fit the data is, when suitable, very convenient because it means that the standard deviation is a sufficient measure of the deviation from randomness, and thus also a sufficient measure of preferential concentration. For a gamma distribution $\overline{\mathcal{V}(\mathcal{V}-\overline{\mathcal{V}})^3} = 2\overline{(\mathcal{V}-\overline{\mathcal{V}})^2}^2$ holds, which means that the extent to which this identity holds is a measure of the suitability of the gamma distribution. This is tested in Figure 6 for all the different Stokes numbers and across the channel. The gamma distribution is seen to be a good

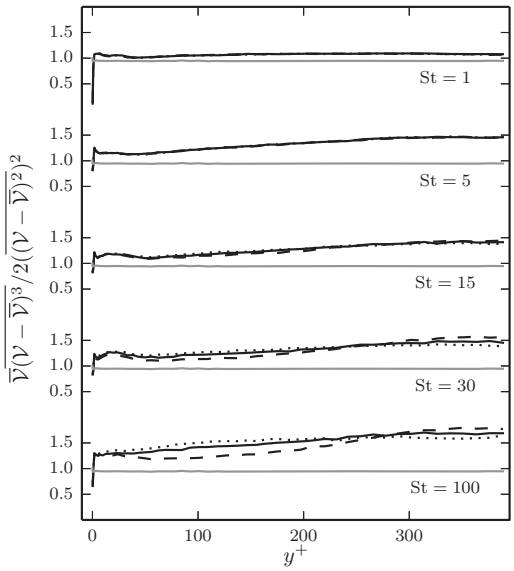

FIG. 6. Measure of suitability of gamma distribution for Stokes numbers 1 through 100 in downward flow (dashed line), upward flow (dotted line), and flow without gravity (solid line), and compared with randomly seeded particles (grey line). A value equal to unity indicates that the first three moments behave as if governed by a gamma distribution.

fit for the randomly distributed particles, as suggested by Ferenc and Néda,[30] where the plotted ratio is equal to 0.94. This strongly suggests that it is suitable to compare our results to previous three-dimensional studies, despite the fact that we are using fairly thin wall-normal slices. Thus we are expecting to find gamma distributions as observed by Tagawa *et al.*[16] in a three-dimensional Voronoï analysis, and not the lognormal distributions found by Monchaux, Bourgoin, and Cartellier[15] based on a two-dimensional analysis. We have also tested a lognormal fit for our data (not shown) but found it to be unsuited.

While a gamma distribution is a good fit for $\mathrm{St} = 1$, it cannot be generally said to be a suitable probability distribution for the other Stokes numbers, and even less so in the centre of the channel. This is surprising as one would expect the preferential concentration to behave closest to that seen in homogeneous isotropic turbulence in the centre of the channel. Comparisons between the probability distributions displayed in Figure 5 and gamma distributions (not shown) lead us to the same conclusion.

It is often assumed that preferential concentration of particles in the centre of a channel or pipe flow is similar to what is observed in homogeneous isotropic turbulence.[4] In our results, however, we find probability density functions in the centre of the channel that are more different from those observed in homogeneous turbulence, than those found close to the walls are. There are several factors at play here. First, the centre of a channel flow is neither homogeneous nor isotropic, so it is not unreasonable to expect that the clustering in the centre of a channel flow is different from that seen in homogeneous isotropic turbulence. Second, the Taylor microscale Reynolds numbers used by Tagawa *et al.*[16] were 75 and 180, while the streamwise Taylor microscale Reynolds number in the centre of our channel flow is 51. Considering the lower Reynolds number, it is not guaranteed that we would have found the same type of probability density function, even if the flow had been homogeneous and isotropic. It is not possible to determine if the observed discrepancy is primarily an effect of Reynolds number or an effect of inhomogeneity and anisotropy, without doing a channel flow simulation at a higher Reynolds number.

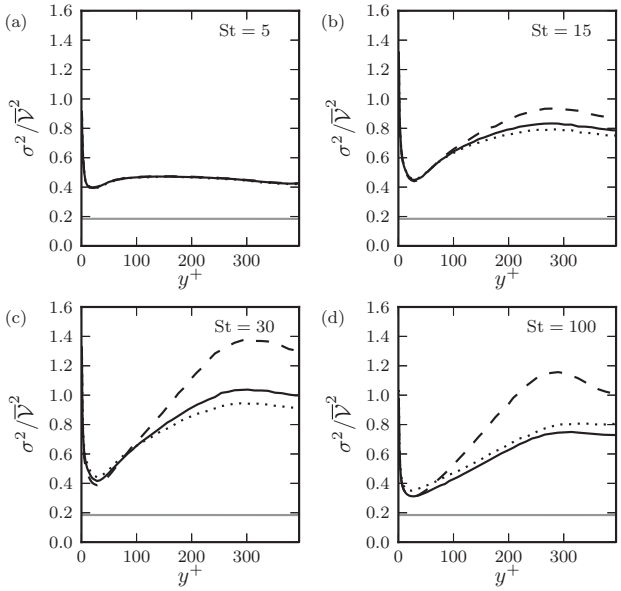

FIG. 7. Normalised variance of the Voronoï volume for particles with (a) St = 5, (b) St = 15, (c) St = 30, and (d) St = 100, for downward flow (dashed line), upward flow (dotted line), and flow without gravity (solid line), and compared with randomly distributed particles (grey line).

Particle clustering in a turbulent channel flow is too complex to be measured solely by the two first moments of the Voronoï volume distribution, but the variance should nevertheless provide a reliable measure of the degree of preferential concentration. The normalised variance is plotted in Figure 7, across the channel width. The variance has local maxima close to the wall and around the centre of the channel, indicating that the strongest clustering is found at these locations. The variance reaches its highest values for St = 30, suggesting that maximum preferential concentration is found around this Stokes number. This also corresponds with the Stokes number at which the maximum number of particles are transported to the walls (see Figure 3).

Once again gravity has significant effects in the centre of the channel. In the downward flow there is an increase in variance, indicating that preferential concentration is more prominent. This effect is strong for both St = 30 and 100.

It has been shown that the variance of the Voronoï distribution is affected by the particle density.[15–18] Because we observe an increase in particle density in the centre of the channel in downward flow (see Figure 3), it is possible that the differences in variance observed in Figure 7 are caused in part by the difference in particle density. To test this, the Voronoï analysis has not only been conducted on the full set of particles, but also on sets subjected to random thinning. Particle numbers from $N_p/32$ to N_p have been used, and the results are shown in Figure 8 for $y^+ = 300$. While it is clear that the variance does depend on the particle density, the effect is not strong enough to explain the differences observed in Figure 7. It is therefore made clear that there is a significant difference between the degree of preferential concentration in the core region of a downward channel flow and a channel flow without gravity. The largest difference is observed for St = 100.

The most common understanding of clustering, that heavy particles are thrown out of vortices,[2,4] would predict that the increased decorrelation between particle and fluid velocity caused by gravity should lead to less clustering. Thus, the observed increased clustering in downward flow is unexpected. Strong gravity was also shown to decrease preferential concentration in a cellular flow by Maxey and Corrsin.[1] However, it is also known[31] that gravity will cause particles to accumulate in

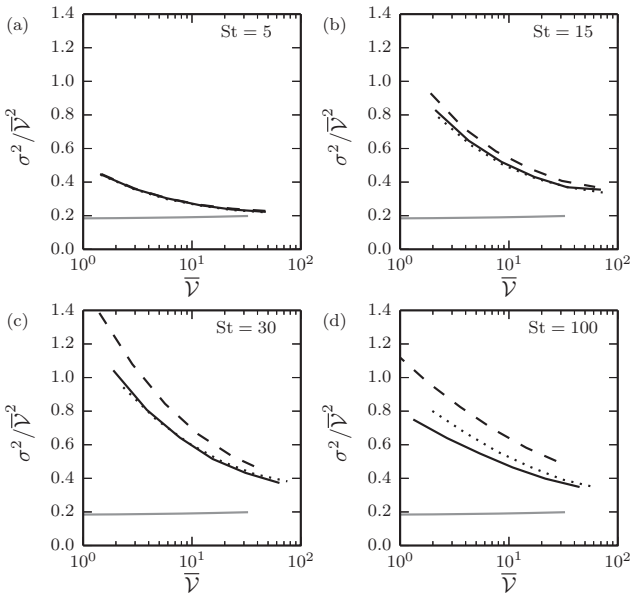

FIG. 8. Normalised variance under random thinning at $y^+ = 300$ for particles with (a) St = 5, (b) St = 15, (c) St = 30, and (d) St = 100, for downward flow (dashed line), upward flow (dotted line), and flow without gravity (solid line).

downward moving fluid; the particles will preferentially populate the regions of high streamwise velocity in a downward flow. This could in cases of weak gravity lead to increased clustering.

If we instead understand clustering in terms of the effect of "caustics"[9,32,33] a mechanism explaining our results is revealed. Preferential particle concentration is possible also in flows without semi-coherent vortex structures. When inertial particles move in a non-constant velocity field, faster particles will overtake the slower particles and the particle distribution "folds over itself" and a higher particle concentration occurs in certain regions.[32] As seen in Figure 4 more particles move towards the centre in a downward flow. The wall-normal drift makes caustic clustering more likely because faster moving particles overtake the slower ones, an effect which is also much more likely to occur when there is a negative velocity gradient in the direction of the mean velocity. This effect is most prominent in the beginning of the simulation when the wall-normal velocities are highest, but particle clusters can be long-lasting. When the particles get close together they are exposed to the same fluid velocity, and are thus likely to stay together. In the point-particle framework we employ there is nothing that prevents the particles from essentially occupying the same space. Tagawa *et al.*[16] showed that the lifetime of clusters of heavy particles was much longer than the lifetime of the fluid structures responsible for forming them. The additional effect of particles preferentially concentrating in regions of high streamwise velocity also increases the probability of particle-overtaking and the following clustering to occur in the streamwise direction.

IV. CONCLUSION

We have studied the motion of inertial particles in vertical channel flow, and tried to determine the extent to which they tend to cluster. A direct numerical simulation at $\mathrm{Re}_\tau = 395$ has been performed with particles ranging from Stokes numbers 1 to 100, and in both upward and downward flows, and flow without gravity. The preferential concentration in channel flow takes two distinct forms: a global preferential concentration causing higher particle density in the near-wall region

and a local preferential concentration causing particles to cluster under the effect of the local flow structures.

As expected there is a drift of particles towards the wall, and this effect is most prominent for Stokes numbers 15 and 30. Gravity alters this drift such that in an upward flow more particles are transported to the walls, and in a downward flow more particles move towards the centre of the channel. We believe this is partly because particles in a downward flow move with a velocity that is closer to that of adjacent vortices on the core side than on the wall side, which gives the former vortices more time to sweep the particles towards the centre.

We use Voronoï diagrams to analyse the preferential concentration of particles in the channel. Probability density functions for the Voronoï volume deviate considerably from the gamma distributions used as approximations in homogeneous isotropic turbulence by Tagawa *et al.*,[16] particularly in the centre of the channel. It is not clear if this represents a real physical difference between the clustering in the centre of a channel flow and in homogeneous isotropic turbulence, or if it is because the Taylor microscale Reynolds number is lower in the channel.

We are primarily concerned with the effect of gravity and observe that gravity increases the degree of preferential concentration in the centre of the channel in a downward flow, for Stokes numbers 30 and 100. This is indicated by higher values of the variance in the core region, and confirmed to be a real physical effect by showing that it is not caused indirectly by a change in particle density. Increased clustering is believed to be caused by the effect of caustics; fast particles overtaking slower particles and causing local increases in particle density. In the downward flow, a wall-normal drift of particles towards the centre of the channel and the resultant velocity gradient gives fast wall-normal moving particles overtaking the slower ones and causing clustering. In addition to this, particles in a downward flow are more likely to be located in the regions of high streamwise velocity due to their preference for downward moving fluid.

As we have seen in several examples, the effects of gravity are far from insignificant and sometimes quite surprising, and ignoring gravity in simulations could in some cases lead to unphysical conclusions. Increased preferential concentration in downward flow means that growth of aggregates and coalescence of droplets are more likely to occur in downward flow for heavy particles. In denser suspensions the rheological properties will vary across the channel in both upward and downward flows, but even more so in the latter case.

ACKNOWLEDGMENTS

The work was supported by The Research Council of Norway (Programme for Supercomputing) through a grant of computing time on the Hexagon compute cluster (Cray XE6m-200) in Bergen.

[1] M. R. Maxey and S. Corrsin, "Gravitational settling of aerosol particles in randomly orientated cellular flow fields," J. Atmos. Sci. **43**, 1112–1134 (1986).
[2] M. R. Maxey, "The gravitational settling of aerosol particles in homogeneous turbulence and random flow fields," J. Fluid Mech. **174**, 441–465 (1987).
[3] K. D. Squires and J. K. Eaton, "Preferential concentration of particles by turbulence," Phys. Fluids A **3**, 1169–1178 (1991).
[4] J. K. Eaton and J. R. Fessler, "Preferential concentration of particles by turbulence," Int. J. Multiphase Flow **20**, 169–209 (1994).
[5] S. Balachandar and J. K. Eaton, "Turbulent dispersed multiphase flow," Annu. Rev. Fluid Mech. **42**, 111–133 (2010).
[6] D. Rouson and J. K. Eaton, "On the preferential concentration of solid particles in turbulent channel flow," J. Fluid Mech. **428**, 149–169 (2001).
[7] C. Marchioli and A. Soldati, "Mechanisms for particle transfer and segregation in a turbulent boundary layer," J. Fluid Mech. **468**, 283–315 (2002).
[8] W. C. Reade and L. R. Collins, "Effect of preferential concentration on turbulent collision rates," Phys. Fluids **12**, 2530–2540 (2000).
[9] G. Falkovich, A. Fouxon, and M. G. Stepanov, "Acceleration of rain initiation by cloud turbulence," Nature (London) **419**, 151–154 (2002).
[10] C. A. Ho and M. Sommerfeld, "Modelling of micro-particle agglomeration in turbulent flows," Chem. Eng. Sci. **57**, 3073–3084 (2002).
[11] C. Marchioli, M. Picciotto, and A. Soldati, "Influence of gravity and lift on particle velocity statistics and transfer rates in turbulent vertical channel flow," Int. J. Multiphase Flow **33**, 227–251 (2007).
[12] W. S. J. Uijttewaal and R. V. A. Oliemans, "Particle dispersion and deposition in direct numerical and large eddy simulations of vertical pipe flows," Phys. Fluids **8**, 2590–2604 (1996).

[13] H. Zhang and G. Ahmadi, "Aerosol particle transport and deposition in vertical and horizontal turbulent duct flows," J. Fluid Mech. **406**, 55–80 (2000).
[14] R. Monchaux, M. Bourgoin, and A. Cartellier, "Analyzing preferential concentration and clustering of inertial particles in turbulence," Int. J. Multiphase Flow **40**, 1–18 (2012).
[15] R. Monchaux, M. Bourgoin, and A. Cartellier, "Preferential concentration of heavy particles: A Voronoï analysis," Phys. Fluids **22**, 103304 (2010).
[16] Y. Tagawa, J. M. Mercado, V. N. Prakash, E. Calzavarini, C. Sun, and D. Lohse, "Three-dimensional Lagrangian Voronoï analysis for clustering of particles and bubbles in turbulence," J. Fluid Mech. **693**, 201–215 (2012).
[17] Y. Tagawa, I. Roghair, V. N. Prakash, M. van Sint Annaland, H. Kuipers, C. Sun, and D. Lohse, "The clustering morphology of freely rising deformable bubbles," J. Fluid Mech. **721**, R2 (2013).
[18] R. Monchaux, "Measuring concentration with Voronoï diagrams: the study of possible biases," New J. Phys. **14**, 095013 (2012).
[19] M. García-Villalba, A. G. Kidanemariam, and M. Uhlmann, "DNS of vertical plane channel flow with finite-size particles: Voronoï analysis, acceleration statistics and particle-conditioned averaging," Int. J. Multiphase Flow **46**, 54–74 (2012).
[20] K. M. O. Håkansson, M. Kvick, F. Lundell, L. P. Wittberg, and L. D. Söderberg, "Measurement of width and intensity of particle streaks in turbulent flows," Exp. Fluids **54**, 1555 (2013).
[21] C. Marchioli, A. Soldati, J. G. M. Kuerten, B. Arcen, A. Tanière, G. Goldensoph, K. D. Squires, M. F. Cargnelutti, and L. M. Portela, "Statistics of particle dispersion in direct numerical simulations of wall-bounded turbulence: Results of an international collaborative benchmark test," Int. J. Multiphase Flow **34**, 879–893 (2008).
[22] L. H. Zhao, C. Marchioli, and H. I. Andersson, "Stokes number effects on particle slip velocity in wall-bounded turbulence and implications for dispersion models," Phys. Fluids **24**, 021705 (2012).
[23] H. Abe, H. Kawamura, and Y. Matsuo, "Direct numerical simulation of a fully developed turbulent channel flow with respect to Reynolds number dependence," ASME J. Fluids Eng. **123**, 382–393 (2001).
[24] H. Abe, R. A. Antonia, and H. Kawamura, "Correlation between small-scale velocity and scalar fluctuations in a turbulent channel flow," J. Fluid Mech. **627**, 1–32 (2009).
[25] J. J. J. Gillissen, B. J. Boersma, P. H. Mortensen, and H. I. Andersson, "On the performance of the moment approximation for the numerical computation of fiber stress in turbulent channel flow," Phys. Fluids **19**, 035102 (2007).
[26] L. Schiller and A. Z. Naumann, "Über die grundlegenden Berechnungen bei der Schwerkraftaufereitung," Z. Ver. Dtsch. Ing. **77**, 318–320 (1933).
[27] M. Caporaloni, F. Tampieri, F. Trombetti, and O. Vittori, "Transfer of particles in nonisotropic air turbulence," J. Atmos. Sci. **32**, 565–568 (1975).
[28] M. W. Reeks, "The transport of discrete particles in inhomogeneous turbulence," J. Aerosol Sci. **14**, 729–739 (1983).
[29] J. M. Wallace, H. Eckelmann, and R. S. Brodkey, "The wall region in turbulent shear flow," J. Fluid Mech. **54**, 39–48 (1972).
[30] J. S. Ferenc and Z. Néda, "On the size distribution of Poisson Voronoï cells," Physica A **385**, 518–526 (2007).
[31] L.-P. Wang and M. R. Maxey, "Settling velocity and concentration distribution of heavy particles in homogeneous isotropic turbulence," J. Fluid Mech. **256**, 27–68 (1993).
[32] M. Wilkinson and B. Mehlig, "Caustics in turbulent aerosols," Europhys. Lett. **71**, 186–192 (2005).
[33] K. Duncan, B. Mehlig, S. Östlund, and M. Wilkinson, "Clustering by mixing flows," Phys. Rev. Lett. **95**, 240602 (2005).

Chapter 10

Article 4: Mechanisms of particle clustering in Gaussian and non-Gaussian synthetic turbulence

Under consideration for publication in Physical Review E

Mechanisms of particle clustering in Gaussian and non-Gaussian synthetic turbulence

Christopher Nilsen* and Helge I. Andersson
Department of Energy and Process Engineering,
Norwegian University of Science and Technology, N-7491 Trondheim, Norway
(Dated: 12th August 2014)

We use synthetic turbulence simulations to study how inertial particles cluster in a turbulent flow, for a wide range of Stokes numbers. Two different types of synthetic turbulence are used: one Gaussian, where the time evolution of the velocity field is a simple phase shift, and one non-Gaussian, where convection is used to evolve the velocity field in time. In both flow types we observe significant particle clustering over a wide range of scales and Stokes numbers. The clustering found at low Stokes numbers can be attributed to the vortex centrifuge effect, where heavy particles are expelled from regions dominated by vorticity. This mechanism is much more effective in the non-Gaussian turbulence, because local flow structures are convected with the particles. The preferential sampling of regions with low vorticity, is almost negligible in the Gaussian turbulence. At higher Stokes numbers, caustics are formed in a very similar manner in both Gaussian and non-Gaussian synthetic turbulence. In non-Gaussian turbulence, heavy particles cluster in regions of low fluid kinetic energy, while the opposite is true in Gaussian turbulence. Our results show that synthetic simulations cannot correctly predict how the particle clustering correlates with local fluid flow properties, without including convection.

I. INTRODUCTION

We study the motion of N inertial spherical particles in a domain Ω. The particles are characterised by their position vectors $\boldsymbol{X}_i \in \mathbb{R}^3,\ i = 1, \ldots, N$ and velocity vectors $\boldsymbol{V}_i$. The probability of finding a randomly chosen particle at time t inside $\Phi \subset \Omega$, is $\int_\Phi f(\boldsymbol{x}, t)\, d\boldsymbol{x}$, where f is the probability density function (p.d.f.) for the particle position. If f is the continuous uniform distribution, $f = 1/\int_\Omega d\boldsymbol{x}$, we say that the particles are randomly or uniformly distributed. If not, the particles are clustered in some way. For particles with finite inertia, clustering is the expected condition.

Particle clustering in turbulent flows is often referred to as preferential concentration [1, 2] and the topic has attracted considerable attention since it was first observed that settling particles followed preferential paths [3, 4]. The most common explanation to this phenomenon is that inertial particles are thrown out of vortices as if in a centrifuge, and that this causes heavy particles (particle density greater than the fluid density) to cluster in regions dominated by strain [2]. Light particles will on the other hand cluster in regions dominated by vorticity.

The N particles moving in a turbulent velocity field $\boldsymbol{u}(\boldsymbol{x}, t)$ are all assumed to have sufficiently small radius r to be modelled as point particles. Assuming also that the particle density ρ_p is much greater than the fluid density ρ, the motion of each single particle is governed by the equation

$$\frac{d\boldsymbol{V}}{dt} = \frac{1}{\tau_p}(\boldsymbol{u}(\boldsymbol{X}(t), t) - \boldsymbol{V}(t)), \tag{1}$$

when gravity and Brownian diffusion are neglected. The particle relaxation time $\tau_p = 2r^2\rho_p/(9\rho\nu)$ (where ν is the kinematic viscosity of the fluid) is a measure of how fast the particle is able to adjust to the local fluid velocity. We can define a non-dimensional particle time scale, the Stokes number, as $\mathrm{St} = \tau_p/\tau_f$ where τ_f is a fluid time scale characteristic of the small-scale turbulent motion.

When τ_p is small, the particle velocity can be approximated as $\boldsymbol{V} \approx \boldsymbol{u} - \tau_p \boldsymbol{a}$, which gives a unique Eulerian particle velocity field as a function of the fluid velocity $\boldsymbol{u}$ and the fluid acceleration $\boldsymbol{a} = D\boldsymbol{u}/Dt$. The divergence of this velocity field is then $\nabla \cdot \boldsymbol{V} \approx -\tau_p \nabla \cdot \boldsymbol{a} = 2\tau_p Q$, where $Q = -(1/2)(\partial u_i/\partial x_j)(\partial u_j/\partial x_i)$ is the second invariant of the velocity gradient tensor $\nabla \boldsymbol{u}$ [5]. Q is a measure of the balance between vorticity and shear strain, and that the velocity field contracts ($\nabla \cdot \boldsymbol{V} < 0$) in regions of negative Q, is consistent with the notion that particles cluster in regions dominated by shear [2].

The "centrifuge effect" is an intuitive explanation of why particles with finite but low inertia cluster. It does, however, require the existence of finite-time vortex structures and thus cannot explain the existence of clustering in velocity fields with white noise time dependence [6, 7]. It is possible for strongly inertial particles to detach from the flow and be thrown a significant distance. This causes regions of high particle density, but also significant velocity differences over arbitrarily short distances. These regions of increased particle density do not necessarily correlate with local fluid vorticity, because the fluid structures that caused the effect can be significantly removed in both time and space. Falkovich *et al.* [8] called this the "sling effect", while others have described the mechanism as "caustics" [6, 7, 9]. The

* research@christophernilsen.no

caustics are regions where fast particles have caught up with the slower particles, causing a local increase in particle density.

We will use a synthetic turbulent velocity field $\boldsymbol{u}(\boldsymbol{x}, t)$ in our study of particle clustering. Synthetic turbulence makes it possible to study the motion of millions of particles in a turbulence-like velocity field without having to solve the Navier-Stokes equations. Because the presence of large-scale sweeping of smaller scales is believed to be integral to the dispersion of both fluid particles [10] and solid inertial particles [11], we include two methods for generating synthetic turbulence. The first method is a standard type of kinetic simulation, where large-scale sweeping is absent. The second method retains the convection operator in the Navier-Stokes equations and therefore includes large-scale sweeping. A detailed description of both kinds of synthetic turbulence is given in section II.

We study two different mechanisms causing particle clustering in turbulent flow: the vortex centrifuge effect and caustics. By including two very different types of synthetic turbulence, we can assess the importance of convection in the formation of particle clusters. In section III we measure the amount of clustering to determine at which Stokes numbers and length scales the strongest clustering is observed. In section IV we discuss the vortex centrifuge mechanism and in section V we discuss caustics. Conclusions are drawn in section VI.

II. SYNTHETIC TURBULENCE SIMULATION

Synthetic turbulence simulations [10, 12, 13] are often used as a simple method of generating turbulence-like velocity fields, satisfying the most fundamental requirements of incompressibility and an energy spectrum resembling real turbulence. Particle clustering is studied in two different types of synthetic turbulence, one Gaussian and one non-Gaussian. We use the energy spectrum

$$E(k) = C\epsilon^{2/3}k^{-5/3}\exp(-C_\eta(\eta k)^2) \tag{2}$$

in both synthetic turbulence methods. The wavenumber k is the length of the wavenumber vector $\boldsymbol{k}$ in Fourier space, ϵ is the rate of dissipation, η is the Kolmogorov length scale, and C and C_η are constants. This particular form of the energy spectrum has no energy-containing range and an $\exp(-k^2)$ high wavenumber roll-off, to extend the $k^{-5/3}$ range.

The method involves generating a velocity field $\boldsymbol{u}(\boldsymbol{x})$ on a three-dimensional periodic box with uniform grid with n nodes in each direction. The discrete Fourier transform $\mathcal{F}(\boldsymbol{u}) = \hat{\boldsymbol{u}}(\boldsymbol{k})$ has an energy at each wavenumber $k = |\boldsymbol{k}|$ which can be computed as

$$\mathcal{E}(\hat{\boldsymbol{u}}; k) = \sum_{|\boldsymbol{p}|=k} \hat{\boldsymbol{u}} \cdot \hat{\boldsymbol{u}}^*. \tag{3}$$

Generating a Gaussian synthetic turbulence field involves three simple steps. We first generate a set of random Fourier modes $\hat{\boldsymbol{\zeta}}(\boldsymbol{k})$ on the n^3 grid, satisfying the conjugate symmetry required to make the inverse transform real, and with $(\Re(\hat{\boldsymbol{\zeta}}), \Im(\hat{\boldsymbol{\zeta}})) \sim \mathcal{N}(\boldsymbol{0}, \boldsymbol{1})$. $\mathcal{N}(\boldsymbol{0}, \boldsymbol{1})$ is the multivariate standard normal distribution. The field is then made divergence free by the projection

$$\hat{\boldsymbol{\xi}} = \hat{\boldsymbol{\zeta}} - \frac{\boldsymbol{k} \cdot \hat{\boldsymbol{\zeta}}}{\boldsymbol{k} \cdot \boldsymbol{k}}\boldsymbol{k}, \tag{4}$$

and rescaled to obtain the correct energy spectrum

$$\boldsymbol{u} = \mathcal{F}^{-1}\left[\hat{\boldsymbol{\xi}}\left(\frac{E(k)}{\mathcal{E}(\hat{\boldsymbol{\xi}}; k)}\right)^{1/2}\right], \tag{5}$$

before being transformed to real space. This velocity field is then evolved a time Δt using a simple phase shift

$$\hat{\boldsymbol{u}}(\boldsymbol{k}, t + \Delta t) = \hat{\boldsymbol{u}}(\boldsymbol{k}, t)\exp(\mathrm{i}\omega(k)\Delta t). \tag{6}$$

The time scales associated with large-scale sweeping of smaller scales are Uk [14] and we use $\omega(k) = C_\omega Uk$, to closely match the timescales of real turbulence, even though there is no such sweeping in the phase-shifted synthetic turbulence. C_ω is a constant that determines how fast the velocity field is evolving in time.

Rosales and Meneveau [15, 16] used a pure convection equation to create a multi-scale Lagrangian map. We will also use convection to distort the velocity field. If we wanted to solve the incompressible Navier-Stokes equations, we could use a splitting scheme. Applying a common first-order splitting scheme to the Navier-Stokes equations gives a solution algorithm consisting of three steps: convection

$$\boldsymbol{v} = \boldsymbol{u}(\boldsymbol{x}_d, t), \tag{7}$$

$$\boldsymbol{x}_d = \boldsymbol{x} - \Delta t\boldsymbol{u}\left(\boldsymbol{x} - \frac{\Delta t}{2}\boldsymbol{u}(\boldsymbol{x}, t), t\right), \tag{8}$$

incompressible correction

$$\boldsymbol{w} = \boldsymbol{v} - \frac{\Delta t}{\rho}\nabla p(t + \Delta t) \tag{9}$$

and viscous correction

$$\boldsymbol{u}(t + \Delta t) = \boldsymbol{w} + \nu\Delta t\nabla^2\boldsymbol{u}(t + \Delta t). \tag{10}$$

Here we use a semi-Lagrangian treatment of convection, and $\boldsymbol{x}_d$ is the departure point of a fluid particle arriving at $\boldsymbol{x}$ at time $t + \Delta t$.

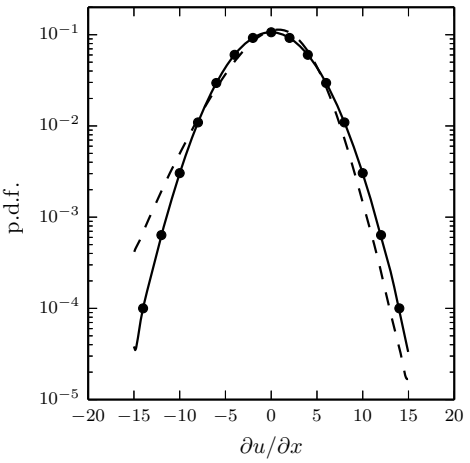

Figure 1. Probability density function of $\partial u/\partial x$ in Gaussian (solid line) and non-Gaussian (dashed line) turbulence. The symbols represent a Gaussian probability distribution.

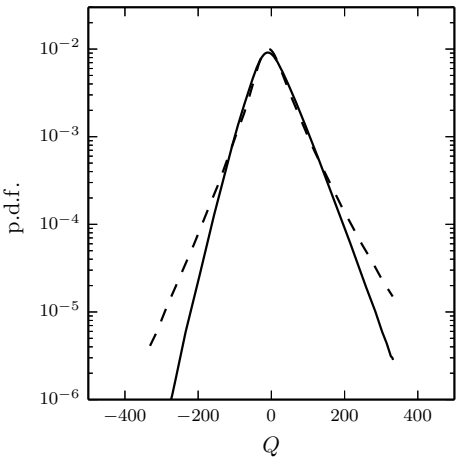

Figure 2. Probability density function of Q in Gaussian (solid line) and non-Gaussian (dashed line) turbulence.

Based on this solution procedure we can create a synthetic turbulence evolution method consisting of three steps: convection

$$\hat{\boldsymbol{v}} = \mathcal{F}(\boldsymbol{u}(\boldsymbol{x}_d, t)), \tag{11}$$

$$\boldsymbol{x}_d = \boldsymbol{x} - \Delta t \boldsymbol{u}\left(\boldsymbol{x} - \frac{\Delta t}{2}\boldsymbol{u}(\boldsymbol{x}, t), t\right), \tag{12}$$

incompressible projection

$$\hat{\boldsymbol{w}} = \hat{\boldsymbol{v}} - \frac{\boldsymbol{k}\cdot\hat{\boldsymbol{v}}}{\boldsymbol{k}\cdot\boldsymbol{k}}\boldsymbol{k} \tag{13}$$

and viscous correction

$$\boldsymbol{u}(t+\Delta t) = \mathcal{F}^{-1}\left[\hat{\boldsymbol{w}}\left(\frac{E(k)}{\mathcal{E}(\hat{\boldsymbol{w}};k)}\right)^{1/2}\right]. \tag{14}$$

We use a Gaussian synthetic turbulence field as the initial condition.

The results in this paper are from two different simulations, one with the Gaussian turbulence and one with the non-Gaussian turbulence. In both cases we use $n = 128$, $C\epsilon^{2/3} = 1$, $C_\eta\eta^2 = 100/k_{\max}^2$ and $\Delta t = 10^{-3}$. The use of $C_\eta\eta^2 = 100/k_{\max}^2$ is very conservative and ensures that accurate fluid velocity interpolation can be achieved without using full Fourier-summation. The time evolution of the Gaussian synthetic turbulence is matched to the non-Gaussian turbulence by choosing $C_\omega U = 47.5$, such that the Taylor time scale $\lambda = 0.033$ in both cases. We use the domain $\Omega = (0,1)\times(0,1)\times(0,1)$.

Before we move on to the particle statistics, we will briefly discuss some fundamental differences between the statistics of the Gaussian and non-Gaussian synthetic turbulence. Simulations of both types of synthetic turbulence are run, starting from the same initial conditions, until the non-Gaussian turbulence has reached a steady state. Afterwards, the statistics are gathered over a total of 10 time units.

Figure 1 shows the probability density function of $\partial u/\partial x$ for both types of synthetic turbulence. We observe that the p.d.f. for the Gaussian synthetic turbulence is Gaussian, as expected. The non-Gaussian turbulence has negative skewness for the $\partial u/\partial x$ p.d.f., which is a well known feature of real turbulence. In addition to this, we see in figure 2 that the non-Gaussian turbulence has a significant widening of the tails of the p.d.f. of Q (the second invariant of $\nabla\boldsymbol{u}$), which means that very large values of strain or vorticity are more likely in the non-Gaussian turbulence. As the value of Q is highly relevant for the distribution of particles (as discussed in the introduction), the differences in the tails of Q are likely to in some way also be reflected in the spatial distribution of particles.

Eulerian time spectra are plotted in figure 3 to compare the temporal evolution of Gaussian and non-Gaussian turbulence. The time spectra are very similar for values of the non-dimensional frequency $\omega\lambda > 10^{-1}$, but with large differences at the lowest frequency. There is significantly more energy in the low-frequency modes in the non-Gaussian turbulence than in the Gaussian turbulence. The difference in low-frequency energy will undoubtedly influence how the particles are transported by the flow, especially when the Stokes number is high.

In these flows, $N = 2\cdot 10^6$ particles with time

4

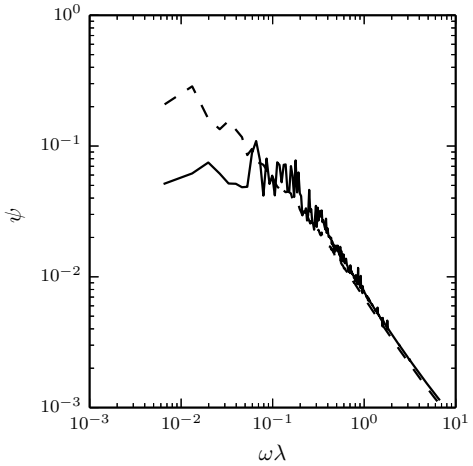

Figure 3. Time spectrum $\psi(\omega)$ ($\int_0^\infty \psi\, d\omega = \frac{1}{2}\boldsymbol{u}\cdot\boldsymbol{u}$) for Gaussian (solid line) and non-Gaussian (dashed line) synthetic turbulence, plotted as function of non-dimensional frequency $\omega\lambda$.

scale τ_p are released and tracked by integrating equation 1 using the standard fourth-order Runge-Kutta method and a time step equal to $2\Delta t$. Third-order polynomial interpolation is used to obtain the fluid velocities at the particle locations. In order to accurately investigate the effect of particle Stokes number $\mathrm{St} = \tau_p/\lambda$, we approximate the τ_p parameter space using high-order polynomials. A total of 15 values of τ_p between 10^{-3} and 0.5 are used, and chosen such that $\log \tau_p^{(j)}$, $j = 1, \ldots, 15$ are Chebyshev nodes transformed using an affine transformation. Fluid tracers are also included for a total of 16 different particle types and $32 \cdot 10^6$ particles.

After a steady state has been reached for the particles, statistics are gathered over a total of 10 time units. We use angular brackets, $\langle\cdot\rangle$, to denote the average of a fluid or particle quantity sampled on the particle paths.

III. PARTICLE DENSITY

To describe the particles' spatial distribution, we approximate the probability density $f(\boldsymbol{x}, t)$. We will use kernel density estimation [17], a non-parametric probability density estimation method with better convergence properties than histograms, and the convenience of providing a smooth functional approximation. The probability density f at position $\boldsymbol{x}$ is approximated as a sum of density kernels using a bandwidth parameter h. The approximate density $\tilde{f}$ for a bandwidth h is

$$\tilde{f}(\boldsymbol{x}; h) = N^{-1}h^{-3}\sum_{i=1}^{N} K((\boldsymbol{x} - \boldsymbol{X}_i)/h), \qquad (15)$$

where $K(\boldsymbol{x})$ is the Gaussian kernel

$$K(\boldsymbol{x}) = (2\pi)^{-3/2}\exp\left(-\frac{1}{2}\boldsymbol{x}\cdot\boldsymbol{x}\right). \qquad (16)$$

There are many different methods for choosing the bandwidth h [17], and with the right choice of bandwidth, the density estimate $\tilde{f}$ should converge to the true density f. Instead of trying to find an optimal bandwidth, we will use a wide range of bandwidth values to see how the particles are clustered at different scales. The density estimate $\tilde{f}(\boldsymbol{x}, h)$ will then approximate the result of applying a Gaussian filter with bandwidth h to the true density.

Kernel density estimation makes it easy to compute the local probability density for each particle, i.e. $\tilde{f}(\boldsymbol{X}_j; h)$ for $j = 1, \ldots, N$. This might seem like a very costly operation to perform, however, since the Gaussian kernel is very close to zero outside $5h$, we only need to include the contribution from particles closer than $5h$ and an $\mathcal{O}(N \log N)$ divide-and-conquer [18] algorithm can be used. The divide-and-conquer algorithm also allows for a natural implementation of the periodic boundary conditions, that are necessary to ensure that $\int_\Omega \tilde{f}\, dx = 1$.

We can measure the extent to which the particles are clustered by comparing $\tilde{f}$ to a uniform particle distribution. If f is a uniform distribution then we expect the density estimate $\tilde{f}$ to follow

$$h^3\langle\tilde{f}\rangle - (2\pi)^{-3/2}N^{-1} = h^3, \qquad (17)$$

which means that

$$\phi(h) = (h^3\langle\tilde{f}\rangle - (2\pi)^{-3/2}N^{-1})^{1/3} - h, \qquad (18)$$

can be used to measure the degree of clustering. This measure is almost identical to the one based on the well-known Ripley's K-function [19], with the exception that we are using a smooth Gaussian kernel to estimate the density. Using different values of h, one can get a good impression of how the particles cluster at different scales.

Figure 4 shows a St-h contour plot of ϕ which allows us to determine at which Stokes numbers and at which scales the particle clustering is most prominent. We observe particle clustering over a wide range of scales and Stokes numbers, in both types of synthetic turbulence The maximum clustering is found for Stokes numbers around unity and at length scales around 10^{-2}. Significant clustering is found at very small scales ($h < 10^{-3}$) for particles with Stokes numbers around $10^{-0.5} \approx 0.3$, and very large scales ($h > 10^{-1}$) for particles with Stokes numbers greater than 10^1. The most noticeable difference between Gaussian and non-Gaussian turbulence is that the clustering is generally stronger for the non-Gaussian turbulence.

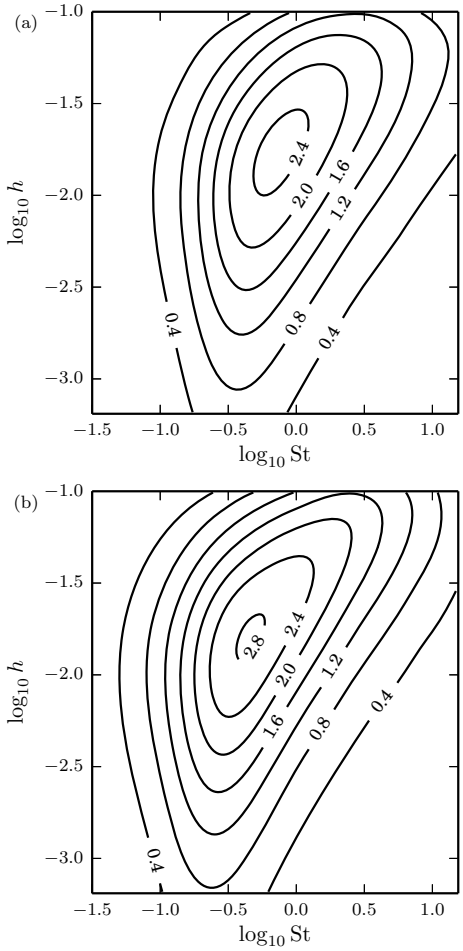

Figure 4. Degree of particle clustering measured using 1000ϕ for (a) Gaussian synthetic turbulence and (b) non-Gaussian synthetic turbulence.

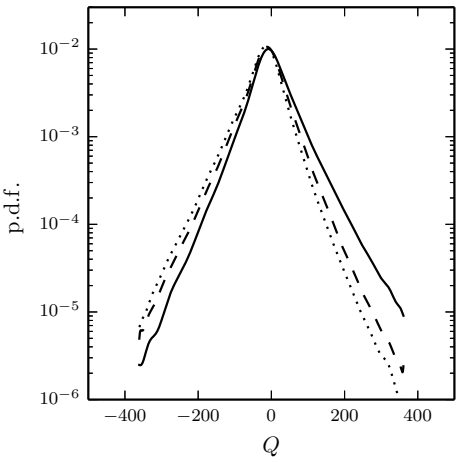

Figure 5. Probability density function of Q in non-Gaussian synthetic turbulence sampled on the particle paths for fluid tracer particles (solid line), particles with St = 0.067 (dashed line) and particles with St = 0.19 (dotted line).

IV. LOW STOKES NUMBER CLUSTERING

We established in section III that clustering is a phenomenon that occurs over a wide range of scales and Stokes numbers. We will now explore some of the mechanisms behind this multiscale phenomenon, starting with how clustering occurs for particles with finite but small Stokes numbers.

We showed in section I, that the divergence of the particle velocity field can (assuming a unique field can be constructed) be approximated as $\nabla \cdot \boldsymbol{V} \approx 2\tau_p Q$. This suggests that the particles will concentrate in regions of negative Q. By studying probability density functions of Q sampled on the particle locations, we can determine if this is observed in the simulations. In figure 5, p.d.f.'s of Q are compared for three different particle types in non-Gaussian synthetic turbulence. It is clear that particles with low Stokes numbers are more likely to be found in regions of negative Q, as predicted by the perturbation approximation.

We use the skewness S_Q of the particle sampled p.d.f. of Q to measure the extent to which particles are clustered in regions of negative Q. A comparison of skewness in Gaussian and non-Gaussian turbulence is shown in figure 6 for all the simulated Stokes numbers. There is clearly a tendency for the particles to cluster in regions of negative Q, and the effect is strongest for St ≈ 0.2, in both types of turbulence. Thus a mechanism where particles are ejected from regions of positive Q, where vorticity is dominant, explains the small-scale clustering observed for low Stokes numbers in figure 4. The same mechanism cannot explain the clustering observed for large St, where S_Q is very close to the value obtained for tracers.

While the particles show an attraction to regions of negative Q in both Gaussian and non-Gaussian synthetic turbulence, the effect is far more pronounced in non-Gaussian turbulence, as seen from the negative values of S_Q in figure 6. The variation in S_Q in Gaussian turbulence is very small compared to what is found in the non-Gaussian turbulence. For Stokes numbers around 0.2, close to 70% of the particles reside in regions with $Q < 0$, in the non-Gaussian turbulence, while the number is no more than 56%, in the Gaussian turbulence. In both cases, roughly 54% of the tracer particles are in regions with $Q < 0$.

6

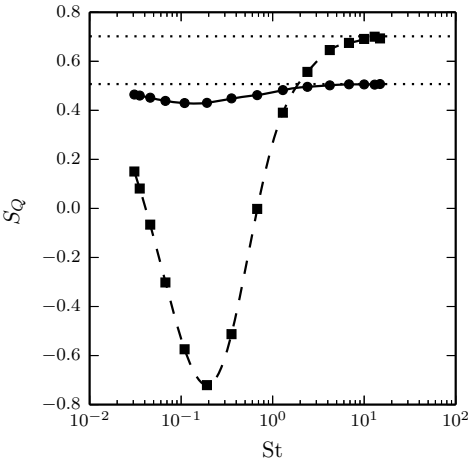

Figure 6. Skewness of p.d.f. for Q sampled on particle paths for Gaussian synthetic turbulence (solid line, circles) and non-Gaussian synthetic turbulence (dashed line, squares). The symbols mark the simulated values, and the lines are interpolants. Horizontal dotted lines mark the skewness of Q for fluid tracers in Gaussian (lower line) and non-Gaussian (upper line) turbulence.

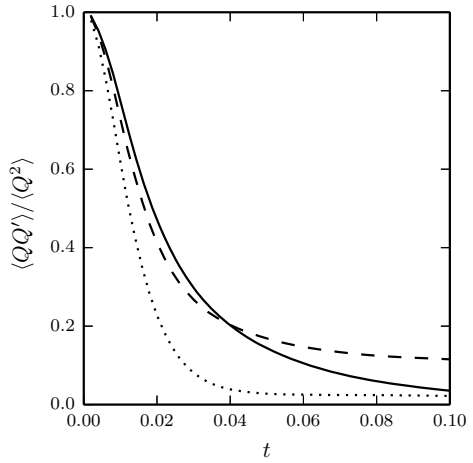

Figure 7. Lagrangian autocorrelation of Q along particle trajectories for fluid tracers (sold line), particles with St = 0.11 (dashed line) and St = 1.3 (dotted line), in non-Gaussian synthetic turbulence.

It is possible that the increased probability of very high or very low values of Q, as observed in figure 2, is part of the reason why particles in non-Gaussian turbulence exhibit a much stronger preferential sampling of low-Q regions. The main reason, however, is most likely the time the particles have to adjust to the local fluid flow structures.

The Lagrangian autocorrelation of Q along particle trajectories will reveal how long the flow structures remain correlated along the particle trajectories. This tells us how long time the particles have to adjust to the local Q. We define the Lagrangian autocovariance of Q along particle trajectories as $\langle Q(\boldsymbol{X}(t_0), t_0) Q(\boldsymbol{X}(t_0 + t), t_0 + t) \rangle = \langle QQ' \rangle$, and the autocorrelation as $\langle QQ' \rangle / \langle Q^2 \rangle$. The autocorrelation is plotted in figure 7 for three different particle types in non-Gaussian synthetic turbulence. As the Stokes number is increased, the autocorrelation is seen to fall more rapidly towards zero, but never quite reaching zero. Because of the preferential concentration of the particles, Q remains correlated even as $t \to \infty$ for moderate Stokes numbers.

From the Lagrangian autocorrelation we can define a Lagrangian integral time scale as $\int_0^\infty \langle QQ' \rangle / \langle Q^2 \rangle \, dt$. This definition would in our case lead to infinite values because $\langle QQ' \rangle / \langle Q^2 \rangle$ does not go to zero as $t \to \infty$. We therefore instead define the Lagrangian integral time scale for Q as

$$\mathcal{T}_Q = \int_0^\infty \frac{\langle QQ' \rangle - \langle QQ' \rangle_\infty}{\langle Q^2 \rangle - \langle QQ' \rangle_\infty} \, dt \,, \qquad (19)$$

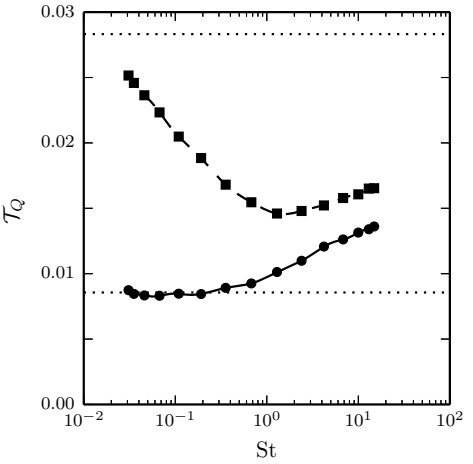

Figure 8. Lagrangian integral time scale for Q along particle trajectories in Gaussian (solid line, circles) and non-Gaussian (dashed line, squares) synthetic turbulence. The horizontal (dotted) lines represent the integral time scales for fluid tracers in Gaussian (lower line) and non-Gaussian (upper line) turbulence.

which is computed using values at $t = 0.5$ to approximate $t \to \infty$. The integral time scale is plotted in figure 8 in both Gaussian and non-Gaussian turbulence. Not only are the numerical values of $\mathcal{T}_Q$ different, the Stokes number dependence is also very different.

In the non-Gaussian turbulence, both the particles

and the fluid structures are convected by the velocity field. This means that particles with low inertia will tend to stay together with certain fluid structures as they are swept through the flow. The longest correlation time is seen for particles exactly following the flow, i.e. the fluid tracers. As the Stokes number increases, the particle trajectories will deviate from the fluid tracer trajectories and $\mathcal{T}_Q$ is reduced. This reduction is seen for low St in figure 8.

In the Gaussian turbulence, there is no convection of fluid structures, and Q is no more correlated along particle tracers, than in any other direction. Thus the integral time scale $\mathcal{T}_Q$ along fluid tracers, is much smaller than in the non-Gaussian turbulence. $\mathcal{T}_Q$ remains close to constant up to St ≈ 1, unlike what is observed for non-Gaussian turbulence.

In both types of turbulence, we see an increase in $\mathcal{T}_Q$ at Stokes numbers greater than unity, where there is very little preferential concentration in regions of low Q (as seen in figure 6). A possible explanation for this is that as the particles get heavier, they get increasingly stationary and $\mathcal{T}_Q$ will be more and more like an Eulerian time scale.

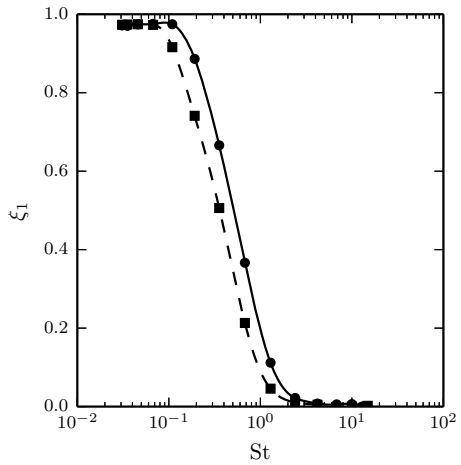

Figure 9. Power-law exponent of first order particle velocity structure function in the dissipative range, in Gaussian (solid line, circles) and non-Gaussian (dashed line, squares) synthetic turbulence.

V. HIGH STOKES NUMBER CLUSTERING

In section IV we defined an integral time scale from the Lagrangian autocorrelation of Q along particle trajectories. The integral time scale for the fluid velocity, is $\mathcal{T}(\boldsymbol{u}) = \int_0^\infty \langle \boldsymbol{u} \cdot \boldsymbol{u}' \rangle / \langle \boldsymbol{u} \cdot \boldsymbol{u} \rangle \, dt$; and for the particle velocity, the integral scale is $\mathcal{T}(\boldsymbol{V}) = \int_0^\infty \langle \boldsymbol{V} \cdot \boldsymbol{V}' \rangle / \langle \boldsymbol{V} \cdot \boldsymbol{V} \rangle \, dt$. At low Stokes numbers, the particles follow the flow almost like tracers and $\mathcal{T}(\boldsymbol{V}) \approx \mathcal{T}(\boldsymbol{u})$. At very high Stokes numbers, the particles move ballistically and $\mathcal{T}(\boldsymbol{V}) \approx \tau_p \gg \mathcal{T}(\boldsymbol{u})$. Plots of $\boldsymbol{V} \cdot \boldsymbol{V}$ (not shown) reveal that particle velocities decrease as $\sqrt{\boldsymbol{V} \cdot \boldsymbol{V}} \sim \mathrm{St}^{-1/2}$, as shown by Abrahamson [20]. This implies that at large Stokes numbers, particles can travel distances proportional to $\mathrm{St}^{1/2}$, while retaining their velocity.

When particles can travel significant distances in the flow without adjusting to the local velocity field, fast particles are overtaking slower particles and forming caustics. Caustics formation is characterised by the existence of relatively large particle velocity differences over short distances, and we can use structure functions to identify this. We use the longitudinal particle velocity structure function of order p, which is defined as

$$S_p(r) = \langle [(\boldsymbol{V}(\boldsymbol{x}+\boldsymbol{r}) - \boldsymbol{V}(\boldsymbol{x})) \cdot \boldsymbol{r}/r]^p \rangle = \langle [\Delta V(r)]^p \rangle. \quad (20)$$

Plots of $S_p(r)$ (not shown) reveal power laws $S_p(r) \sim r^{\xi_p}$ in the dissipative range, i.e. for low values of r. For a smooth velocity field we expect to find $\xi_p = p$. The first order exponent ξ_1 is plotted in figure 9 for the full range of Stokes numbers. At the lowest Stokes numbers we get $\xi_1 \approx 1$, indicative of a smooth velocity field. The value of ξ_1 then decreases smoothly for Stokes numbers around unity to $\xi_1 \approx 0$ at the highest Stokes numbers. In this ballistic range of St, the average velocity difference between two particles is almost independent of the distance between them, for separations in the dissipative range. The Stokes number dependence of ξ_1 seen in figure 9 is very similar to what was observed by Bec *et al.* [21] in direct numerical simulations of homogeneous isotropic turbulence. The only discernible difference between Gaussian and non-Gaussian turbulence in figure 9, is a slightly earlier transition to the ballistic behaviour in non-Gaussian turbulence.

In figure 10 we also include higher order structure functions ($p = 1, 2, 3$) for non-Gaussian turbulence. A similar figure for the Gaussian turbulence (not shown) looks almost identical and any comments made about figure 10 will also apply in Gaussian turbulence. Again we see $\xi_p \approx p$ for the lowest Stokes numbers (St < 0.1), $\xi_p \approx 0$ for the highest Stokes numbers (St > 1.0) and a relatively sharp transition region in the middle.

The curves for ξ_2 and ξ_3 overlap almost completely for St > 0.1 indicating saturation to an exponent ξ_∞. All three curves overlap for St > 0.2, which shows that the saturation occurs at orders lower than 1, as seen by Bec *et al.* [21]. It was also suggested by Bec *et al.* [21] that $\xi_\infty(\mathrm{St})$ should follow a logarithmic function in a certain range of St. In figure 10, it does seem like ξ_∞ could follow a logarithmic function for $0.2 <$ St < 1, but the low number of Stokes numbers in this

8

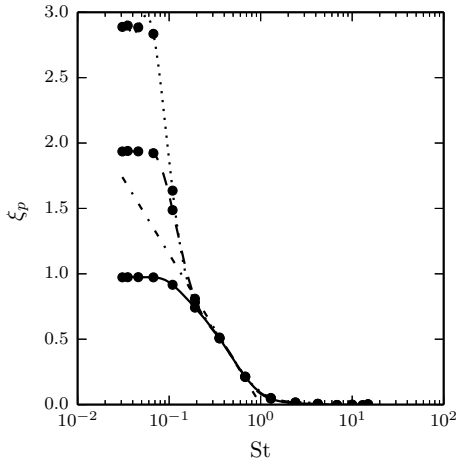

Figure 10. Power-law exponent ξ_p of particle velocity structure function in the dissipative range, for $p = 1$ (solid line), $p = 2$ (dashed line) and $p = 3$ (dotted line) in non-Gaussian turbulence. Dash-dot line is $-0.5 \log \mathrm{St}$.

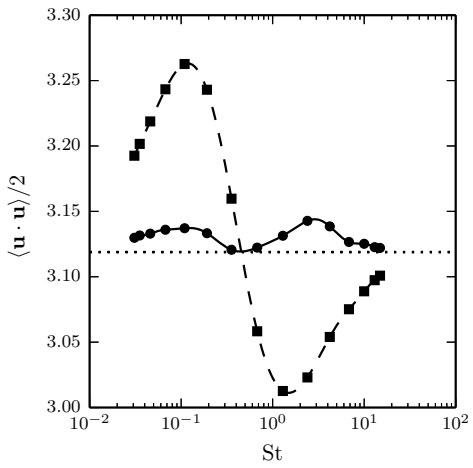

Figure 11. Average fluid kinetic energy sampled on the particle paths, for Gaussian (solid line, circles) and non-Gaussian (dashed line, squares) turbulence. The horizontal dotted line marks the kinetic energy sampled for fluid tracers.

range makes this highly speculative.

In figure 11, we plot the average particle-sampled fluid kinetic energy $\langle \boldsymbol{u} \cdot \boldsymbol{u} \rangle / 2$. At low Stokes numbers, particles preferentially sample regions of high kinetic energy. This effect is maximised around the values of St, where sampling of negative Q is maximised. At higher Stokes numbers, the particles in non-

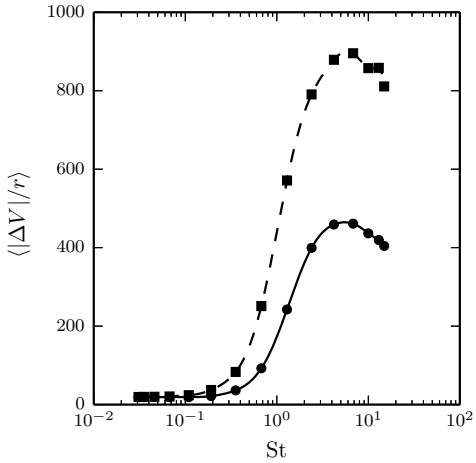

Figure 12. Average velocity gradient $\langle |\Delta V| / r \rangle$ for $r < 10^{-3}$ in Gaussian (solid line, circles) and non-Gaussian (dashed line, squares) synthetic turbulence.

Gaussian turbulence start to preferentially sample regions of low kinetic energy, while the particles in Gaussian turbulence always preferentially sample regions of high kinetic energy. In non-Gaussian turbulence, the transition occurs around the same Stokes numbers where caustics start to emerge. This suggests that caustics cause clustering in low energy regions in non-Gaussian turbulence, and high energy regions in Gaussian turbulence.

We have seen that caustics create a highly intermittent particle velocity field for both Gaussian and non-Gaussian turbulence, with structure function scaling exponents saturating at low orders. However, we also know that the average particle velocity should decrease as the Stokes number increases, and therefore that in the limit $\mathrm{St} \to \infty$ the particles will not move at all. From this it is reasonable to infer that the maximum possible dissipation range velocity differences, are found at some intermediate Stokes number. To test this, we use the average velocity gradient $\langle |\Delta V| / r \rangle$, where ΔV is the longitudinal velocity difference.

Figure 12 illustrates how the short range velocity differences depend on the Stokes number. At the lowest Stokes numbers $\langle |\Delta V| \rangle \sim r$ and $\langle |\Delta V| / r \rangle$ approaches a constant value. As the Stokes number is increased, caustics form and very high values of the velocity gradient become possible. Due to the decrease in particle kinetic energy as $\mathrm{St} \to \infty$, the average close range velocity gradient takes its maximum value at $\mathrm{St} \approx 5$ in both the Gaussian and non-Gaussian turbulence.

Substantially larger values of the gradient $\langle |\Delta V| / r \rangle$ are found in non-Gaussian turbulence than in Gaus-

sian turbulence. The intermittency of the non-Gaussian turbulence itself is likely part of the explanation for the differences observed. It is also likely that the convective mechanism included in the non-Gaussian turbulence, is much more efficient at sweeping heavy particles along to form caustics.

VI. CONCLUSION

A comparison of the clustering of inertial particles in a phase-shifted Gaussian synthetic turbulence and a convected non-Gaussian synthetic turbulence, reveals many similarities and some important differences. In both types of turbulence, we find clustering over a wide range of scales and Stokes numbers, with the maximum clustering found at intermediate scales and Stokes numbers of order unity.

We use Q, the second invariant of $\nabla \boldsymbol{u}$, sampled on the particle locations, to study the extent to which particles concentrate in regions of low vorticity. In both Gaussian and non-Gaussian turbulence there is a tendency for the particles to gather in regions of low Q, although this tendency is much more pronounced in non-Gaussian turbulence. At most, close to 70% of the particles in non-Gaussian turbulence, reside in regions where $Q < 0$. In Gaussian turbulence, this number is less than 56%. It is shown that the sweeping of fluid structures in non-Gaussian turbulence, gives the local fluid vortical structures much more time to throw out the particles. This vortex ejection mechanism is most effective at $\mathrm{St} \approx 0.2$.

The formation of caustics causes large particle velocity differences at short distances, which we observe for Stokes numbers greater than unity in both types of turbulence. Structure function scaling exponents in the dissipation range reveal highly intermittent particle velocities, and surprisingly modest differences between Gaussian and non-Gaussian turbulence. The scaling exponents up to order three are not significantly affected by the intermittency in the non-Gaussian velocity field. In non-Gaussian turbulence, the caustics cause preferential sampling of regions of low fluid kinetic energy, while the opposite is true in Gaussian turbulence. In both types of turbulence, the average dissipation range velocity gradient is maximised for $\mathrm{St} \approx 5$, but the values are higher in non-Gaussian turbulence.

The clustering maps in figure 4 show that maximum clustering occurs when both preferential sampling of low Q and caustics are in effect, for Stokes numbers around unity. These clustering maps are remarkably similar in Gaussian and non-Gaussian turbulence. In both cases we see that the vortex centrifuge effect causes small-scale clustering at low Stokes numbers, and caustics are responsible for creating the, mostly large-scale, clustering at high Stokes numbers. While the extent to which particles are clustered is not very different in the two flows, the preferential sampling of vorticity and kinetic energy is crucially dependent on convection. It is important to include convection in the flow, in order to be able to predict how the particle clustering correlates with local flow properties.

ACKNOWLEDGMENTS

We gratefully acknowledge financial support from COST Action FP1005, for the first author to attend the COST training school “Non-spherical particles and aggregates in fluid flows”.

[1] K. D. Squires and J. K. Eaton, Phys. Fluids A **3**, 1169 (1991).
[2] J. K. Eaton and J. R. Fessler, Int. J. Multiphase Flow **20**, 169 (1994).
[3] M. R. Maxey and S. Corrsin, J. Atmos. Sci. **43**, 1112 (1986).
[4] M. R. Maxey, J. Fluid Mech. **174**, 441 (1987).
[5] H. M. Blackburn, N. N. Mansour, and B. J. Cantwell, J. Fluid Mech. **310**, 269 (1996).
[6] M. Wilkinson and B. Mehlig, Europhys. Lett. **71**, 186 (2005).
[7] K. Duncan, B. Mehlig, S. Östlund, and M. Wilkinson, Phys. Rev. Lett. **95**, 240602 (2005).
[8] G. Falkovich, A. Fouxon, and M. G. Stepanov, Nature **419**, 151 (2002).
[9] K. Gustavsson, E. Meneguz, M. Reeks, and B. Mehlig, New J. Phys. **14**, 115017 (2012).
[10] D. J. Thomson and B. J. Devenish, J. Fluid Mech. **526**, 277 (2005).
[11] L. Chen, S. Goto, and J. C. Vassilicos, J. Fluid Mech. **553**, 143 (2006).
[12] J. C. H. Fung, J. C. R. Hunt, N. A. Malik, and R. J. Perkins, J. Fluid Mech. **236**, 281 (1992).
[13] D. R. Osborne, J. C. Vassilicos, K. Sung, and J. D. Haigh, Phys. Rev. E **74**, 036309.
[14] H. Tennekes, J. Fluid Mech. **67**, 561 (1975).
[15] C. Rosales and C. Meneveau, Phys. Fluids **18**, 075104 (2006).
[16] C. Rosales and C. Meneveau, Phys. Rev. E **78**, 016313 (2008).
[17] M. P. Wand and M. C. Jones, *Kernel Smoothing* (Chapman & Hall, London, 1995).
[18] J. L. Bentley, Comm. ACM **23**, 214 (1980).
[19] B. D. Ripley, J. Appl. Prob. **13**, 255 (1976).
[20] J. Abrahamson, Chem. Eng. Sci. **30**, 1371 (1975).
[21] J. Bec, L. Biferale, M. Cencini, A. S. Lanotte, and F. Toschi, J. Fluid Mech. **624**, 527 (2010).

Chapter 11

Article 5: On wall-normal particle drift and clustering in a turbulent channel flow

Under consideration for publication in Journal of Fluid Mechanics

Under consideration for publication in J. Fluid Mech. 1

On wall-normal particle drift and clustering in a turbulent channel flow

Christopher Nilsen† and Helge I. Andersson

Department of Energy and Process Engineering, Norwegian University of Science and Technology, N-7491 Trondheim, Norway

(Received 12th August 2014)

Preferential concentration of particles in a turbulent channel flow takes two distinct forms: wall-normal particle drift and local clustering. We use direct numerical simulations at shear Reynolds numbers 180 and 395 to study these two effects. The wall-normal particle drift is maximised at viscous Stokes numbers around 20 at both Reynolds numbers, but significantly higher values of the mean wall-normal particle velocity are found at the highest Reynolds number. Instead of a turbulence gradient law, we find that the mean wall-normal particle velocity is almost proportional to the wall-normal fluid RMS velocity, for a wide range of particle Stokes numbers. Local particle clustering is observed over a wide range of scales and Stokes numbers, both in the buffer layer and the centre of the channel. There is strong preferential sampling of low vorticity regions also in the core region, and this effect is maximised for Kolmogorov Stokes numbers around unity. At Kolmogorov Stokes numbers greater than unity we also observe caustics in the centre of the channel. We find strongly intermittent dissipation range structure functions for the particle velocity in the core region.

1. Introduction

If a swarm of inertial particles are released in a turbulent channel flow, they will tend to move towards the walls. This causes large gradients in the particle density close to the wall, and extensive particle deposition even without the assistance of gravity. Caporaloni *et al.* (1975) and later Reeks (1983) described a mechanism causing particles in inhomogeneous turbulence to drift in the direction of negative gradient of the turbulent velocity fluctuations. They referred to this as a "turbophoretic" velocity, due to how the mechanism is reminiscent of thermophoresis. More recently, detailed studies of the wall-normal drift of particles have been performed using direct numerical simulation in both Newtonian (Sardina *et al.* 2012) and non-Newtonian (Nowbahar *et al.* 2013) flows.

This is just one example of what is commonly referred to as preferential concentration (Maxey 1987; Squires & Eaton 1991), which causes particles to prefer to reside in certain regions of the flow. Also in homogeneous turbulence, strongly inhomogenous spatial particle distributions are found (Squires & Eaton 1991), and heavy particles (particles with density greater than the fluid density) accumulate in strain-dominated regions (Eaton & Fessler 1994). The particles preferentially concentrate in regions dominated by strain because they are being thrown out of vortices acting as small centrifuges.

In a turbulent channel flow, however, the non-random spatial distribution of particles was not found to be significantly correlated with the local flow topology by Rouson & Eaton (2001), except in the near-wall region, where the particles preferentially concentrate in the low-speed streaks. Mechanisms explaining the accumulation in low-speed streaks, as well as the strong wall-normal flux of particles, were discussed in detail by Marchioli & Soldati (2002), with special emphasis on the importance of sweeps and ejections.

† Email address for correspondence: research@christophernilsen.no

The "centrifuge mechanism" is most effective at low to moderate Stokes numbers, while there are other mechanisms causing clustering at the highest Stokes numbers. Strongly inertial particles can retain their velocity while traveling significant distances in the flow. This makes it possible for fast particles to overtake slower particles and cause significant velocity differences over arbitrarily small distances. When this happens the particle velocity field "folds over itself", causing regions of increased particle density (Falkovich *et al.* 2002; Wilkinson & Mehlig 2005; Duncan *et al.* 2005; Gustavsson *et al.* 2012). These "folds" in the particle velocity field are referred to as "caustics", and caustic clustering has been identified at Stokes numbers greater than unity in homogeneous isotropic turbulence (Bec *et al.* 2010).

We use direct numerical simulations of turbulent channel flow with suspended spherical particles to investigate preferential concentration. We focus on both the mean wall-normal flux of particles and the formation of local clustering. Experimental or computational studies of particle dispersed turbulent channel flows are often limited to a fairly low number of particle Stokes numbers (usually three to five). This makes it difficult to draw clear conclusions about the effect of particle inertia. A well resolved Stokes number parameter space and a large number of particles, should help us bring more clarity to the specific effect of particle Stokes number. We will also use two different channel flow Reynolds numbers to identify possible Reynolds number effects.

The numerical methods used for performing the simulations and computing particle statistics, are presented in section 2. Results are presented and analysed in section 3, with a focus on wall-normal particle drift in 3.1 and clustering in 3.2. Conclusions are drawn in section 4.

2. Methodology

2.1. *Direct numerical simulation*

We use direct numerical simulations to study the motion of particles in turbulent channel flows. Two different simulations are used, one at friction Reynolds number $\mathrm{Re}_\tau = u_\tau h/\nu = 180$ and one at $\mathrm{Re}_\tau = 395$. Most previous studies of particle clustering in channel flow use $\mathrm{Re}_\tau \leq 180$ (Rouson & Eaton 2001; Marchioli & Soldati 2002; Sardina *et al.* 2012). The wall-normal height of the channel is $2h$, ν is the kinematic viscosity of the fluid and u_τ is the friction velocity, when ρu_τ^2 is the wall stress and ρ is the fluid density. Periodic boundary conditions are used in the streamwise (x) direction and spanwise (z) direction, while no-slip velocity boundary conditions are used in the wall-normal (y) direction. We use a spectral element method to find an approximate solution for the velocity $\boldsymbol{u} = (u, v, w)$ and the pressure p to the incompressible Navier-Stokes equations with constant density and viscosity. The flows are driven by a constant mean streamwise pressure gradient.

The Navier-Stokes equations are solved numerically using a dual splitting scheme similar to the one suggested by Karniadakis *et al.* (1991), but with auxiliary semi-Lagrangian convection treatment (Maday *et al.* 1990). A third-order backwards differentiation method is used for the Stokes operator and a fourth-order Runge-Kutta method is used for the convection operator. Consistent third-order Neumann pressure boundary conditions (Karniadakis *et al.* 1991) are used for a resulting temporal accuracy of order three. This splitting scheme requires the solution of one Poisson equation for the pressure and three Helmholtz equations for the velocity components, in addition to the integration of the convection operator, each time step.

The spatial discretisation uses a Galerkin formulation and is similar to the discretisation presented by Rønquist (1988). A solution is found on a domain Ω which is the union of E smaller deformed hexahedral elements. Within each element the solution is approximated

using a nodal tensor-product basis of one-dimensional Lagrangian interpolants through the $n+1$ Gauss-Lobatto-Legendre nodes. C^0 continuity is enforced on the element boundaries. A small amount of spectral vanishing viscosity is used to stabilise the simulation (Xu & Pasquetti 2004), and the convective form $(\boldsymbol{u} \cdot \nabla \boldsymbol{u})$ of the convection operator is used. The discretised Poisson and Helmholtz equations form symmetric positive definite systems that are solved using the preconditioned conjugate gradient method.

In the simulation at $\mathrm{Re}_\tau = 180$, a domain size of $L_x \times L_y \times L_z = 15h \times 2h \times 7h$ is discretised using $18 \times 8 \times 12$ elements, while the simulation with $\mathrm{Re}_\tau = 395$ uses $12 \times 8 \times 9$ elements and a domain size of $10h \times 2h \times 5h$. The domains are larger than those used by Moser *et al.* (1999) to avoid some of the small-domain effects observed by Sardina *et al.* (2012). The elements are non-uniformly deformed in the wall-normal direction, such that the centres of the elements are positioned on a set of Chebyshev nodes between 0 and $2h$. A polynomial order $n = 17$ is used for $\mathrm{Re}_\tau = 180$ and $n = 30$ is used for $\mathrm{Re}_\tau = 395$. The low Reynolds number simulation use a viscous time step of $\Delta t = 2 \cdot 10^{-4} h/u_\tau$ and two convection time steps per viscous time step, and for the high Reynolds number simulation $\Delta t = 1 \cdot 10^{-4} h/u_\tau$ and three convection steps per viscous step are used.

Large swarms of tiny spherical particles are tracked in the channel flow simulation. These particles are assumed to be so much smaller than the smallest fluid scales that their motion can be accurately approximated using a point-particle approximation. Specifically, we can say that we assume $a^+ = a u_\tau/\nu \ll 1$, when a is the particle radius. The particles do not interact with each other and they do not affect the flow. The N particles follow the particle paths $\boldsymbol{X}_i = (X_i, Y_i, Z_i),\ i = 1, \ldots, N$ with velocities $\boldsymbol{V}_i = (U_i, V_i, W_i),\ i = 1, \ldots, N$. When we also assume that the particle density ρ_p is much greater than the fluid density ρ and that gravitational and Brownian forces are negligible, the equation of motion for a single particle is

$$\frac{d\boldsymbol{V}}{dt} = \frac{1}{\tau_p}(\boldsymbol{u}(\boldsymbol{X}(t), t) - \boldsymbol{V}(t)). \tag{2.1}$$

The particle relaxation time $\tau_p = 2a^2\rho_p/(9\rho\nu)$ is used to define the Stokes number $\mathrm{St} = \tau_p/(\nu/u_\tau^2)$, which measures the particle inertia. No drag-correction or other finite-radius effects are included, and the particles bounce back elastically when they hit the walls ($Y < 0$ or $Y > 2h$). The reason to neglect all finite-radius effects is to make sure that the assumption $a u_\tau/\nu \ll 1$ is consistently applied, and to avoid a two-dimensional parameter space for the particles.

Equation 2.1 is integrated in time using a fourth-order Runge-Kutta method and a time step equal to $2\Delta t$. Fourth order Lagrangian interpolation is used to approximate $\boldsymbol{u}(\boldsymbol{X})$. The particle integration is done in the reference variables internal to each element, and a non-linear iterative method is used to identify the time and location a particle crosses over into another element.

In the $\mathrm{Re}_\tau = 180$ simulation we use $N = 2 \cdot 10^6$ particles for each Stokes number and in the $\mathrm{Re}_\tau = 395$ simulation we use $N = 8 \cdot 10^6$. In both cases we use the 12 different Stokes numbers $\mathrm{St}^{(j)} = 10^{1+\xi_j},\ j = 1, \ldots, 12$, where ξ_j are the Gauss-Lobatto-Legendre nodes. This particular choice of Stokes numbers allows us to approximate the continuous Stokes number space between 1 and 100 using high-order polynomial interpolation. We can also compute a Stokes number $\mathrm{St}_K = \mathrm{St}/\tau_K^+$ based on the centreline Kolmogorov time scale $\tau_K^+ = \tau_K/(\nu/u_\tau^2)$, which is 13.7 for $\mathrm{Re}_\tau = 180$ and 19.6 for $\mathrm{Re}_\tau = 395$. The Kolmogorov time scale is smaller closer to the wall, and a Stokes number based on the local Kolmogorov time scale could be used. Instead, we use the viscous Stokes number St in the near-wall region.

The particles are randomly (uniformly) distributed in the channel after the turbulent channel flow has reached a statistically steady-state condition. After the particles are in-

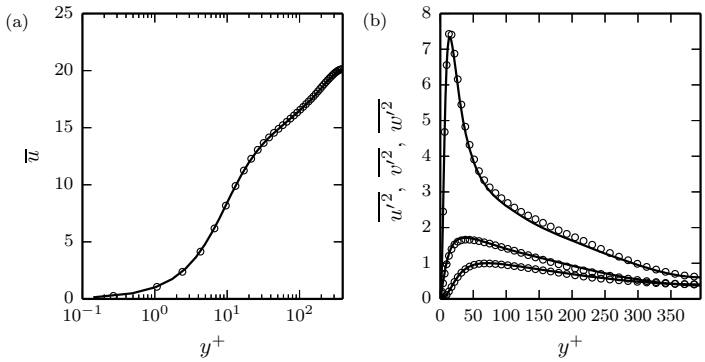

FIGURE 1. Comparison of (a) mean velocity and (b) normal components of Reynolds stress tensor from simulation with $\mathrm{Re}_\tau = 395$ (solid lines) with results by Moser *et al.* (1999) (circles). Curves in (b) are, from top to bottom, $\overline{u'^2}$, $\overline{w'^2}$ and $\overline{v'^2}$. The circles represent values at every third grid-point used by Moser *et al.* (1999), to avoid excessive clutter. Our results are averaged in the two homogeneous directions and over the whole simulation time span.

troduced in the velocity field, the simulations are run from $t = 0$ and until $t = 63.2h/u_\tau = 11376\nu/u_\tau^2$ for $\mathrm{Re}_\tau = 180$, and $t = 22.2h/u_\tau = 8769\nu/u_\tau^2$ for $\mathrm{Re}_\tau = 395$. We will mostly use the non-dimensional time $t^+ = t\nu/u_\tau^2$, when referencing time variation.

As a validation of the Navier-Stokes solution procedure, we compare statistics obtained for the mean streamwise velocity ($\overline{u}$) and normal Reynolds stress components ($\overline{u'^2}$, $\overline{v'^2}$, $\overline{w'^2}$) with results published by Moser *et al.* (1999) at $\mathrm{Re}_\tau = 395$ in figure 1. Our results show good agreement with the results from the reference simulation. Statistics for $\mathrm{Re}_\tau = 180$ (not shown) look similar, but with values slightly closer to the corresponding results of Moser *et al.* (1999).

2.2. *Particle statistics*

If we define a particle probability density function $f(\boldsymbol{x})$, such that the probability of finding a particle inside $\Phi \subset \Omega$ is $\int_\Phi f(\boldsymbol{x})\, d\boldsymbol{x}$ and $\int_\Omega f\, d\boldsymbol{x} = 1$, then the particle density is Nf. We use kernel density estimation (Wand & Jones 1995), which is an efficient non-parametric probability density estimation method, to find an estimate of f.

We know the position vectors $\boldsymbol{X}_i$, $i = 1, \ldots, N$ of the particles and can approximate the true density f with the kernel estimate $\hat{f}$ using

$$\hat{f}(\boldsymbol{x}; \sigma) = N^{-1}\sigma^{-d} \sum_{i=1}^{N} K((\boldsymbol{x} - \boldsymbol{X}_i)/\sigma), \tag{2.2}$$

in d-dimensional space. We use a Gaussian kernel function,

$$K(\boldsymbol{x}) = (2\pi)^{-3/2} \exp\left(-\frac{1}{2}\boldsymbol{x} \cdot \boldsymbol{x}\right), \tag{2.3}$$

and a bandwidth σ. The bandwidth defines the scale of investigation, and we can vary σ to find how the particles are clustered at different scales. Instead of using a three-dimensional density estimate, we use two-dimensional density estimates $\hat{f}_{xz}$ in planes parallel with the walls and a one-dimensional density estimate $\hat{f}_y$ in the wall-normal direction.

Because of the strong density gradients close to the walls, we use a coordinate trans-

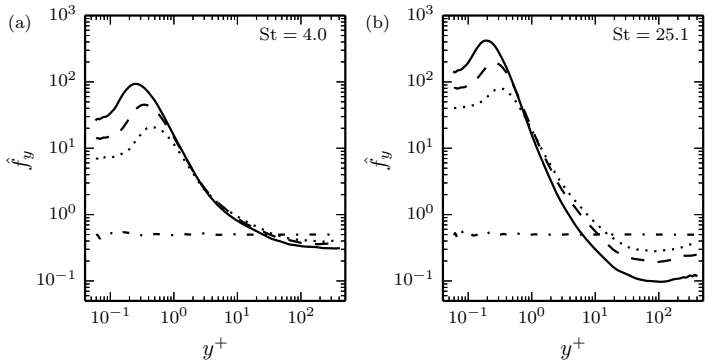

FIGURE 2. Particle probability density in channel flow with $\mathrm{Re}_\tau = 395$ at times $t^+ = 0$ (dash–dotted), 1975 (dotted), 3950 (dashed) and 7900 (solid), for particles with (a) St = 4.0 and (b) St = 25.1.

formation (Wand *et al.* 1991) when finding the one-dimensional density estimate $\hat{f}_y$, i.e.

$$\hat{f}_y(y) = N^{-1}\sigma^{-1}\sum_{i=1}^{N} g'_\lambda(y)K((g_\lambda(y) - g_\lambda(Y_i))/\sigma), \tag{2.4}$$

with

$$g_\lambda(x) = \begin{cases} x^\lambda & x < 1 \\ 2 - (2-x)^\lambda & x > 1 \end{cases}, \tag{2.5}$$

and $\lambda = 0.15$. The mean wall-normal particle velocity is similarly approximated as

$$\langle V \rangle_y(y) = \frac{\sum_{i=1}^{N} V_i g'_\lambda(y)K((g_\lambda(y) - g_\lambda(Y_i))/\sigma)}{\sum_{i=1}^{N} g'_\lambda(y)K((g_\lambda(y) - g_\lambda(Y_i))/\sigma)}. \tag{2.6}$$

3. Results

3.1. *Wall accumulation*

All particles included in the simulations are observed to migrate towards the walls, and accumulate in the near wall region. This, by necessity, causes a depletion of particles in the channel core region. In figure 2, we show the particle probability density $\hat{f}_y$ (the density is symmetric and only half is included), which is an estimate of the probability of finding a randomly chosen particle at wall-normal coordinate y at time t. The large number of particles and the good convergence properties of the kernel density estimation method, make it possible to also study the time variation of $\hat{f}_y$.

For both of the Stokes numbers included in figure 2, the density reaches its maximum value very close to the wall ($y^+ < 1$) and its minimum value around $y^+ \approx 100$. When St = 25.1, the maximum density value is almost four orders of magnitude greater than the minimum density, at time $t^+ = 7900$. The position of maximum density moves closer to the wall as time progresses, and at increasing Stokes numbers. The slow shift of the point of maximum density was also observed by Marchioli & Soldati (2002), and explained to be the result of a two-stage process where particles are first transported to the near-wall region by turbulent motion, and then slowly drift toward the wall. Particle densities in the $\mathrm{Re}_\tau = 180$ simulation are very similar to the ones shown in figure 2.

The value at maximum density $\hat{f}_{y,\max}$ is plotted in figure 3 for the whole range of Stokes numbers, and at both Reynolds numbers. In this and similar figures, the symbols mark

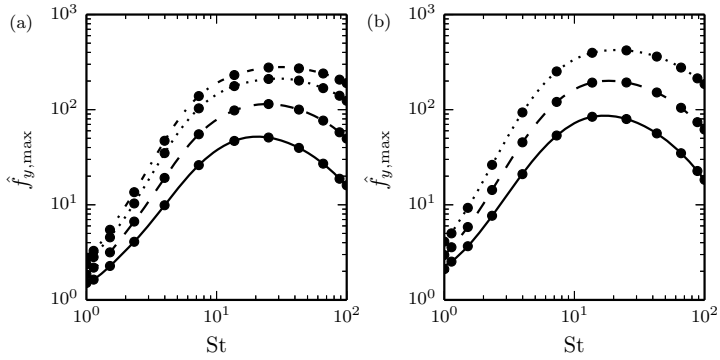

FIGURE 3. Maximum value of particle probability density in channel flow with (a) $\mathrm{Re}_\tau = 180$, at times 1980 (solid), 3960 (dashed), 7920 (dotted) and 11160 (dash-dotted); and with (b) $\mathrm{Re}_\tau = 395$, at times 1975 (solid), 3950 (dashed) and 7900 (dotted).

the actual simulated Stokes numbers and the lines are high-order polynomial interpolants. At both Reynolds numbers the maximum density, and thus the wall accumulation, is maximised for $\mathrm{St} \approx 20$. The shapes of the curves in figure 3 suggest that wall accumulation of particles will be a significant effect also at Stokes numbers much higher than 100.

The increase seen in $\log \hat{f}_{y,\max}$ in figure 3 is close to constant for the successive doublings in t. This suggests that $\hat{f}_{y,\max}$ increases close to linearly with time. Plots of probability density $\hat{f}_y$ as a function of time (not shown) do indeed show that $\hat{f}_y \propto t$ in the near wall region, for the entire time span included in the simulations: $t^+ < 11376$ for $\mathrm{Re}_\tau = 180$ and $t^+ < 8769$ for $\mathrm{Re}_\tau = 395$. There is nothing to suggest that a steady state particle density will be reached anytime soon. Marchioli *et al.* (2008) did find an approximately steady state near-wall particle density, but only after t^+ had reached approximately 20000 and with the help of a finite-radius collision model. It is not certain that a steady state particle distribution, apart from one where all the particles are at the walls, can be reached without a finite-radius collision model.

The accumulation of particles close to the walls is caused by a non-zero mean wall-normal particle velocity $\langle V \rangle_y$, which is plotted in figure 4 for Stokes numbers 4.0 and 25.1 at Reynolds number 395 (same as figure 2). At $\mathrm{St} = 25.1$ the particle velocity does not change much between $t^+ = 1975$ and $t^+ = 7900$, suggesting it is close to steady.

In the turbophoretic drift theory presented by Caporaloni *et al.* (1975), the turbophoretic velocity V_{TF} should be proportional to the gradient of the RMS velocity squared, i.e. $V_{\mathrm{TF}} = -\tau_p d\overline{v'^2}/dy$. Nowbahar *et al.* (2013) showed, using a simple perturbation approximation, that the drift velocity $\langle V \rangle_y$ could be approximated as the sum of the mean particle-sampled fluid velocity $\langle v \rangle_y$ and the turbophoretic drift velocity $-\tau_p d\langle v'^2 \rangle_y/dy$ (now using gradient of particle-sampled RMS velocity), for low values of τ_p. Neither the shape of $\langle V \rangle_y$ in figure 4 nor $\hat{f}_y$ in figure 2, can be explained from a turbulence gradient law. Particle transport towards lower values of turbulence intensity should lead to a net influx of particles to the channel core region, which is not observed.

The mean particle wall-normal velocity $\langle V \rangle_y$ takes its minimum value (maximum absolute value) for y^+ around 50 to 100, which is close to the position of maximum $\overline{v'^2}$ in figure 1. The shape of $\langle V \rangle_y$ seen in figure 4 also suggests that $\langle V \rangle_y$ is closer to being proportional to $\overline{v'^2}$ or $\sqrt{\overline{v'^2}}$, than to the gradient. In figure 5, we plot $\langle V \rangle_y / \langle V \rangle_{y,\min}$

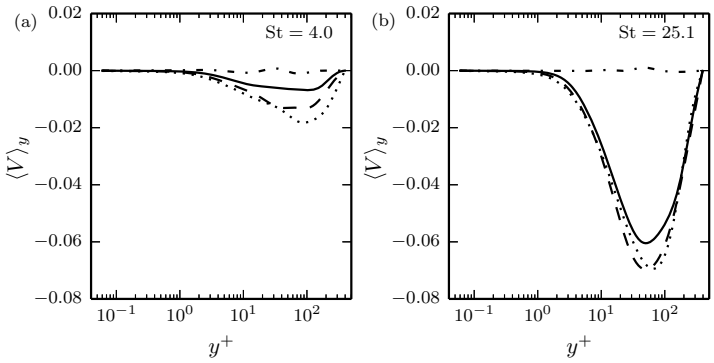

FIGURE 4. Particle mean wall-normal velocity in channel flow with $\mathrm{Re}_\tau = 395$ at times $t^+ = 0$ (dash-dotted), 1975 (dotted), 3950 (dashed) and 7900 (solid), for particles with (a) $\mathrm{St} = 4.0$ and (b) $\mathrm{St} = 25.1$. Each of the particle velocity curves (except for $t^+ = 0$) are averaged over five time samples 39.5 time units apart centred at the specified values of t^+.

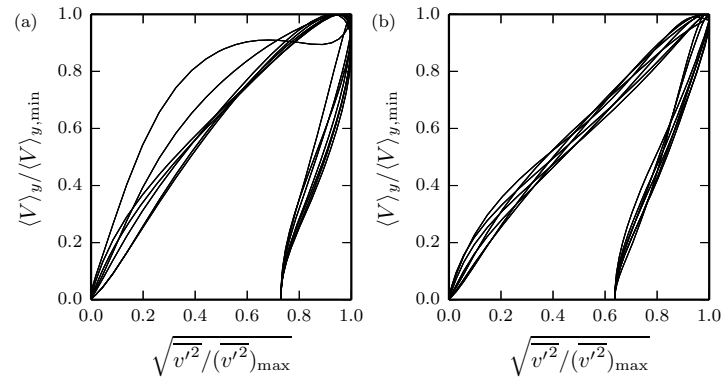

FIGURE 5. Normalised wall-normal particle velocity versus wall-normal fluid RMS velocity for St between 7.3 and 100 for (a) $\mathrm{Re}_\tau = 180$ and $t^+ = 3960$, and (b) $\mathrm{Re}_\tau = 395$ and $t^+ = 3950$.

versus $\sqrt{\overline{v'^2}/(\overline{v'^2})_{\max}}$, at both $\mathrm{Re}_\tau = 180$ and $\mathrm{Re}_\tau = 395$. We see that the particle drift velocity is close to proportional to $-\sqrt{\overline{v'^2}}$ for $y < y_{vm}$ and $\left(\sqrt{(\overline{v'^2})_{\max}} - \sqrt{\overline{v'^2}}\right)$ for $y > y_{vm}$, where y_{vm} is the position of maximum $\overline{v'^2}$. This is particularly true at the highest Reynolds number.

The minimum value of the wall-normal velocity $\langle V \rangle_y$ is plotted in figure 6, showing that the wall-normal particle drift is maximised at $\mathrm{St} \approx 20$ (as suggested in figure 3). The approximate proportionality between $\langle V \rangle_y$ and $-\sqrt{\overline{v'^2}}$ could be used to approximate the evolution of particle density, using only information about fluid statistics. With a Stokes number dependent coefficient, determined from figure 6, it should be possible to obtain reasonable predictions of the particle density.

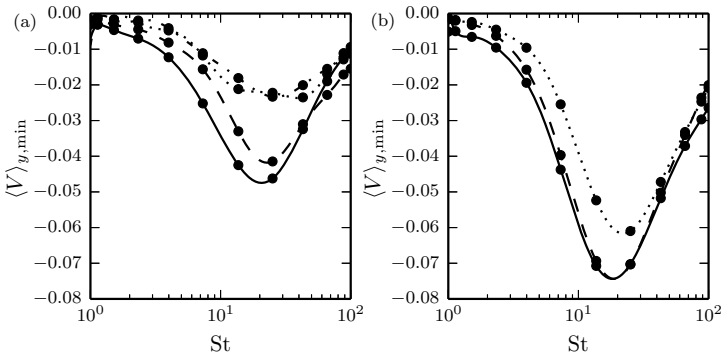

FIGURE 6. Minimum value of wall-normal particle velocity in channel flow with (a) $\mathrm{Re}_\tau = 180$ at times 1980 (solid), 3960 (dashed), 7920 (dotted) and 11160 (dash-dotted); and with (b) $\mathrm{Re}_\tau = 395$, at times 1975 (solid), 3950 (dashed) and 7900 (dotted). Each of the particle velocity curves are averaged over five time samples (a) 36.0 and (b) 39.5 time units apart, centred at the specified values of t^+.

3.2. *Local particle clustering*

In addition to accumulating at the walls, the particles also collect in local clusters. We use the two-dimensional density estimate $\hat{f}_{xz}(\sigma)$ in a plane parallel with the walls, to measure the extent to which particles are clustered at scale σ. If the particles are uniformly distributed in the plane we expect to get

$$L_x L_z(\sigma^2 \langle \hat{f}_{xz} \rangle - (2\pi N)^{-1}) = \sigma^2, \tag{3.1}$$

where $\langle \hat{f}_{xz} \rangle$ denotes the density sampled on the particle locations. The function

$$\phi(h) = [L_x L_z(\sigma^2 \langle \hat{f}_{xz} \rangle - (2\pi N)^{-1})]^{1/2} - \sigma \tag{3.2}$$

is then a measure of how clustered the particles are at scale σ. This clustering measure is similar to Ripley's L-function (Ripley 1976), a well-known measure of spatial homogeneity.

In figures 7 and 8, we plot ϕ as a function of h and St, in planes in the middle of the buffer layer and in the centre of the channel. In both cases we observe significant clustering over a wide range of scales and Stokes numbers. Similar plots at $\mathrm{Re}_\tau = 180$ (not shown) are also produced to determine (St, σ) coordinates of maximum clustering. In the centre of the channel maximum clustering is found for $\mathrm{St} = 18.4$ ($\mathrm{St}_K = 1.3$) and $\sigma^+ = 18.6$ ($\sigma/\eta_K = 5.0$) with a value of $\phi = 0.035$, at $\mathrm{Re}_\tau = 180$; and $\mathrm{St} = 28.8$ ($\mathrm{St}_K = 1.5$) and $\sigma^+ = 29.2$ ($\sigma/\eta_K = 6.6$) with a value of $\phi = 0.024$, at $\mathrm{Re}_\tau = 395$. In the buffer layer maximum clustering is found for $\mathrm{St} = 15.2$ and $\sigma^+ = 20.3$ with a value of $\phi = 0.042$, at $\mathrm{Re}_\tau = 180$; and $\mathrm{St} = 10.9$ and $\sigma^+ = 20.3$ with a value of $\phi = 0.019$, at $\mathrm{Re}_\tau = 395$.

The clustering in the buffer layer occurs at lower values of the Stokes number, most likely because of the smaller fluid time scales in this region of the flow. In the centre of the channel, an increase in Reynolds number shifts the point of maximum clustering towards higher Stokes numbers and larger scales. The most noteworthy Reynolds number effect observed in these numbers, is the clear reduction in ϕ, and therefore clustering, at the higher Reynolds number. This is a little surprising, but is most likely caused by the increased wall-normal particle velocity seen in figure 6. When the particles move faster towards the walls, there is less time to form local clusters.

The most common explanation for particle clustering is that particles are ejected from regions of high vorticity. We use $Q = -(1/2)(\partial u_i/\partial x_j)(\partial u_j/\partial x_i)$, the second invariant of

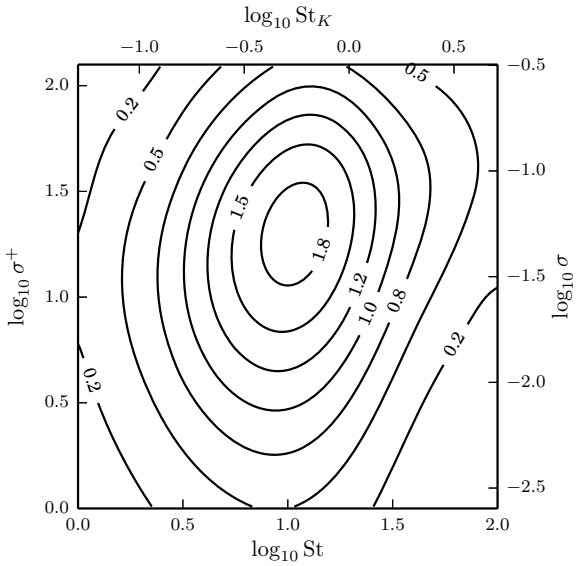

FIGURE 7. Contour plot of clustering function $100\phi(\sigma)$ for particles with wall-normal coordinate $19 < Y^+ < 21$ in channel flow with $\mathrm{Re}_\tau = 395$, averaged between $t^+ = 3950$ and $t^+ = 7900$.

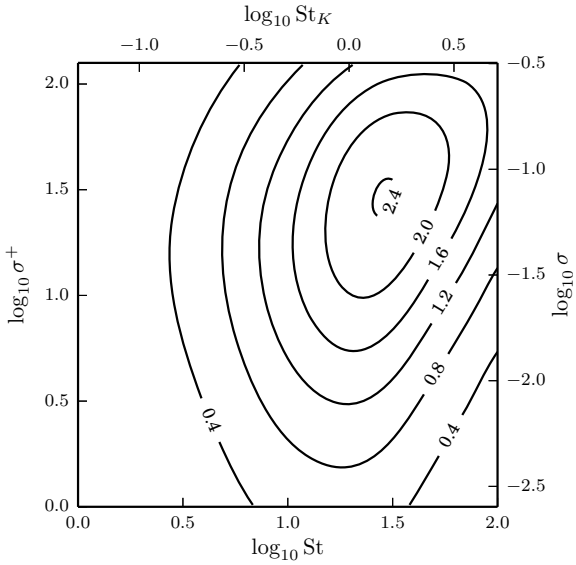

FIGURE 8. Contour plot of clustering function $100\phi(\sigma)$ for particles with wall-normal coordinate $393 < Y^+ < 395$ in channel flow with $\mathrm{Re}_\tau = 395$, averaged between $t^+ = 3950$ and $t^+ = 7900$.

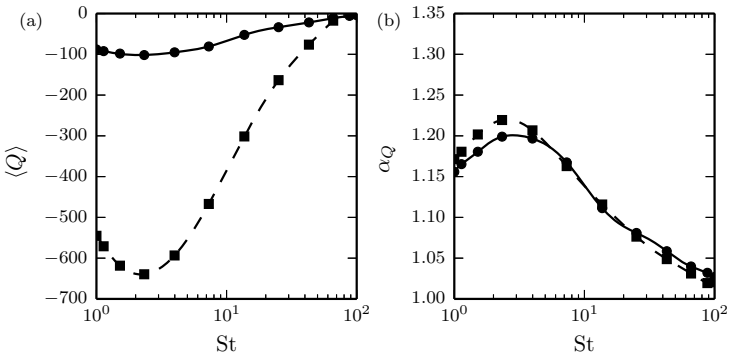

FIGURE 9. (a) Mean particle sampled Q and (b) likelihood ratio α_Q for particles located in the wall-parallel slice $18 < y^+ < 22$ averaged over time samples between $t^+ = 3960$ and $t^+ = 7920$ for $\mathrm{Re}_\tau = 180$ (solid line, circles), and between $t^+ = 3950$ and $t^+ = 7900$ for $\mathrm{Re}_\tau = 395$ (dashed line, squares).

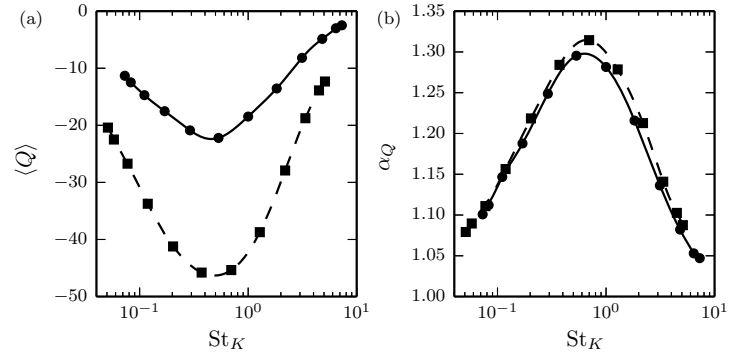

FIGURE 10. (a) Mean particle sampled Q and (b) likelihood ratio α_Q for particles located in the wall-parallel slice $(\mathrm{Re}_\tau - 10) < y^+ < \mathrm{Re}_\tau$ averaged over time samples between $t^+ = 3960$ and $t^+ = 7920$ for $\mathrm{Re}_\tau = 180$ (solid line, circles), and between $t^+ = 3950$ and $t^+ = 7900$ for $\mathrm{Re}_\tau = 395$ (dashed line, squares).

the velocity gradient tensor $\nabla \boldsymbol{u}$, to test this explanation. Q represents the local balance between vorticity and shear strain, and we expect particles to gather in regions of negative Q (where shear is dominating). We use two Q-related measures: the particle sampled mean value $\langle Q \rangle$ and the likelihood ratio α_Q. The ratio α_Q is the fraction of particles located in regions with $Q < 0$ divided by the corresponding fraction for fluid tracers, i.e. α_Q is how many times more likely it is to find a randomly chosen particle in a region of $Q < 0$ than it would be for fluid tracers.

Both $\langle Q \rangle$ and α_Q are plotted for particles in a section of the buffer layer in figure 9, and a section in the core region in figure 10. In the buffer layer we see the particles preferentially sampling regions of the flow with $Q < 0$, as previously observed by Rouson & Eaton (2001). This mechanism is most effective at fairly low Stokes numbers, and both $\langle Q \rangle$ and α_Q take their extreme values at $\mathrm{St} \approx 2$. Since the clustering in the buffer layer is maximised at a significantly higher Stokes number (see figure 7), there must be other effects causing clustering. An increase in the probability and intensity of strong gradients

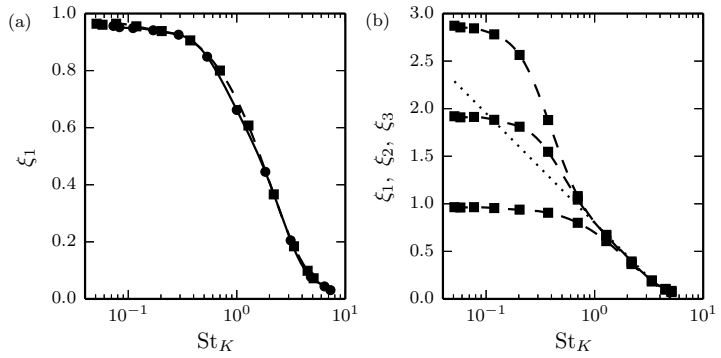

FIGURE 11. Structure function power law exponents ξ_p for r in the dissipative range ($r < \eta_K$), for (a) $p = 1$ and (b) $p = 1, 2, 3$. In (a) both $\mathrm{Re}_\tau = 180$ (solid line, circles) and $\mathrm{Re}_\tau = 395$ (dashed line, squares) are included. The dotted line in (b) is the logarithmic function $0.8 - 0.5 \log \mathrm{St}$.

leads to significantly higher absolute values of $\langle Q \rangle$ at the highest Reynolds number, but measured with α_Q the magnitude of the preferential sampling is roughly equal for the two Reynolds numbers, at all Stokes numbers.

Unlike in the near-wall region, Rouson & Eaton (2001) did not find that the particle distribution was significantly correlated with local flow topology in the centre of the channel. They suggested that this was because the clustering in that part of the channel was created close to the walls and transported to the core region. We find in figure 9 that also in the centre of the channel there is significant preferential sampling of $Q < 0$ regions. Although the absolute values of $\langle Q \rangle$ are much lower than in the buffer layer, because of the much lower values of $\overline{Q^2}$, the likelihood ratio α_Q takes higher values in the centre of the channel. At most, close to 80% of the particles in the centre of the channel, reside in regions with $Q < 0$. The maximum absolute value of $\langle Q \rangle$ is found for $\mathrm{St}_K \approx 0.5$, while α_Q takes its maximum value at $\mathrm{St}_K \approx 0.7$. Also here we find almost completely overlapping α_Q curves, suggesting that the extent to which particles cluster in regions of negative Q, does not depend on Reynolds number. If the majority of the particle clusters in the core region were created close to the wall (as suggested by Rouson & Eaton (2001)) one would expect a stronger Reynolds number dependence.

The vortex centrifuge mechanism is not the only explanation of why particles cluster, and figure 10 can not explain the clustering observed at very large values of St in figure 7. Caustics have been shown to be a significant effect for Stokes numbers greater than unity in homogeneous turbulence (Bec *et al.* 2010), and it would be reasonable to expect similar effects in the channel flow. Because caustics are associated with large close-range velocity differences, we use the longitudinal velocity structure function of order p, $S_p(r)$, defined as

$$S_p(r) = \langle [(\boldsymbol{V}(\boldsymbol{x} + \boldsymbol{r}) - \boldsymbol{V}(\boldsymbol{x})) \cdot \boldsymbol{r}/r]^p \rangle, \tag{3.3}$$

for a separation vector $\boldsymbol{r}$. We use the structure functions to study particle velocities in the slice $(\mathrm{Re}_\tau - 10) < y^+ < (\mathrm{Re}_\tau + 10)$ in the centre of the channel.

For distances r in the dissipation range ($r < \eta_K$), $S_p(r)$ is expected to follow the power law r^p for a smooth velocity field. In plots of $S_p(r)$ (not shown) we observe power laws $S_p(r) \propto r^{\xi_p}$ in the dissipation range. The values of the exponents ξ_p are plotted in figure 11 for $p = 1, 2, 3$. The exponent ξ_1 transitions from a value close to 1 at low Stokes numbers to a value close to 0 at high Stokes numbers, in much the same way as previously observed in homogeneous turbulence (Bec *et al.* 2010). A power law exponent

close to zero means that the velocity difference is almost independent of distance (in the dissipation range), indicating a highly intermittent velocity distribution. That ξ_2 and ξ_3 overlap for a range of Stokes numbers in figure 11, shows that the power law exponents saturate at large orders. Bec *et al.* (2010) proposed that the saturation exponent ξ_∞ could be approximated with a logarithmic function for a certain range of Stokes numbers. The comparison with a logarithmic function in figure 11 indicates that this could also be true in our case, but the modest number of Stokes numbers in the relevant range makes it difficult to conclude.

The ξ_1 curves for $\mathrm{Re}_\tau = 180$ and $\mathrm{Re}_\tau = 395$ are overlapping for the whole range of St_K. This is also true for ξ_2 and ξ_3, which is why only the results for $\mathrm{Re}_\tau = 395$ are included. There does therefore not seem to be any significant Reynolds number effects, however it is impossible to know if this also holds true at much higher Reynolds numbers. Bec *et al.* (2010) did not observe any significant Reynolds number effects in homogeneous turbulence either.

4. Concluding remarks

We have studied the preferential concentration of inertial point-particles in turbulent channel flow, using direct numerical simulation. There is a significant drift of particles towards the walls at both Reynolds numbers $\mathrm{Re}_\tau = 180$ and $\mathrm{Re}_\tau = 395$, and for particles with Stokes numbers between 1 and 100. The maximum particle density is found very close to the wall ($y^+ < 1$) and the value increases approximately linearly with time. The wall-normal flux is maximised for $\mathrm{St} \approx 20$ at both Reynolds numbers, but the mean wall-normal velocity is higher at $\mathrm{Re}_\tau = 395$. A turbulence intensity gradient drift law can not explain the mean wall-normal particle velocity observed. Instead we find that the particle velocity is almost proportional to the wall-normal RMS fluid velocity $\sqrt{\overline{v'^2}}$.

In addition to the wall-normal particle flux, we observe local particle clustering over a wide range of scales and Stokes numbers in both the buffer layer and the core region. Significantly stronger clustering is found at the lowest Reynolds number, which we believe to be the result of the increased wall-normal drift at the highest Reynolds number. The particles have less time to collect in local clusters along their path to the wall.

Preferential sampling of regions of low Q is found in both the buffer layer and in the core region. In the buffer layer, this is a mechanism which is most effective at very low Stokes numbers, significantly lower than the Stokes number at which clustering is maximised. In the centre of the channel, maximum preferential sampling of negative Q is found when the Kolmogorov Stokes number St_K is around unity. The correlation with local fluid structures in the centre of the channel suggests that the particle clusters are formed in the centre of the channel, and not primarily transported from the walls. For St_K around unity, close to 80% of the particles in the centre of the channel reside in regions with $Q < 0$.

By studying dissipation range particle velocity structure functions in the core region, we also find strong intermittency, indicative of caustics, at higher Stokes numbers. The clustering observed in the centre of the channel is the result of the combined effects of preferential sampling of negative Q and clustering caused by caustics.

Although both the wall-normal drift velocity and the clustering are different at the two Reynolds numbers, the two mechanisms that are believed to cause the clustering are not. Neither the preferential sampling of negative Q, nor the particle velocity intermittency, exhibit any significant Reynolds number dependence. This suggests that it is the change in the wall-normal flux that causes the Reynolds number dependence of the clustering, and it emphasises the strong connection between wall-normal particle drift and local clustering, in the turbulent channel flow.

We gratefully acknowledge financial support from COST Action FP1005, for the first author to attend the COST training school "Non-spherical particles and aggregates in fluid flows". Computing time on the Vilje compute cluster at the Norwegian University of Science and Technology (NTNU), was granted by the Research Council of Norway (Programme for Supercomputing) and NTNU.

REFERENCES

Bec, J., Biferale, L., Cencini, M., Lanotte, A. S. & Toschi, F. 2010 Intermittency in the velocity distribution of heavy particles in turbulence. *J. Fluid Mech.* **624**, 527–536.

Caporaloni, M., Tampieri, F., Trombetti, F. & Vittori, O. 1975 Transfer of particles in nonisotropic air turbulence. *J. Atmos. Sci.* **32**.

Duncan, K., Mehlig, B., Östlund, S. & Wilkinson, M. 2005 Clustering by mixing flows. *Phys. Rev. Lett.* **95**, 240602.

Eaton, J. K. & Fessler, J. R. 1994 Preferential concentration of particles by turbulence. *Int. J. Multiphase Flow* **20**, 169–209.

Falkovich, G., Fouxon, A. & Stepanov, M. G. 2002 Acceleration of rain initiation by cloud turbulence. *Nature* **419**, 151–154.

Gustavsson, K., Meneguz, E., Reeks, M. & Mehlig, B. 2012 Inertial-particle dynamics in turbulent flows: caustics, concetration fluctuations and random uncorrelated motion. *New J. Phys.* **14**, 115017.

Karniadakis, G. E., Israeli, M. & Orszag, S. A. 1991 High-order splitting methods for the incompressible Navier-Stokes equations. *J. Comp. Phys.* **97**, 414–443.

Maday, Y., Patera, A. T. & Rønquist, E. M. 1990 An operator-integration-factor splitting method for time-dependent problems: Application to incompressible fluid flow. *J. Sci. Comp.* **5**, 263–292.

Marchioli, C. & Soldati, A. 2002 Mechanisms for particle transfer and segregation in a turbulent boundary layer. *J. Fluid Mech.* **468**, 283–315.

Marchioli, C., Soldati, A., Kuerten, J. G. M, Arcen, B., Tanière, A., Goldensoph, G., Squires, K. D., Cargnelutti, M. F. & Portela, L. M. 2008 Statistics of particle dispersion in direct numerical simulations of wall-bounded turbulence: Results of an international collaborative benchmark test. *Int. J. Multiphase Flow* **34**, 879–893.

Maxey, M. R. 1987 The gravitational settling of aerosol particles in homogeneous turbulence and random flow fields. *J. Fluid Mech.* **174**, 441–465.

Moser, R. D., Kim, J. & Mansour, N. N. 1999 Direct numerical simulation of turbulent channel flow up to $\mathrm{Re}_\tau = 590$. *Phys. Fluids* **11**, 943–945.

Nowbahar, A., Sardina, G., Picano, F. & Brandt, L. 2013 Turbophoresis attenuation in a turbulent channel flow with polymer additives. *J. Fluid Mech.* **732**, 706–719.

Reeks, M. W. 1983 The transport of discrete particles in inhomogeneous turbulence. *J. Aerosol Sci.* **14**, 729–739.

Ripley, B. D. 1976 The second-order analysis of stationary point processes. *J. Appl. Prob.* **13**, 255–266.

Rønquist, E. M. 1988 Optimal spectral element methods for the unsteady three-dimensional incompressible Navier-Stokes equations. PhD thesis, Massachusetts Institute of Technology.

Rouson, D. & Eaton, J. K. 2001 On the preferential concentration of solid particles in turbulent channel flow. *J. Fluid Mech.* **428**, 149–169.

Sardina, G., Schlatter, P., Brandt, L., Picano, F. & Casciola, C. M. 2012 Wall accumulation and spatial localization in particle-laden wall flows. *J. Fluid Mech.* **699**, 50–78.

Squires, K. D. & Eaton, J. K. 1991 Preferential concentration of particles by turbulence. *Phys. Fluids A* **3**, 1169–1178.

Wand, M. P. & Jones, M. C. 1995 *Kernel Smoothing*. London: Chapman & Hall.

Wand, M. P., Marron, J. S. & Ruppert, D. 1991 Transformations in density estimation. *J. Amer. Stat. Ass.* **86**, 343–353.

Wilkinson, M. & Mehlig, B. 2005 Caustics in turbulent aerosols. *Europhys. Lett.* **71**, 186–192.

Xu, C. & Pasquetti, R. 2004 Stabilized spectral element computations of high Reynolds number incompressible flows. *J. Comp. Phys.* **196**, 680–704.

Bibliography

A. Aliseda and J. C. Lasheras. Preferential concentration and rise velocity reduction of bubbles immersed in a homogeneous and isotropic turbulent flow. *Phys. Fluids*, 23(9):093301, 2011.

Jon Louis Bentley. Multidimensional divide-and-conquer. *Comm. ACM*, 23: 214–229, 1980.

C. Canuto, Y. Hussaini, A. Quarteroni, and T. A. Zang. *Spectral Methods in Fluid Dynamics*. Springer Series in Computational Physics. Springer, Berlin, 1998.

G. Coppola, S. J. Sherwin, and J. Peiró. Nonlinear particle tracking for high-order elements. *J. Comp. Phys.*, 172:356–386, 2001.

D. L. Darmofal and R. Haimes. An analysis of 3D particle path integration algorithms. *J. Comp. Phys.*, 123:182–195, 1996.

M. O. Deville, P. F. Fischer, and E. H. Mund. *High-Order Methods for Incompressible Fluid Flow*. Cambridge University Press, Cambridge, 2002.

J. K. Eaton and J. R. Fessler. Preferential concentration of particles by turbulence. *Int. J. Multiphase Flow*, 20:169–209, 1994.

John R. Fessler, Jonathan D. Kulick, and John K. Eaton. Preferential concentration of heavy particles in a turbulent channel flow. *Phys. Fluids*, 6(11):3742–3749, 1994.

P. F. Fischer. Implementation considerations for the OIFS/characteristics approach to convection problems. Unpublished manuscript available, as of 23/04/2014, at `http://www.mcs.anl.gov/~fischer/Nek5000/oifs.pdf`.

J. C. H. Fung, J. C. R. Hunt, N. A. Malik, and R. J. Perkins. Kinematic simulation of homogeneous turbulence by unsteady random Fourier modes. *J. Fluid Mech.*, 236:281–318, 1992.

L. Grindberg and G. E. Karniadakis. Extrapolation-based acceleration of iterative solvers: Application to simulation of 3D flows. *Comm. Comp. Phys.*, 9:607–626, 2011.

M. R. Hestenes and E. Stiefel. Methods of conjugate gradients for solving linear systems. *J. Res. N. B. S*, 49:409–436, 1952.

G. B. Jeffery. The motion of ellipsoidal particles immersed in a viscous fluid. *Proc. R. Soc. Lond. A*, 102:161–179, 1922.

G. E. Karniadakis and S. J. Sherwin. *Spectral/hp Element Mehtods for Computational Fluid Dynamics*. Oxford University Press, Oxford, 2005.

G. E. Karniadakis, M. Israeli, and S. A. Orszag. High-order splitting methods for the incompressible Navier-Stokes equations. *J. Comp. Phys.*, 97:414–443, 1991.

B. W. Kernighan and D. M. Ritchie. *The C Programming Language*, volume 2. Prentice Hall, New Jersey, 1988.

R. M. Kirby and G. E. Karniadakis. Coarse resolution turbulence simulations with spectral vanishing viscosity—large-eddy simulations (SVV-LES). *ASME J. Fluids Eng.*, 124:886–891, 2002.

R. M. Kirby and G. E. Karniadakis. De-aliasing on non-uniform grids: algorithms and applications. *J. Comp. Phys.*, 191:249–264, 2003.

C. L. Lawson, R. J. Hanson, D. R. Kincaid, and F. T. Krogh. Basic linear algebra subprograms for Fortran usage. *ACM Trans. Math. Software*, 5:308–323, 1979.

E. Leriche and G. Labrosse. High-order direct Stokes solvers with or without temporal splitting: Numerical investigations of their comparative properties. *SIAM J. Sci. Comput.*, 22:1386–1410, 2000.

F. Lundell and A. Carlsson. Heavy ellipsoids in creeping shear flow: Transitions of the particle rotation rate and orbit shape. *Phys. Rev. E*, 81:016323, 2010.

Y. Maday, A. T. Patera, and E. M. Rønquist. An operator-integration-factor splitting method for time-dependent problems: Application to incompressible fluid flow. *J. Sci. Comp.*, 5:263–292, 1990.

M. R. Maxey and J. J. Riley. Equation of motion for a small rigid sphere in a nonuniform flow. *Phys. Fluids*, 26:883–889, 1983.

R. Monchaux, M. Bourgoin, and A. Cartellier. Preferential concentration of heavy particles: A Voronoï analysis. *Phys. Fluids*, 22:103304, 2010.

P. H. Mortensen, H. I. Andersson, J. J. J. Gillissen, and B. J. Boersma. Dynamics of prolate ellipsoidal particles in a turbulent channel flow. *Phys. Fluids*, 20:093302, 2008.

R. D. Moser, J. Kim, and N. N. Mansour. Direct numerical simulation of turbulent chanel flow up to Re = 590. *Phys. Fluids*, 11:943–945, 1999.

Y. Notay. Flexible conjugate gradients. *SIAM J. Sci. Comput.*, 22:1444–1460, 2000.

D. R. Osborne, J. C. Vassilicos, K. Sung, and J. D. Haigh. Fundamentals of pair diffusion in kinematic simulations of turbulence. *Phys. Rev. E*, 74:036309, 2006.

M. Picciotto, C. Marchioli, and A. Soldati. Characterization of near-wall accumulation regions for inertial particles in turbulent boundary layers. *Phys. Fluids*, 17:098101, 2005.

B. D. Ripley. The second-order analysis of stationary point processes. *J. Appl. Prob.*, 13:255–266, 1976.

E. M. Rønquist. *Optimal spectral element methods for the unsteady three-dimensional incompressible Navier-Stokes equations.* PhD thesis, Massachusetts Institute of Technology, 1988.

E. M. Rønquist. Convection treatment using spectral elements of different order. *Int. J. Num. Meth. Fluids*, 22:241–264, 1996.

E. M. Rønquist. MA8502 Numerical solution of partial differential equations. Course material, Department of Mathematical Sciences, NTNU, 2012.

E. M. Rønquist and A. T. Patera. Spectral element multigrid. *J. Sci. Comp.*, 2:389–406, 1987.

C. Rosales and C. Meneveau. A minimal multiscale Lagrangian map approach to synthesize non-gaussian turbulent vector fields. *Phys. Fluids*, 18:075104, 2006.

C. Rosales and C. Meneveau. Anomalous scaling and intermittency in three-dimensional synthetic turbulence. *Phys. Rev. E*, 78:016313, 2008.

D. W. I. Rouson and J. K. Eaton. On the preferential concentration of solid particles in turbulent channel flow. *J. Fluid Mech.*, 428(1):149–169, 2001.

S. I. Rubinow and J. B. Keller. The transverse force on a spinning sphere moving in a viscous fluid. *J. Fluid Mech.*, 11:447–459, 1961.

P. G. Saffman. The lift on a small sphere in a slow shear flow. *J. Fluid Mech.*, 22:385–400, 1965.

B. W. Silverman. *Density Estimation for Statistics and Data Analysis.* Chapman & Hall, London, 1986.

H. Tennekes. Eulerian and Lagrangian time microscales in isotropic turbulence. *J. Fluid Mech.*, 67:561–567, 1975.

D. J. Thomson and B. J. Devenish. Particle pair separation in kinematic simulations. *J. Fluid Mech.*, 526:277–302, 2005.

A. G. Tomboulides, M. Israeli, and G. E. Karniadakis. Efficient removal of boundary-divergence errors in time-splitting methods. *J. Sci. Comp.*, 4:291–308, 1989.

M. P. Wand and M. C. Jones. *Kernel Smoothing.* Chapman & Hall, London, 1995.

M. P. Wand, J. S. Marron, and D. Ruppert. Transformations in density estimation. *J. Amer. Stat. Ass.*, 86:343–353, 1991.

D. Wilhelm and L. Kleiser. Stable and unstable formulations of the convection operator in spectral element simulations. *App. Num. Math.*, 33:275–280, 2000.

D. Xiu and G. E. Karniadakis. A semi-Lagrangian high-order method for Navier-Stokes equations. *J. Comp. Phys.*, 172:658–684, 2001.

D. Xiu, S. J. Sherwin, S. Dong, and G. E. Karniadakis. Strong and auxiliary forms of the semi-Lagrangian method for incompressible flows. *J. Sci. Comp.*, 25:323–346, 2005.

C. Xu and R. Pasquetti. Stabilized spectral element computations of high Reynolds number incompressible flows. *J. Comp. Phys.*, 196:680–704, 2004.